



UNIVERSITY OF LEEDS

**Modelling and Observations of
Molecules in Discs Around Young Stars**

John David Ilee

Department of Physics and Astronomy

University of Leeds

Submitted in accordance with
the requirements for the degree of

Doctor of Philosophy

April 2013

The candidate confirms that the work submitted is his own, except where work which has formed part of jointly authored publications has been included. The contribution of the candidate and the other authors of this work has been explicitly indicated. The candidate confirms that appropriate credit has been given within this thesis where reference has been made to the work of others.

This copy has been supplied on the understanding that it is copyright material and that no quotation from the thesis may be published without proper acknowledgement.

© 2013 The University of Leeds and John David Ilee.

For John Wilson.

*Thanks for being there throughout my life,
you are greatly missed.*

Preface

Within this thesis, some chapters have been based on work presented in the following jointly authored publications:

- I. Chemistry in a gravitationally unstable protoplanetary disc, **J. D. Ilee**, A. C. Boley, P. Caselli, T. W. Hartquist and J. M. C. Rawlings, 2011, MNRAS, 417, 2950.
- II. CO bandhead emission of massive young stellar objects: determining disc properties, **J. D. Ilee**, H. E. Wheelwright, R. D. Oudmaijer, W. J. de Wit, L. T. Maud, M. G. Hoare, S. L. Lumsden, T. J. T. Moore, J. S. Urquhart and J. C. Mottram, 2013, MNRAS, 429, 2960.

Paper I forms the basis of Chapter 2. The primary author (J. D. Ilee) was responsible for the complete rewrite of a chemical network provided by J. M. C. Rawlings to be compatible with a physical disc model provided by A. C. Boley. The network was expanded to include thermal desorption and three-body reactions. Various integration methods were tested for the chemical rate equations, and key integration parameters were altered until successful runs were obtained. The chemistry results were combined with the original physical model to provide maps of the column density for each molecule. The chemistry of individual elements, along with the disc as a whole, was interpreted and analysed.

The primary author wrote the initial draft of the publication, and then incorporated comments from co-authors in the final draft.

Paper II forms the basis of Chapter 3. The data were obtained with proposals written by R. D. Oudmaijer and were observed by W. J. de Wit. The primary author (J. D. Ilee) was responsible for the complete data reduction and spectra extraction, along with the data analysis and interpretation. The analysis involved the adaptation of the emission model provided by H. E. Wheelwright, and included changing the physical representations of the circumstellar disc between three possible models which were subsequently tested. The primary author wrote the initial draft of the publication, and then incorporated comments from co-authors in the final draft.

Acknowledgements

I would like to thank René Oudmaijer, Tom Hartquist and Paola Caselli for their supervision and guidance over the past few years, and Hugh Wheelwright, who has been an invaluable source of encouragement. I would also like to thank all the members of the Astrophysics department for making it such an enjoyable place to work.

Thanks must also go to all of my fellow students, who have made working in Leeds not only enjoyable, but also extremely fun. Cheers to Hazel for putting up with me in a small office, to Mo for always being mildly inappropriate, and to Luke for providing an endless supply of anecdotes. Many thanks to Jonny for introducing me to seven year old rum, and being a fantastic mate. I must also say a huge thank you to my girlfriend Stephanie, who kept me sane over the final few months (at least on most days).

I would also like to thank all my family. Ann, John, Marisa & Nick - thank you for your support, your friendship, and for welcoming us every Christmas. Kath, you and John have always been there for me. Finally, but most importantly, I want to thank my mother. Without her love and encouragement, I would not have come close to starting a thesis, never mind finishing one. Thank you.

Abstract

This thesis contains a study of molecules within circumstellar discs around young stars. Firstly, the chemistry of a disc around a young, Class 0 protostar is modelled. Such discs are thought to be massive, and thus experience gravitational instabilities, which produce spiral density waves. These affect the chemistry in three ways; by desorbing molecules from dust grains, by providing extra energy for new reactions to take place, and by mixing the internal structure of the disc to provide a rich chemistry near the midplane.

Secondly, high resolution near-infrared spectra of 20 massive young stellar objects are presented. The objects display CO first overtone bandhead emission, which is excited in the conditions expected within circumstellar discs. The emission is modelled using a simple analytic model of a Keplerian disc, and good fits are found to all spectra. On average, the discs correspond to being geometrically thin, spread across a wide range of inclinations. The discs are located within the dust sublimation radius, providing strong evidence that the CO emission originates in small gaseous discs, supporting the scenario in which massive stars form via disc accretion.

Finally, medium resolution near-infrared spectra of 5 Herbig Ae & Be stars are presented. The spectra cover both CO bandhead and Br γ

emission. Accretion rates are derived from the measuring the Br γ emission and through modelling the CO emission, however these accretion rates are found to be inconsistent. High resolution archival data of one of the targets is presented, and it is shown that this CO disc model is unable to fit the high resolution data. Therefore, it is concluded that to properly fit CO spectra, high resolution data are needed, and that previously published information determined from low resolution spectra should be treated with caution.

Abbreviations

ALMA	Atacama Large Millimeter Array
AMBER	Astronomical Multi-Beam Combiner
AO	Adaptive Optics
arcsec	Second of arc
au	Astronomical Unit
Br	Brackett Series
CCD	Charge-Coupled Device
CO	Carbon Monoxide
CRIRES	Cryogenic High-Resolution IR Echelle Spectrograph
Dec	Declination
E-ELT	European Extremely Large Telescope
ESO	European Southern Observatory
FIR	Far Infrared
FF	Free-Fall
FWHM	Full Width at Half Maximum
GMC	Giant Molecular Cloud
HAeBe	Herbig Ae/Be
IDL	Interactive Data Language
IR	Infrared
IRAF	Image Reduction and Analysis Facility

IRAS	Infrared Astronomical Satellite
ISM	Interstellar Medium
KH	Kelvin-Helmholtz
MAG	Magnitude
MS	Main Sequence
MSX	Mid-course Space Experiment
MYSO	Massive Young Stellar Object
NASA	National Aeronautics and Space Administration
NIR	Near Infrared
pc	Parsec
PMS	Pre-main-sequence
RA	Right Ascension
RMS	Red MSX Source
rms	Root Mean Squared deviance
SED	Spectral Energy Distribution
SNR	Signal to Noise Ratio
TTS	T Tauri star
UV	Ultraviolet
VLT	Very Large Telescope
VLTI	Very Large Telescope Interferometer
YSO	Young Stellar Object
ZAMS	Zero Age Main Sequence
2MASS	Two Micron All Sky Survey

Contents

List of Figures	xvii
List of Tables	xx
1 Introduction	1
1.1 The formation of stars	1
1.1.1 Low mass	5
1.1.2 High mass	8
1.1.3 Intermediate mass	10
1.2 The importance of discs	11
1.3 Astrochemistry	15
1.3.1 Types of reactions	17
1.3.2 The CO molecule	22
1.4 An introduction to this thesis	24
2 Chemistry in a gravitationally unstable disc	27
2.1 Introduction	27
2.2 Methods	30
2.2.1 The physical disc model	30
2.2.2 The chemical model	36

2.2.3	Chemical initial conditions	42
2.2.4	Timescales	43
2.3	Results & Discussion	45
2.3.1	An individual fluid element	45
2.3.2	The disc - face on	47
2.3.3	The disc - other perspectives	51
2.3.4	The effect of three-body reactions	52
2.3.5	Comparison with other models	54
2.4	Conclusions & Future Work	58
3	CO bandhead emission of MYSOs	61
3.1	Introduction	61
3.2	Models	63
3.2.1	The CO emission model	63
3.2.2	A disc of CO	65
3.2.3	The physical disc structure	67
3.3	Observations and sample selection	72
3.3.1	Observational results	73
3.4	Fitting the data	75
3.4.1	The fitting procedure	75
3.4.2	A test of the disc models - W33A	77
3.5	Full sample results	83
3.6	Discussion	90
3.6.1	Disc sizes - the location of the emission	90
3.6.2	Determining mass accretion rates	92

3.6.3	Are these typical MYSOs?	93
3.7	An object by object comparison with previous studies	96
3.8	Lower mass YSOs and objects that were not fitted	102
3.9	Conclusions	103
4	Accretion rates in HAeBes	107
4.1	Introduction	107
4.2	Observations & sample selection	109
4.2.1	Telluric line removal	111
4.3	Results from Br γ	115
4.3.1	Accretion rates	116
4.4	Results from CO	120
4.4.1	A case study: V596 Car	120
4.4.2	Multiple bandheads	122
4.4.3	Full sample results	125
4.5	Analysis & Discussion	132
4.6	Exploring the effect of higher resolution data	134
4.7	Conclusions	138
5	Conclusions	141
5.1	Summary	141
5.2	Future work	146
5.3	Final remarks	151
	Bibliography	152

List of Figures

1.1	Multiwavelength view of the Rosette nebula.	2
1.2	Schematic of low mass star formation.	6
1.3	Simulation of a gravitationally unstable disc.	13
1.4	A selection of the main ion-molecule reactions initiated by H_3^+	21
1.5	A schematic of the $v = 2 - 0$ CO bandhead	23
2.1	Column density of nuclei in disc.	32
2.2	The final location of the fluid elements within the disc.	34
2.3	Temperature structure of the disc.	35
2.4	Slices of the disc interior showing the number densities and temperatures.	37
2.5	Temperature and number density history of a fluid element in the disc.	38
2.6	Fractional abundance of species for a fluid element in the disc.	46
2.7	Column densities of molecules within the disc (dominated by adsorption and desorption).	49
2.8	Column densities of molecules within the disc (where total abundance varies with time).	51

2.9	Column densities of the disc from the side.	53
2.10	Slices of the disc interior showing the fractional abundances.	53
2.11	Comparison of slices of the disc interior with an axisymmetric disc.	57
3.1	Spectra produced by slabs of CO in different conditions	66
3.2	Spectra produced by discs of CO in different conditions	68
3.3	CO bandhead of IRAS 08576–4334 with model fit	75
3.4	Best fitting CO bandhead spectra to W33A using three different physical disc models	78
3.5	Exploration of the chi squared parameter space for fits to W33A	79
3.6	Exploration of the chi squared parameter space for fits to W33A, using a bloated star	81
3.7	Model fits to the CO bandhead emission of the MYSOs	84
3.8	Distribution of inclinations, temperature exponents and density ex- ponents of the best fitting discs for the MYSOs	89
3.9	Comparison of the inner and outer disc radii with the dust subli- mation radius of each object.	91
3.10	Cumulative frequency of NIR and MIR colours of the MYSOs with CO emission compared to the RMS population as a whole.	95
3.11	Model fits to objects later confirmed to be lower mass YSOs.	102
3.12	Objects with CO emission that was too weak for a fit to be obtained.	103
4.1	Examples of methods to remove telluric spectral features	114
4.2	Br γ emission lines for the sample of HAeBes	119
4.3	Fits obtained for V596 Car using two separate disc models	121
4.4	Spectra produced using disc model B with different free parameters	123

4.5	Fits to V596 Car using one, two and three CO bandheads	124
4.6	Model fits to the CO bandhead emission of the HAeBes	129
4.7	Comparison of best fitting CO parameters for each HAeBe	131
4.8	Line luminosities and mass accretion rates determined from the CO and Br γ	134
4.9	Comparison of CRIRES and X-SHOOTER data for V1052 Cen	135
4.10	Model fits to the CRIRES data of V1052 Cen	136
5.1	Synthetic ALMA observations of the gravitationally unstable disc	148

List of Tables

1.1	Angular momentum in the stages of stellar evolution	12
1.2	Common reactions in astrophysical environments	18
2.1	Initial fractional abundances used for the chemical network.	43
2.2	Comparison of maximum abundances with other models.	55
3.1	Observational information for each MYSO	74
3.2	Allowed ranges of parameters for the model fitting procedure	76
3.3	Best fitting disc model parameters for W33A	78
3.4	Stellar parameters used for the model fitting	85
3.5	Best fitting disc parameters for all MYSO spectra.	86
4.1	Log of the observations of HAeBe sample	110
4.2	Astrophysical parameters of the HAeBe sample	110
4.3	Measured parameters from the Br γ emission lines	116
4.4	Accretion luminosity and mass accretion rate for the sample of HAeBes	117
4.5	Measured parameters from the CO emission	122
4.6	Best fitting parameters to V596 Car using one, two and three CO bandheads	125

4.7 Parameters obtained from the CO fitting of the HAeBes 126

4.8 Best fitting model parameters for high resolution V1052 Cen data . 137

Chapter 1

Introduction

1.1 The formation of stars

Star formation in our Galaxy occurs mostly within giant molecular clouds (GMCs) located primarily in the spiral arms of the Galactic plane (Shu *et al.*, 1987a). GMCs are thought to exist for around 10^7 years, and during that time the influences of their surrounding environment creates much of the complex structure observed within them. For example, shocks driven by stellar winds, supernova remnants or ionised hydrogen (H II) regions can compress and shape the GMCs, forming structures such as filaments and voids within them. The Rosette Molecular Cloud (RMC) provides a good example of a GMC; it has a mass of about $1\text{--}2 \times 10^5 M_{\odot}$, covers an area on the sky of approximately 2200 pc^2 and has a mean molecular hydrogen number density, $n(\text{H}_2)$, of 30 cm^{-3} (Williams *et al.*, 1995). Figure 1.1 shows an intensity map of carbon monoxide (CO) in the RMC, tracing the distribution of matter and showing the inhomogeneous nature of the region.

The majority of the mass of a GMC lies in denser regions known as clumps. The

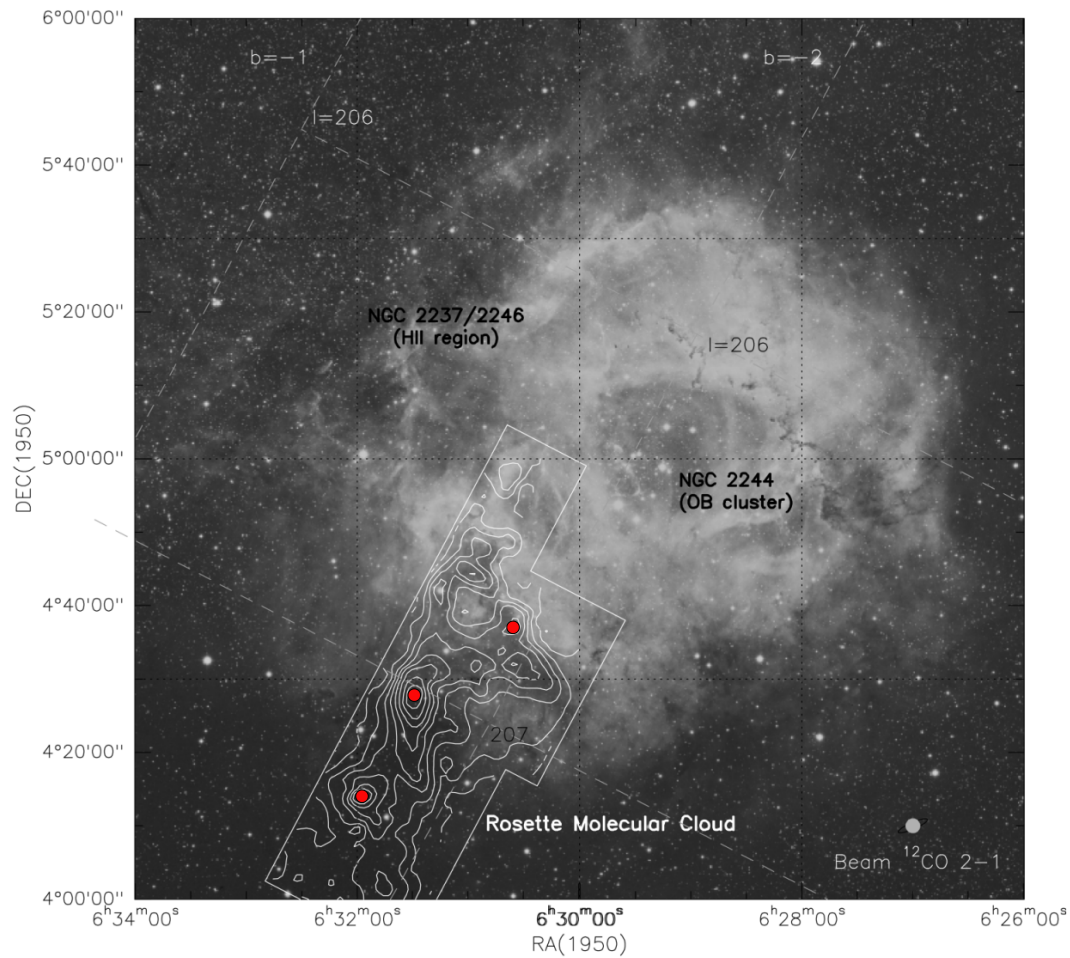


Figure 1.1: Optical image of the Rosette nebula from the Palomar Observatory Sky Survey, overlaid with contours of ^{12}CO J=2-1 emission, which indicates the position of the Rosette Molecular Cloud. Red circles indicate the position of bright infrared sources that have been detected in the region. Taken from Schneider *et al.* (1998)

RMC has approximately 70 clumps, with observed densities of $n(\text{H}_2) \sim 220 \text{ cm}^{-3}$, temperatures of around 10 K, sizes of up to 5 pc and masses of between 30–2500 M_\odot (Williams *et al.*, 1995). Their susceptibility to collapse under their own self gravity can be approximately assessed by examining the Jeans mass (Jeans, 1902), which can be expressed as

$$M_J = \left(\frac{\pi k_b T}{\mu G} \right)^{3/2} \rho^{-1/2}, \quad (1.1)$$

where T and ρ are the local temperature and density of the clump, k is the Boltzmann constant, G is the gravitational constant and μ is the molecular weight of the material in the clump. Regions with a mass greater than M_J will be susceptible to gravitational collapse. For the clumps in the RMC, this critical mass is approximately 50 M_\odot . Observations have suggested that clumps in the RMC have masses of the order $10^3 M_\odot$, which is far higher than the Jeans mass. This suggests that these regions should have already undergone collapse, and therefore should not exist. This presents a problem with this theoretical prescription of how gravitational collapse proceeds.

However, molecular clouds and clumps have been observed to possess magnetic fields (Kazes & Crutcher, 1986), which has not been considered in the above treatment. Magnetic field gradients cause forces on charged particles. This introduces a relative motion between the charged and neutral particles, which is known more commonly as ambipolar diffusion (Mestel & Spitzer, 1956). This causes collisions between them, which results in a drag force between the charged and neutral particles. This drag force impedes the gravitationally induced collapse of the neutral material in the cloud. Observations of clumps reveal linewidths that are greater than those expected by purely thermal motions. These super-thermal motions are

thought to be due to the presence of magnetohydrodynamic (MHD) waves (Arons & Max, 1975; Falgarone & Phillips, 1990). These waves cause an increase in the effective pressure of the clump material, which offers another source of support against gravitational collapse. When ambipolar diffusion and MHD waves are taken into account, the effective Jeans mass is raised sufficiently to allow clumps to resist collapse (Shu *et al.*, 1987a).

Within clumps, smaller dense core regions are detected with typical densities of $n(\text{H}_2) = 10^5 \text{ cm}^{-3}$ (Myers *et al.*, 1987). At the density of the cores, the fractional ionisation is low enough that magnetic fields can no longer offer sufficient support to the material against gravity, and the collapse to stellar densities can occur. Bright infrared sources are also detected within the cores (as indicated in Figure 1.1). The temperature of the core is not sufficient to create such emission, and thus there must be a central object in the cores that is powering this radiation. These are thought to be young stars in the earliest stages of formation - protostars.

The timescales over which cloud collapse occurs can offer insight into the nature of the stars that are formed in these regions. The timescale for gravitational collapse is given by the free-fall time (Shu *et al.*, 1987b),

$$t_{\text{ff}} = \left(\frac{3\pi}{32G\rho} \right)^{1/2} \approx 3.4 \times 10^7 n^{-1/2} \text{ yr}, \quad (1.2)$$

where ρ is the average mass density of the material, and n is the number density per cubic centimetre. Using the RMC as an example, with a mean number density of 30 cm^{-3} , the longest free fall time would be approximately $6 \times 10^6 \text{ yr}$, giving an upper limit on the timescale for stellar evolution.

However, gravitational free-fall does not occur indefinitely. As mentioned pre-

viously, collapsing material comes together in the centre of the collapse region, where a protostar is formed. The gravitational potential energy of the material is converted into heat. The timescale on which this process occurs is given by the Kelvin-Helmholtz time,

$$t_{\text{KH}} \approx \frac{GM_{\star}^2}{R_{\star}L_{\star}}, \quad (1.3)$$

where M_{\star} , R_{\star} and L_{\star} are the protostellar mass, radius and luminosity, respectively. This provides an estimate of the time taken for objects to evolve to the point immediately prior to the onset of nuclear fusion within their core. For a solar mass star, this time is relatively long at $t_{\text{KH}} \approx 3 \times 10^7$ yrs, but for a star of $50 M_{\odot}$ and $10^4 L_{\odot}$, collapse takes place rapidly, and $t_{\text{KH}} \approx 10^4$ yrs. For stars with masses greater than $8 M_{\odot}$, then $t_{\text{KH}} > t_{\text{ff}}$, which implies that fusion begins before the final collapse to stellar densities. This allows a natural division to be made between two types of stars - low mass ($M < 8 M_{\odot}$) and high mass ($M > 8 M_{\odot}$).

1.1.1 Low mass

The term usually given to the system of a forming protostar and surrounding envelope is a young stellar object (YSO). These YSOs are often grouped into four main classes, which are thought to represent an evolutionary sequence. Three classes were originally defined, Class I–III, by Lada (1987), and were later updated by Andre *et al.* (1993) to include a Class 0 phase. These classes are defined by observations of spectral energy distributions (SEDs). Quantitatively, this can be described by the slope of the SED (or spectral index, a) between 10–100 μm , where

$$a = \frac{d \log(\lambda F_{\lambda})}{d \log \lambda}. \quad (1.4)$$

Figure 1.2 shows a schematic diagram of the evolutionary sequence along with an expected SED for an object of each class.

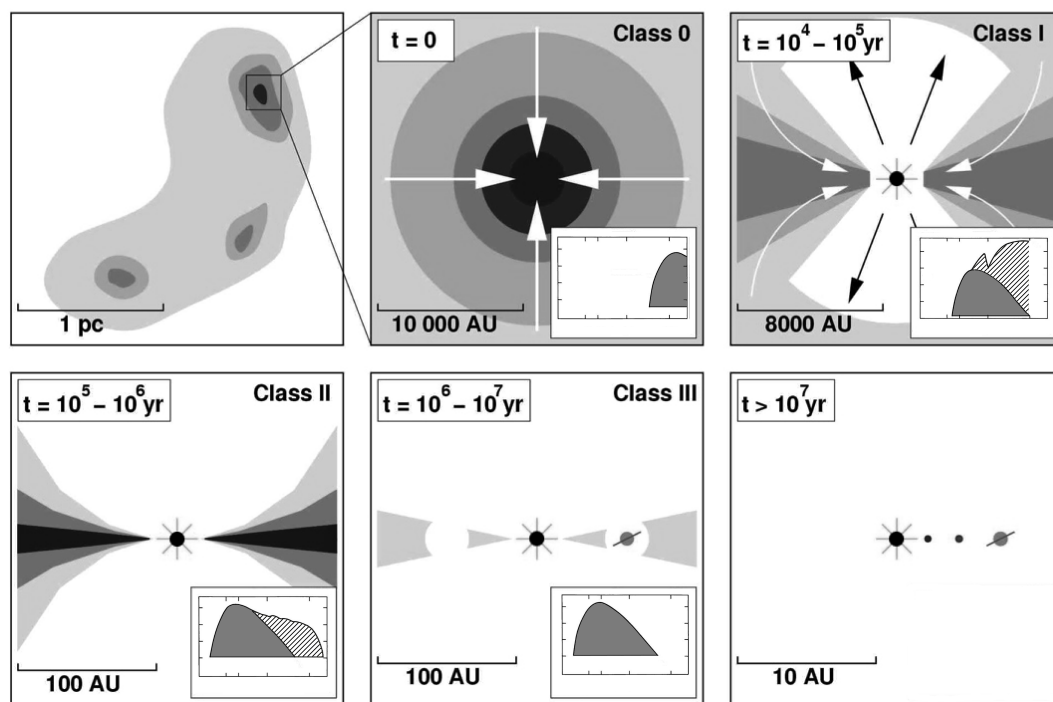


Figure 1.2: Schematic view of low mass star formation, as based on Shu *et al.* (1987a) and Andre *et al.* (1993). Labels show typical timescales and sizes, and insets show the theoretical SED for each evolutionary class. Adapted from Jonkheid (2006).

An early Class 0 object is only observed at longer wavelengths, due to the optically thick, dusty envelope that firstly absorbs and then re-radiates energy from the central protostar. The SED follows a blackbody shape, with a peak corresponding to a temperature of approximately 30 K, in the submillimeter wavelength range where $\lambda > 100 \mu\text{m}$. For Class 0 sources, $a > 3$. They have been observed to possess powerful bipolar outflows, where material is launched away

from the protostar, thus accretion cannot be purely spherical.

After 10^4 – 10^5 years, the Class I phase is reached, where the temperature of the envelope rises to approximately 100 K, and the peak of the SED moves into the far-infrared regime, with $\lambda \approx 30 \mu\text{m}$. For Class I sources, $0 < a \leq 3$. The effects of rotation become important, and the infalling material forms an accretion disc around the protostar, which can be seen as an additional component in the SED, at shorter mid-infrared wavelengths, corresponding to temperatures of around 300 K. Jets and outflows have been observed in these objects, showing cavities being cleared perpendicular to the plane of the accretion disc.

The Class II phase occurs after 10^5 – 10^6 years, at which point a large fraction of the surrounding envelope of cloud material has been dispersed by winds and outflows from the central protostar. The SED now contains an infrared tail, with a component from the central star possibly visible in the optical, and ultraviolet radiation emanating from accretion on to the stellar surface, progressing through magnetically channelled accretion funnels. For Class II sources, $-2 \leq a \leq 0$. This is usually known as a T Tauri star, so-called because of the archetype of its class, T Tauri.

After 10^6 – 10^7 years, the Class III phase begins. These objects possess a typical stellar blackbody SED, with a faint longer wavelength tail due to remnant circumstellar material. Some objects show dips in their SED profiles. This has been suggested as evidence for giant planet formation, where material at a constant radius from the central star has collapsed to form a planetary body, and thus there is a lack of material emitting at the temperature of the disc at this radius, causing a dip in the SED. Smaller, rocky planets may condense and form from the

debris disc of material. For Class III sources, $-3 \leq a \leq -2$. After this phase is complete, the stellar system has completed formation and is known as a zero-age main sequence object (ZAMS).

1.1.2 High mass

Massive stars are much rarer than lower mass stars, but they are important from stellar to galactic scales. The high temperature and luminosity of a massive star results in the injection of large amounts of ionising radiation and kinetic energy into its surroundings, which shapes the local interstellar medium (ISM) and may trigger nearby star formation. They also deposit chemically enriched material into the ISM via continuous mass loss during their lifetime and in supernova explosions at the end of their lives.

Despite their importance to the ISM, the formation mechanisms of massive stars are poorly understood (see the review of Zinnecker & Yorke, 2007). They form extremely quickly ($t_{\text{KH}} = 10^{4-5}$ yrs) and are therefore rare and located at large distances compared to more common lower mass YSOs. Because of their rapid formation timescale, the massive young stellar objects (MYSOs) reach the main sequence and obtain a high luminosity while still enshrouded in their natal cloud material. These characteristics of massive stars present a challenge to theories of their formation, particularly when considering a scaled up version of low mass star formation (as in Shu *et al.* 1987b, see Norberg & Maeder 2000). For instance, because of the short Kelvin-Helmholtz time, there is only a short time to accumulate sufficient mass before the protostar ionises the surrounding material. This ionisation, along with significant radiation pressure from the central proto-

star due to high luminosities, acts on the collapsing material and may halt further accretion (Kahn, 1974; Larson & Starrfield, 1971; Wolfire & Cassinelli, 1987).

However, recent 3D hydrodynamic models indicate that discs circumvent the proposed barrier to massive star formation by facilitating the accretion of matter on to the central object (Krumholz *et al.*, 2009; Kuiper *et al.*, 2010, 2011). In addition, observations have shown that some ultra-compact H II regions have outflows, usually associated with ongoing accretion (e.g. Klaassen *et al.*, 2011). Thus, continued accretion must be possible after the star reaches the main sequence and begins ionising its surroundings.

Obtaining observational evidence of discs in MYSOs is difficult for two reasons. Firstly, the objects are heavily extinguished, making direct imaging impossible in the optical, and difficult with other wavelengths. Secondly, because the formation phase of massive stars is short, MYSOs are rare, and thus a representative sample has been difficult to obtain. Early searches for MYSOs were conducted using the *IRAS* point source catalogue (Molinari *et al.*, 1996; Sridharan *et al.*, 2002). This suffered from source confusion due to the large beam size (2–5 arcmin at 100 μm) and was biased to isolated objects away from the Galactic plane, to avoid confusion with background infrared emission. This issue has been addressed by the Red *MSX* Source (RMS) survey (Lumsden *et al.*, 2002), which is an unbiased survey of MYSOs throughout the Galaxy. It is drawn from the *MSX* mid-infrared survey of the Galactic plane (Egan *et al.*, 2003), which has a resolution of 18 arcsec, allowing detection of sources in previously unresolved regions. An extensive multi-wavelength campaign has been conducted to identify contaminant objects within the *MSX* survey, such as ultra-compact H II regions and planetary nebulae (Mot-

tram *et al.*, 2007, 2010; Urquhart *et al.*, 2007, 2009), finally yielding approximately 500 candidate MYSOs in the database.

1.1.3 Intermediate mass

In practice, there is not a sudden division between the low and high mass stars, but rather a gradual change across the mass range. Stars that occupy the intermediate mass regime (between 2 and 10 M_{\odot}) are thought to form from the pre-main sequence Herbig Ae/Be (HAeBe) stars, which were first discussed by Herbig (1960). Originally, these stars were identified based on three criteria: i) The star has a spectral type A or B with emission lines, ii) it is located in an obscured region, and iii) the star illuminates a bright nearby nebulosity. These criteria proved useful for the identification of HAeBes, and several large catalogues have been compiled (e.g. Thé *et al.*, 1994; Vieira *et al.*, 2003).

HAeBe stars are optically bright, and therefore offer a unique opportunity to study the formation of stars between the lower mass T Tauri stars and the higher mass MYSOs. It is across this mass range that the accretion is thought to switch from the mechanism in lower mass stars, magnetically controlled accretion from discs that are separated from the surface of the central protostar; to discs that reach directly on to the stellar surface (Mottram *et al.*, 2007; Oudmaijer *et al.*, 2011). Therefore, study of this class of objects will offer insight into the accretion processes in both low and high mass stars.

1.2 The importance of discs

Disc-like structures are ubiquitous across all scales of objects in the Universe; from the largest spiral galaxies, to planetary rings such as those around Saturn. In the context of star formation, circumstellar discs form because the collapsing cloud of material possesses some angular momentum, \vec{J} , given by,

$$\vec{J} = \int \rho(\vec{r}) (\vec{r} \times \vec{v}(\vec{r})) d^3\vec{r} \approx \vec{\omega}mr^2, \quad (1.5)$$

where ρ , \vec{v} and \vec{r} are the mass density, velocity and position vector relative to the centre of the cloud. Since angular momentum is conserved as matter moves toward the protostar (a decrease in r) the velocity will increase, leading to an increase in angular velocity $\vec{\omega}$. This causes a centrifugal force that opposes direct collapse which is strongest perpendicular to the rotation axis, and weaker parallel to the rotation axis. The overall effect of this is the emergence of a flattened structure - a circumstellar accretion disc.

The presence of discs in a star formation context is important for several reasons. Apart from being the sites of planet formation, discs provide a route for removing angular momentum from material that will accrete, which is required if the full collapse is to proceed. Table 1.1 shows measured values of the specific angular momentum for different evolutionary stages of star formation.

It is clear that the angular momentum needs to be reduced by orders of magnitude before collapsing material can produce a main sequence star. The emergence of a disc provides an important stage in which the loss of this angular momentum can occur. However, the specific mechanisms that transfer angular momentum through a disc are not known, but an effective coupling between concentric annuli

Table 1.1: Characteristic values of specific angular momentum for various stages of stellar evolution. Taken from Bodenheimer (1995).

Object	Specific Angular Momentum J/m [cm ² s ⁻¹]
Molecular Clump	10 ²³
Molecular Core	10 ²¹
T-Tauri Star	5 × 10 ¹⁷
Main Sequence Star	10 ¹⁵

is required. This effect can be understood if one imagines two masses at different radii in the disc, connected by a stretched spring. The inner mass rotates faster than the outer mass, and the spring torque acts to slow the inner material, lowering its angular momentum and causing it to move to a smaller radius. The outer mass has a corresponding increase in angular momentum and moves to a larger radius, which acts to increase tension in the spring. This cycle continues at all points within the disc and the net effect is to transport angular momentum outwards (Balbus, 2003a). Though molecular viscosity is insufficient, some form of viscosity provides this spring-like connection, but it may be due to a combination of several mechanisms rather than a single phenomenon.

In massive discs, the gravitational effect of the disc material itself can become important, and therefore provide the effective connection between annuli within the disc. In these ‘self gravitating’ discs, the effect of this connection is the emergence of gravitational instabilities (GIs) which produce rotating spiral arms in the disc material. Figure 1.3 shows a simulated disc with these spiral waves developing. The vulnerability of a disc to gravitational instabilities is set by the balance between the self-gravity of the disc material (which drives collapse), the pressure

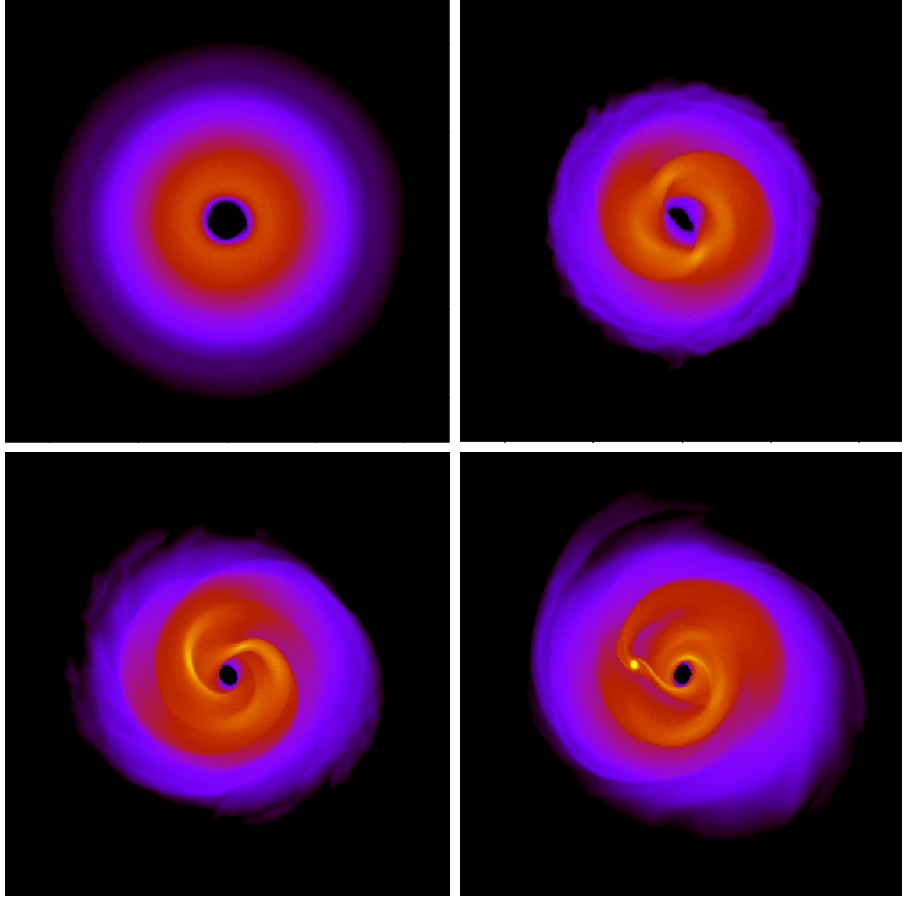


Figure 1.3: Simulation of a gravitationally unstable disc around a $0.3 M_{\odot}$ protostar at four time steps from a simulation of Boley (2009). The colour scale indicates surface density. Spiral waves appear in the initially smooth disc, which eventually lead to a bound protoplanetary fragment in the final panel.

(which prevents small-scale collapse) and the rotation (which prevents large-scale collapse). This can be quantified by the Toomre Q parameter (Toomre, 1964),

$$Q = \frac{c_s \kappa}{\pi G \Sigma} < 1 \quad (1.6)$$

where κ is the epicyclic frequency (representing the rotational support, and equal to the angular velocity Ω in a Keplerian disc), c_s is the sound speed of the gas

(representing the pressure support) and Σ is the surface density of the gas. A thin disc becomes gravitationally unstable when the material becomes dense enough to overcome the support against gravity, i.e. when $Q < 1$. When this condition is fulfilled, for instance in a sufficiently massive or cold disc, the region is susceptible to gravitational instability.

Another mechanism that produces an effective viscosity is the magneto-rotational instability (MRI), a magnetohydrodynamic effect that occurs when a Keplerian disc is threaded by a magnetic field. The fundamentals of this instability were first described in a general sense by Velikhov (1959) and Chandrasekhar (1960) but its application to accretion discs was not investigated until Balbus & Hawley (1991). If dissipative effects can be ignored, for instance if the disc has no resistivity, the magnetic field lines can be considered to be ‘frozen’ into the disc material, so that as material threaded by a magnetic field line moves, the field line stays attached to the material and is carried along by the flow. This gives rise to the spring-like connection discussed earlier. As material moves apart, the tension in the field lines increases and results in a runaway process (Lodato, 2008). This process will only occur in discs (or regions within them) in which the ionisation fraction is sufficient.

The proper theoretical treatment of the potential sources of disc viscosity is complex, and until recently was too computationally expensive. To avoid these complex assumptions on the exact nature of the viscosity, methods were developed to assign an ‘anomalous’ viscosity to discs, in which the viscosity, ν , is characterised by

$$\nu = \alpha H_p c_s, \tag{1.7}$$

where H_p is the pressure scale height of the disc, c_s is the sound speed of the disc material, and α is a dimensionless variable that scales the effective viscosity of the disc, where a larger α corresponds to a more viscous disc environment. Using this approximation allows the viscosity problem to be quantified by way of the α parameter (in circumstellar discs, often $\alpha \sim 0.01$ – 0.001) without having to investigate the source of the viscosity in detail. These α -disc models have been useful in providing a zeroth-order approximation to viscosity, but they cannot fully describe complex discs in which the viscosity is not constant. Modelling this viscosity and angular momentum transport has been the subject of much current research, reviews of which can be found in Balbus (2003b); Bodenheimer (1995); Dullemond *et al.* (2007); Lodato (2008) and Armitage (2011).

1.3 Astrochemistry

One of the most useful tools in astronomy is spectroscopy - the analysis of the electromagnetic spectrum of an object. Often, this involves measurements of the emission and absorption lines in the spectrum. This can reveal information on the physical and dynamical structure of an astrophysical object. The detection of certain molecular lines confirms different physical conditions such as temperatures and densities, the widths of individual spectral lines can give rotational velocities and thermal or non-thermal motions, and Doppler shifted lines give information about line of sight velocities. This information can be obtained even for unresolved objects. However, much of this information depends on a good understanding of how the chemistry occurring within the objects operates and evolves - the study of astrochemistry.

At the time of writing, more than 170 molecules have been detected in interstellar space (Müller *et al.*, 2005). To properly model the behaviour of even a small subset of these molecules, complex networks of chemical reactions are needed. These reaction networks (which utilise data on the rates of chemical reactions obtained both experimentally and theoretically) are used to follow the chemical composition in various models of astrophysical environments. Several groups have compiled large, publicly available databases of both chemical reaction networks, and reaction rates. Two major examples are the UMIST Database for Astrochemistry, (UDfA; Millar *et al.* 1997a, Woodall *et al.* 2007, McElroy *et al.* 2013), and the Kinetic Database for Astrochemistry (KIDA; Wakelam *et al.* 2012).

To discuss these networks further, it is useful to consider a simple example. The rates of formation and destruction of a species depend on the temperature and density of the medium and the abundance of the reactants. If molecule X is created by



and destroyed by



where k is the rate co-efficient of the reaction in $\text{cm}^3 \text{s}^{-1}$, then the rate of change of number density of species X will follow

$$\frac{d}{dt}n(X) = \sum_A \sum_B k_{AB}n(A)n(B) - \sum_C k_{XC}n(C)n(X) \quad (1.10)$$

which is known as the rate equation for species X. The rate coefficient k is determined by $k = \langle \sigma v \rangle$, where σ is the effective cross section of the particles, v is

their velocity and the averaging is performed over all particles in the reaction. If the reaction possesses an activation energy, E_a , the rate co-efficient is often well represented by the Arrhenius formula,

$$k = A(T) \exp\left(\frac{-E_a}{k_b T}\right) \quad (1.11)$$

where T is the temperature of the medium, and the factor $A(T)$ is a function of temperature. In the most simple cases, it is these rate coefficients that are recorded in chemical reaction networks such as the UDfA and KIDA.

1.3.1 Types of reactions

Chemical reactions important in the interstellar medium can fall into several categories, and can involve a variety of reactants. At interstellar densities and temperatures, the overwhelming majority of these involve just two species, and are therefore known as two-body reactions. There are several types of two-body reactions. Table 1.2 lists the common types of reactions and a typical rate coefficient for each.

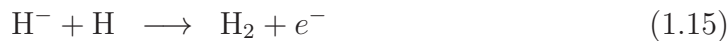
In GMCs, molecular hydrogen (H_2) is the most abundant species, and influences much of the initial chemistry. It is therefore important to consider how it forms. If a simple early universe is assumed to contain neutral atomic hydrogen, some hydrogen ions and electrons that have not recombined, and neutral atomic helium, then the following ion-neutral reaction sequence will take place



Table 1.2: Common reactions in astrophysical environments. The photoabsorption rates are typical for the unshielded standard interstellar radiation field and are negligible in dense molecular regions. Adapted from van Dishoeck & Hogerheijde (1999) and Caselli (2005)

Reaction	Process	Rate Coefficient k [$\text{cm}^3 \text{s}^{-1}$]
Neutral-neutral	$A + B \longrightarrow C + D$	$10^{-12} - 10^{-10}$
Radiative association	$A + B \longrightarrow AB + h\nu$	$10^{-16} - 10^{-13}$
Ion-neutral	$A^+ + B \longrightarrow C^+ + D$	10^{-9}
Dissociative recombination	$AB^+ + e^- \longrightarrow A + B$	10^{-6}
Charge transfer	$A^+ + B \longrightarrow A + B^+$	10^{-9}
Photodissociation	$AB + h\nu \longrightarrow A + B$	$10^{-11} [\text{s}^{-1}]$
Photoionisation	$A + h\nu \longrightarrow A^+ + e^-$	$10^{-11} [\text{s}^{-1}]$

This sequence, and the reaction of hydrogen anions with atomic hydrogen,



dominate production of the initial H_2 (Lepp & Stancil, 1998). Following recombination and prior to the formation of stars, photodissociation of H_2 is negligible. However, once stars form, the incident radiation field also acts to photodissociate H_2 via



at a rate (given in Table 1.2) which is too fast for the above production routes to form the amounts of H_2 present in the Galaxy. One can therefore assume that since a great deal of H_2 is detected, there must be another mechanism creating it that we have yet to consider. The above treatment has only concerned gas phase reactions. In fact, there is another component that is important in the study of

the chemistry of interstellar clouds - dust grains.

Dust grains are formed in the extended atmospheres of cool stars, and ejected into the interstellar medium where they undergo physical and chemical processing (Humphreys & Lockwood, 1972; Williams, 2005). Their surfaces provide a location for further chemistry to occur, and this grain-surface chemistry is of particular importance as it provides a means by which further reactions can create different species. Gas phase molecules attach themselves to the surfaces of dust grains (a process known as adsorption) via two mechanisms: physisorption (involving weak van der Waals forces) or chemisorption (due to chemical valence bonds). At the low temperatures encountered in GMCs, physisorption is thought to dominate because chemisorption has a potential barrier to overcome. Once species are adsorbed, they produce layers of ices on the surface of dust grains, which allows more complex surface chemistry to occur (Herbst & van Dishoeck, 2009). An example of this is the process of hydrogenation, by which surface hydrogen reacts quickly with other surface species (including itself) to produce saturated molecules. For instance, H_2 can be formed via



where the superscript (s) denotes a species on the surface of a dust grain. This $\text{H}_2^{(\text{s})}$ is then removed from the grain surface back into the gas phase, a process known as desorption. This mostly occurs by utilising the excess energy created during its formation, but thermal (sublimation) or non-thermal (cosmic ray) desorption may also occur. This mechanism dominates the formation of H_2 in the interstellar

medium.

In the cold, dense cores mentioned earlier, reactions with large activation energies do not occur, as there is not sufficient thermal energy to overcome the barriers. These regions are also self-shielded from incident stellar radiation, so few reactions that are initiated by photons occur. It is therefore ion-molecule reaction sequences (initiated by cosmic ray induced ionisations) that dominate much of the gas phase chemistry. For example, the following reaction



where γ indicates a cosmic ray, occurs in 97% of cases (3% of the ionisations produce H^+) and proceeds at a rate of 10^{-17} s^{-1} (Hartquist & Dalgarno, 1996). The newly formed H_2^+ reacts swiftly with further H_2 in the reaction



to produce H_3^+ . This H_3^+ is important for many further reactions which include species such as atomic carbon and atomic oxygen, leading to the formation of many new species as indicated in Figure 1.4.

The conditions for chemistry in protoplanetary discs can be quite different to that of interstellar or core chemistry. The number densities and temperatures are much higher, with $n(\text{H}_2) \approx 10^9\text{--}10^{14} \text{ cm}^{-3}$ and $T \approx 30\text{--}1000 \text{ K}$ depending on the location within the disc, as opposed to $10^4\text{--}10^5 \text{ cm}^{-3}$ and about 10 K in GMCs. This means that different chemical processes will occur, and therefore these processes need to be considered. The increased densities also mean that

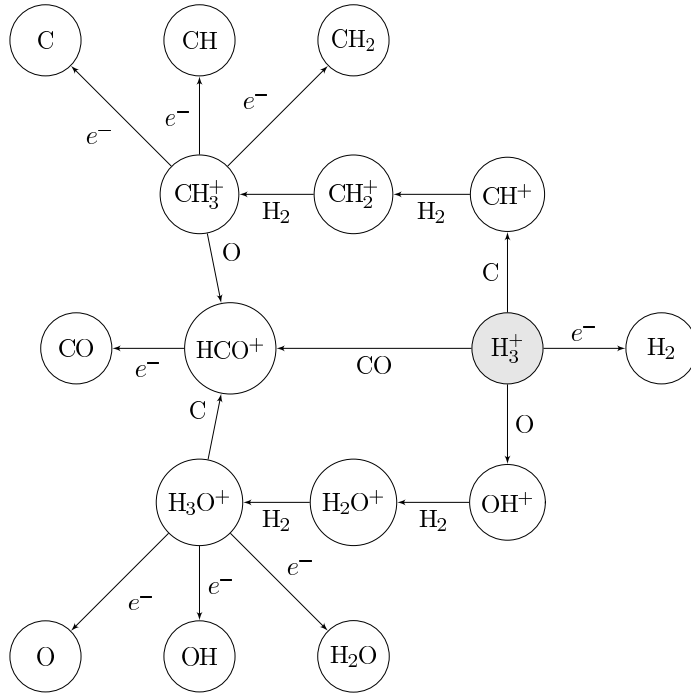


Figure 1.4: A selection of the main ion-molecule reactions in dark clouds, initiated by H_3^+ .

three-body reactions in the gas phase will begin to have an important effect on the chemistry. In these cases, a third body (M, the most abundant species) acts as a non-reacting catalyst in situations such as



This has been included in models by Willacy *et al.* (1998) and others. Thus, it is clear that detailed consideration of the reactions occurring in these regions is required, along with the physical conditions expected, in order to properly model the chemistry.

1.3.2 The CO molecule

As can be seen from Figure 1.1, CO is a common interstellar molecule. It possesses a strong binding energy and is therefore found in many interstellar environments - from cold clouds such as the RMC, to relatively warmer environments such as protoplanetary discs. The CO molecule has a dipole structure, and can therefore not only be excited electronically, but both vibrationally and rotationally. Changes in the rotational quantum number J and the vibrational quantum number v can occur simultaneously, leading to ‘ro-vibrational’ emission or absorption.

When dealing with vibrations, a rough analogy to a stringed musical instrument (such as a guitar) can be drawn. A ‘fundamental’ oscillation occurs when the string vibrates with the only stationary points, or nodes, being the two end points of the string. In the case of CO, this fundamental transition is characterised by changes in the vibrational quantum number being one, e. g. $\Delta v = 1$. A ‘first overtone’ oscillation occurs when the guitar string has three stationary points, at the beginning, middle, and end of the string. For CO, this first overtone transition occurs when $\Delta v = 2$, and can be thought of as a more rapid vibration of the molecule.

Within these vibrational states, there are many rotational transitions where the change in rotational quantum number can be plus or minus one, $\Delta J = \pm 1$. The P-branch of rotational transitions is associated with $\Delta J = +1$ transitions, and the R-branch is associated with $\Delta J = -1$ transitions. For values of $J \sim 50$, the energies of the R-branch transitions reach a maximum, and then begin to decrease for higher values of J . Thus, a ‘pile up’ around the wavelength of the $J \sim 50$ transition occurs as the energies begin to decrease. This can be seen in the top

panel of Figure 1.5, where the upper level of each J transition is plotted against the vacuum wavelength of emission, for the $v = 2 - 0$ vibrational transition.

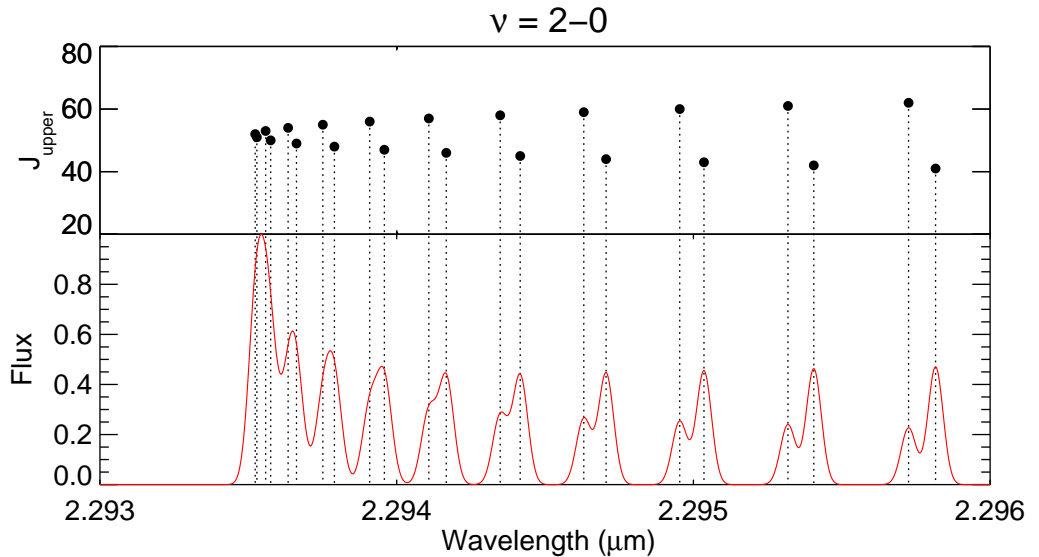


Figure 1.5: A schematic of the $v = 2 - 0$ CO bandhead at $2.2935 \mu\text{m}$. The upper panel shows the J transition numbers and their respective wavelengths, while the lower panel shows the corresponding spectrum produced by CO gas with a temperature of 4000 K , a density of 10^{23} cm^{-2} and an intrinsic line width of 5 km s^{-1} .

The resulting emission from an isothermal slab of CO is shown in the lower panel of Figure 1.5. The pile-up of transitions causes a peak to appear in the spectrum at $2.2935 \mu\text{m}$, with further, more separated emission at increasing wavelengths. This is the CO first overtone $v = 2 - 0$ ‘bandhead’, showing a distinctive saw-toothed appearance. Bandheads also occur for the other vibrational transitions.

The CO first overtone bandheads are excited in warm and dense gaseous environments ($T = 2500\text{--}5000 \text{ K}$, $n > 10^{11} \text{ cm}^{-3}$). They emit in the near-infrared at approximately $2.3 \mu\text{m}$, and therefore suffer from less extinction than emission at

optical wavelengths. This makes them ideal probes of the environments of inner circumstellar discs, where temperatures and densities are high and where extinction prevents direct observations. Comparison of observations of this emission spectrum with models of discs (Carr, 1989; Chandler *et al.*, 1995; Najita *et al.*, 1996; Wheelwright *et al.*, 2010) has provided useful dynamical information on scales that are currently unresolvable, making this a particularly powerful technique in the study of young stellar objects.

1.4 An introduction to this thesis

This thesis contains a study of both modelling and observations of molecules within circumstellar discs. Chapter 2 presents a model of the chemistry in gravitationally unstable protoplanetary disc. Such massive discs are thought to exist around young, Class 0, low mass stars. It is found that the spiral density waves induced by the unstable disc affect the chemistry in three ways; by desorbing molecules from dust grains in to the gas phase, by providing extra energy for new reactions to take place within the gas phase, and by mixing the internal structure of the disc to provide a rich chemistry near the midplane.

Chapter 3 presents high resolution near-infrared spectra of 20 massive young stellar objects. The spectra contain CO first overtone bandhead emission, which is thought to occur in the conditions expected from circumstellar discs. The emission is modelled under the assumption it originates from such a disc, and good fits are found to all objects. On average, the temperature and density structure of the discs correspond to being geometrically thin, spread across a wide range of inclinations. The discs are located within the dust sublimation radius, providing strong

evidence that the CO emission originates in small scale gaseous discs, supporting the scenario in which massive stars form via disc accretion.

Chapter 4 presents medium resolution near-infrared spectra of 5 Herbig Ae & Be stars. The spectra contain both CO first overtone and Br γ emission - both of which can be used to determine accretion rates. The strength of the Br γ emission is measured and an accretion rate for the objects is calculated. The CO emission is modelled in a similar way to the MYSOs, but using a disc model that constrains the mass accretion rate. It is found that the spectral resolution of the data is not sufficient for such fitting to be performed. High resolution archival data of one of the targets is presented, and it is shown that the disc model is unable to fit the high resolution data. It is concluded that high resolution data are needed to properly model the CO emission, and that the model constraining the mass accretion rate should be used with caution when fitted to low resolution data. Finally, the thesis is summarised in Chapter 5 where possible extensions and future work is discussed.

Chapter 2

Chemistry in a gravitationally unstable protoplanetary disc

2.1 Introduction

The chemical evolution of protoplanetary discs has been widely investigated in recent years. Observations made with the Plateau de Bure Interferometer (Dutrey *et al.*, 2007; Henning *et al.*, 2010) and the Submillimeter Array (Qi *et al.*, 2008) have provided images of protoplanetary discs in an increasing variety of molecular line emissions. The field was advanced further by the completion of the Submillimeter Array Disc Imaging Survey (Öberg *et al.*, 2010, 2011). It will be revolutionised through the use of the Atacama Large Millimetre/submillimetre Array (ALMA), which will allow much weaker lines to be investigated, and thus will enable the characterisation of a more diverse range of processes (Guilloteau & Dutrey, 2008; Semenov *et al.*, 2008).

Many authors (e.g., Aikawa *et al.*, 1996, 1999, 2002; Bergin *et al.*, 2003; Fogel

et al., 2011; Gorti & Hollenbach, 2004; Heinzeller *et al.*, 2011; Ilgner *et al.*, 2004; Markwick *et al.*, 2002; Nomura & Millar, 2005; Nomura *et al.*, 2009; Walsh *et al.*, 2010; Willacy, 2007; Willacy *et al.*, 2006; Woitke *et al.*, 2009b) have used physical disc models, together with chemical evolution networks to present computational results for the chemical composition of protoplanetary discs with varying degrees of sophistication in terms of how the physical parameters of the disc were presented, most importantly the temperature and density.

The most simple studies of the chemistry are single point models, in which a single temperature T_i and density ρ_i specify the disc properties. In more sophisticated models, the variations of temperature $T(r)$ and density $\rho(r)$ are continuous functions of radius, and the disc is assumed to be infinitely thin in the vertical direction (see Willacy *et al.*, 1998). In even more advanced models, the radial and vertical variations within the disc are decoupled, and the vertical variations of temperature and density are given at discrete radial points, $T(r_i, z)$ and $\rho(r_i, z)$ (see Aikawa *et al.*, 1999; Ilgner *et al.*, 2004; Markwick *et al.*, 2002). More recently, models have considered the full two-dimensional variation of temperature and density within the disc, $T(r, z)$ and $\rho(r, z)$, under the assumption that the disc is axisymmetric (see Walsh *et al.*, 2010).

These models have had much success in reproducing the chemical conditions in circumstellar discs typical of Class I type YSOs or T Tauri systems. However, in the earliest stages of Class 0 YSOs, when accretion rates are high, discs may become massive enough to trigger gas-phase gravitational instabilities (GIs, see Boley, 2009; Vorobyov & Basu, 2005, 2006, 2009). The stability of a disc to gravitational instabilities can be quantified by the Toomre Q parameter, $Q \equiv \frac{c_s \kappa}{\pi G \Sigma}$

(Toomre, 1964). A thin disc becomes gravitationally unstable when the material becomes dense enough to overcome the support against gravity, i.e. when $Q < 1$. A disc with non-negligible vertical extent becomes unstable when $Q \lesssim 1.5$ (Durisen *et al.*, 2007).

Discs that are gravitationally unstable produce dynamic, non-axisymmetric structure in the form of spiral waves. These spiral waves cause shocks and discontinuities in the temperature and density of the gas (see Durisen *et al.*, 2007, for a review). Under some conditions, the spiral structure will create bound fragments (Boley & Durisen, 2010; Boley *et al.*, 2010; Boss, 2001; Mayer *et al.*, 2004, 2007; Stamatellos *et al.*, 2007; Vorobyov & Basu, 2010), and therefore this mechanism may offer a route toward planet or stellar companion formation. However, the conditions under which disc fragmentation occurs are still under debate (see, e.g., Boss, 2007; Cai *et al.*, 2010; Lodato & Clarke, 2011; Meru & Bate, 2011; Podolak *et al.*, 2011).

In a disc that does not fragment, the gravitational torques caused by this spiral structure lead to significant mass transport (Boley *et al.*, 2006, 2007a; Cossins *et al.*, 2009; Gammie, 2001; Lodato & Rice, 2004; Mejía *et al.*, 2005; Michael *et al.*, 2011). This mass transport may have implications for disc driven outbursts, and recently successful models for FU Orionis outbursts have been developed for the assumption that GIs dominate mass transport beyond disc radii of a few au in non-fragmenting discs (Armitage *et al.*, 2001; Zhu *et al.*, 2009, 2010b). Simulations (Zhu *et al.*, 2010a) including layered accretion in the Dead Zone (Gammie, 1996) as well as transport by GIs show that, when discs accrete from rapidly rotating cloud cores, disc masses can become comparable to those of their central stars. Simple

models for disc evolution overlook the episodic heating induced by GI spiral shocks in massive discs (Boley & Durisen, 2008).

In this chapter, we present results from a chemical model of a relatively massive ($0.39 M_{\odot}$), young protoplanetary disc in which gravitational instabilities cause the formation of spiral waves. Section 2.2 outlines the physical model and chemical network we have utilised, and the assumed initial conditions used. Section 2.3 contains results for the time-dependent fractional abundances within an individual fluid element and column density maps of the entire disc for different species in the chemical network. A comparison of results from this model with those of other models of disc chemistry are also given. Finally, Section 2.4 presents conclusions based on the results and comments on further avenues of research.

2.2 Methods

2.2.1 The physical disc model

A hydrodynamic simulation of a massive ($0.39 M_{\odot}$) protoplanetary disc around a solar mass star is used as the basis for the physical input to the chemical network. Most of the mass in the disc initially extends from a radial distance $r \sim 7$ to 50 au from the central, solar-mass protostar. The system represents a Class 0 or early Class I object, which would likely evolve into an F-type main sequence star. The disc is modelled using CHYMER (Boley, 2007, 2009), which is briefly described here. The equations of hydrodynamics with self-gravity are solved on a fixed, cylindrical Eulerian grid. The simulation is split into 256, 128 and 64 zones in r , ϕ and z , respectively, with a physical resolution of $\Delta r = \Delta z = 0.25$ au. Mirror symmetry about the midplane of the disc is assumed. All grid boundaries have

outflow conditions which allow mass to leave the global disc simulation, where the inner boundary is set to approximately 4 au, but no mass enters from outside the disc. The central star is allowed to move freely, and the equation of motion for it is integrated as described in Boley (2009). The equation of state described in Boley *et al.* (2007b) is used, with a fixed ortho-to-para ratio of hydrogen molecules of 3:1. The fractional mass abundances of hydrogen, helium and more massive elements are set to $X = 0.73$, $Y = 0.25$, and $Z = 0.02$, respectively. However, these quantities are only relevant for the evolution of the physical model. Because the hydrogen is almost entirely in molecular form, the mean molecular weight is taken as 2.33 amu. To account for external heating, the incident stellar radiation field on the disc is assumed to have a black body spectrum with a temperature varying as

$$T_{\text{irr}} = 140 \left(\frac{r}{\text{au}} \right)^{-0.5} + 10 \text{ K} \quad (2.1)$$

and radiative cooling of the gas is accounted for using the approximation described in Boley (2009), which ensures numerical stability when the gas temperature is far from the incident irradiation temperature.

The initial disc model is prepared using the method described in Boley & Durisen (2008). An analytic disc model is first created, with $Q \sim 1$ throughout most of the disc. The spiral instability sets in around $Q \sim 1.7$ (Durisen *et al.*, 2007), so the initial model represents conditions before a strong burst of gravitational instabilities, as might be expected during the earliest stages of disc evolution. A flat Q profile with the irradiation law noted above requires the surface density to roughly follow $\Sigma \propto r^{-1.75}$. This initial configuration is assumed to undergo Keplerian rotation and have an adiabatic index of 5/3. These assumptions about the

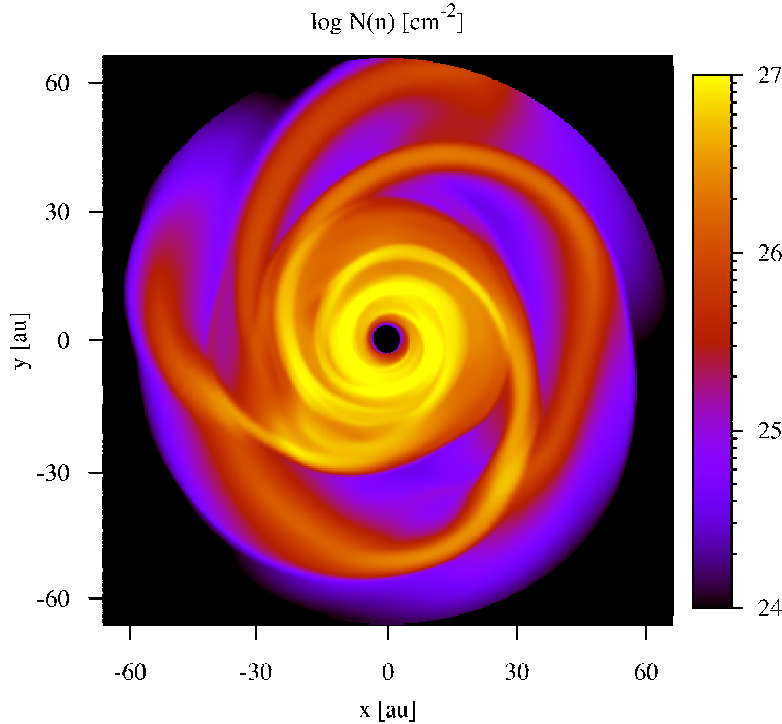


Figure 2.1: Column density of nuclei in the disc, viewed from above, at the end of the simulation where $t = 388$ years.

initial rotation and value of the adiabatic index can lead to large radial oscillations at the start of the simulation due to the associated deviations from equilibrium. To avoid some of this behaviour, the analytic model in CHYMERa is evolved at low azimuthal resolution (8 zones) for 500 yr, which is about two orbital periods near $r \sim 45$ au. The disc is then loaded on to a higher resolution grid, and a 5% cell-to-cell random noise is added to the density distribution, which seeds the growth of non-axisymmetric structure. This is considered to be the time $t = 0$ in the initial disc. The disc is then run at higher azimuthal resolution for an additional 388 yr. Figure 2.1 shows the column density of nuclei for the disc viewed from above at the end of the simulation.

At the start of the full simulation ($t = 0$), 1000 fluid elements are randomly dis-

tributed throughout the disc, weighted by mass. These fluid elements are evolved along with the main simulation, and their physical histories are recorded using a spline interpolation (Boley & Durisen, 2008). By the end of the simulation, 5 fluid elements were lost through grid boundaries, leaving 995 elements with complete thermal histories. 963 of these were used to study the chemical evolution in the disc. Results for the 32 remaining fluid elements were not used to generate chemical results because discontinuities in the physical conditions created difficulties for the integration of the chemical rate equations. The 32 elements were randomly distributed in the disc at the end of the simulation, and had not passed through shocks near the end of the dynamical calculation, so their influence on the chemical results was negligible. Figure 2.2 shows the distribution of the final locations of the fluid elements used in the chemical modelling.

Figure 2.3 shows the maximum line-of-sight temperature T_{\max} and the mass-averaged temperature,

$$T_n = \frac{\int nT dz}{\int n dz}, \quad (2.2)$$

along the line-of-sight for a face-on view of the final disc. Here n is the number density of nuclei (see Equation 2.3), T is the temperature and dz is an infinitesimal path length along the line-of-sight. The maximum and mass-weighted line-of-sight temperatures were calculated from the full hydrodynamic model results, rather than from the properties of the fluid elements used in the chemical calculations, because the full hydrodynamic model results provide higher spatial resolution.

The spiral structure is clearly seen in the maximum line-of-sight temperature map. The structure is also seen in the mass-averaged temperature map, but is somewhat less sharply defined. The difference in the maps is due to the high

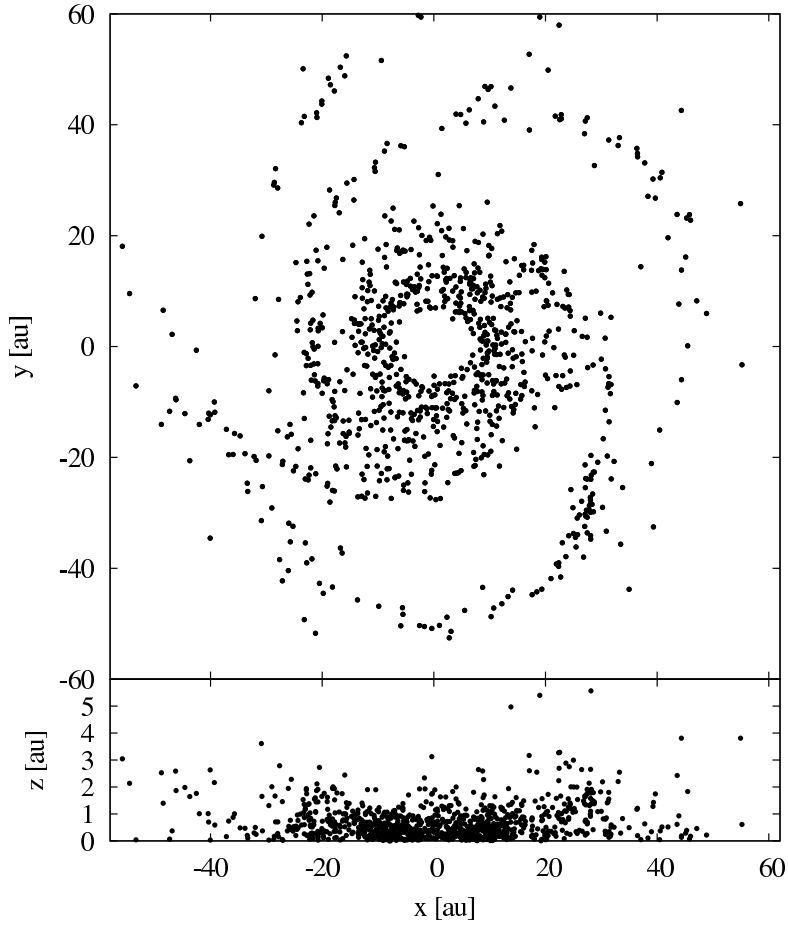


Figure 2.2: The final location of the fluid elements used to sample the disc, at $t = 388$ yr.

temperature region being somewhat, but not highly, limited in extent. It lies near the midplane and contains only a fraction of the disc mass.

Figure 2.4 shows results, taken from the complete hydrodynamical data, for the temperature and number density of nuclei in planes containing the rotation axis and either the North-South axis (y) or the East-West axis (x) from Figure 2.2. The temperature is less than 150 K outside the inner 20 au of the disc, while within it, the temperature can reach up to 350 K. The number density plot shows that the highest density gas lies in the spiral structures at approximately 10 au

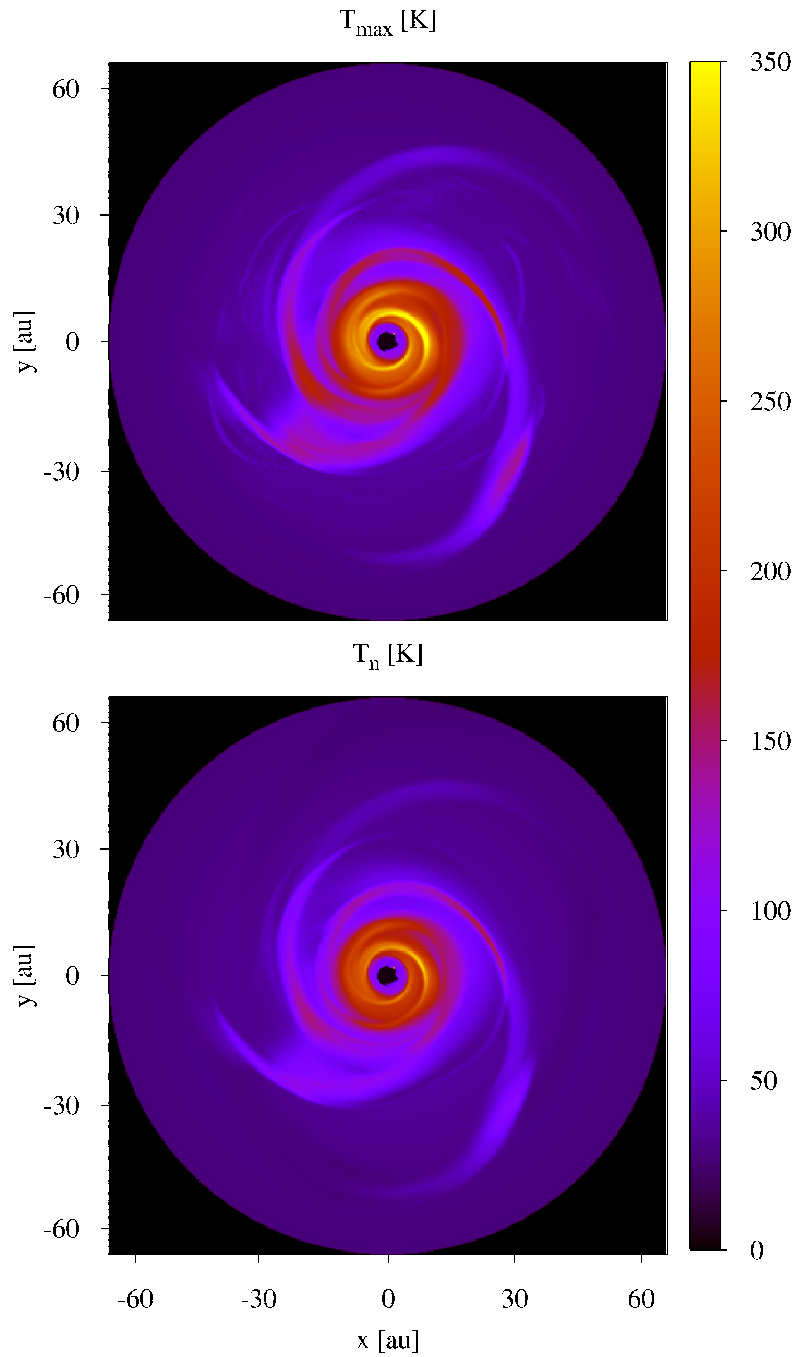


Figure 2.3: Maximum line of sight temperature (top) and mass averaged temperature (bottom) of the disc at $t = 388$ yr.

from the centre.

The temperature and density histories of the fluid elements shown in Figure 2.2 form the physical input to the chemical model. Figure 2.5 shows the evolution of the temperature and density of one of the fluid elements. This element begins at 0.8 au above the midplane, approximately 30 au from the centre of the disc. It follows a nearly circular path that slowly increases in radius. After one-and-a-half orbits, or 270 yr, it encounters the first shock. Both shocks do not affect the circular motion, but instead cause the element to rise to approximately 1.8 au above the midplane of the disc.

The results for this track provide a useful example, because the fluid element experiences a relatively quiescent period for 270 yr, before encountering the shocks. These shocks rapidly raise the temperature to a maximum of 140 K and the number density to 10^{13} cm^{-3} . The temperature and density appear to peak at the same time and drop together. This is due to the increase in the pressure caused by a shock driving an expansion of gas parallel to the shock and obliquely to the midplane of the disc that begins almost immediately behind the shock (see Boley & Durisen, 2008).

2.2.2 The chemical model

The chemical computation is based on a network of rate equations involving 1334 reactions and 125 species containing the elements H, He, C, O, N, Na and S. These reactions were originally selected from a subset of the UMIST Rate 95 database (Millar *et al.*, 1997b). Data from the Kinetic Database For Astrochemistry, KIDA¹ (Wakelam *et al.*, 2012), were used to update some of the rates and rate coefficients.

¹<http://kida.obs.u-bordeaux1.fr>

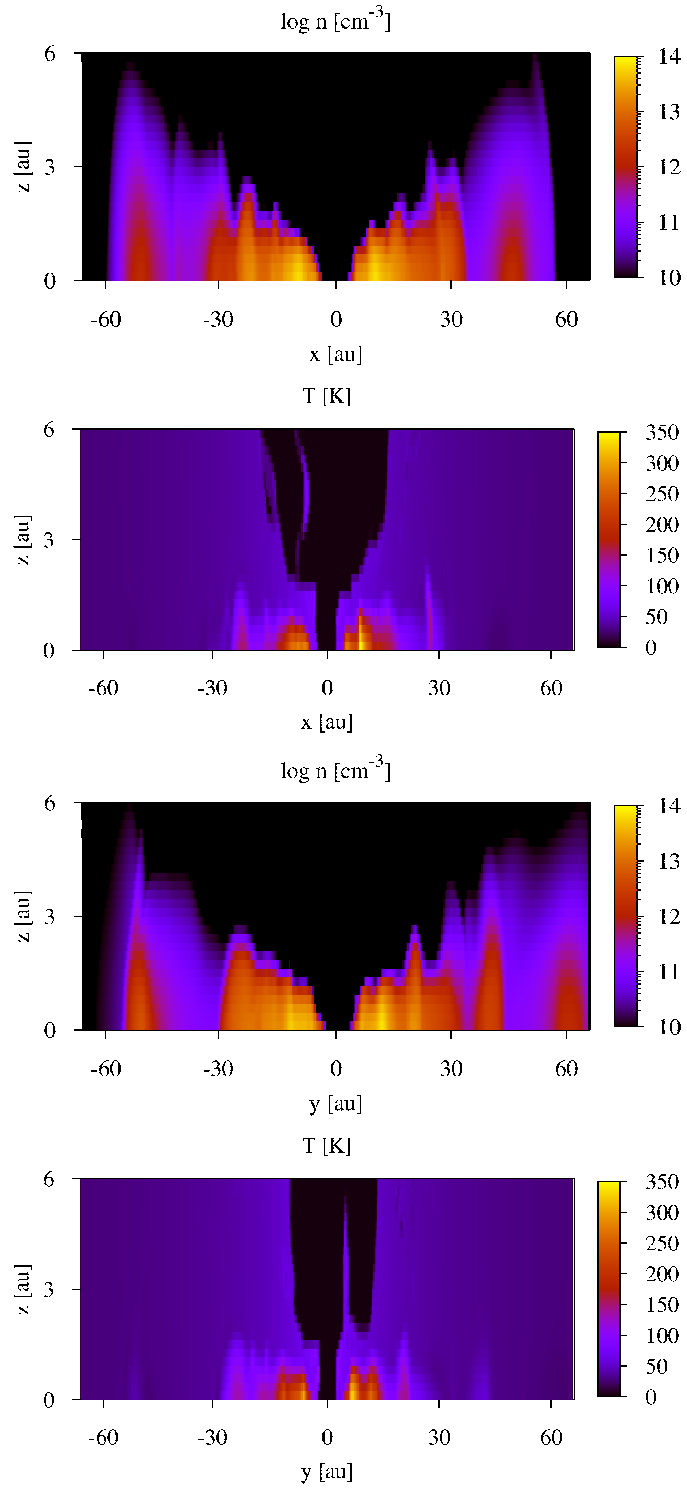


Figure 2.4: Slices of the disc interior showing number densities and temperatures at $t = 388$ yr. The x -axis here corresponds to a slice along the x -axis of Figure 2.1 where $y = 0$, and vice versa.

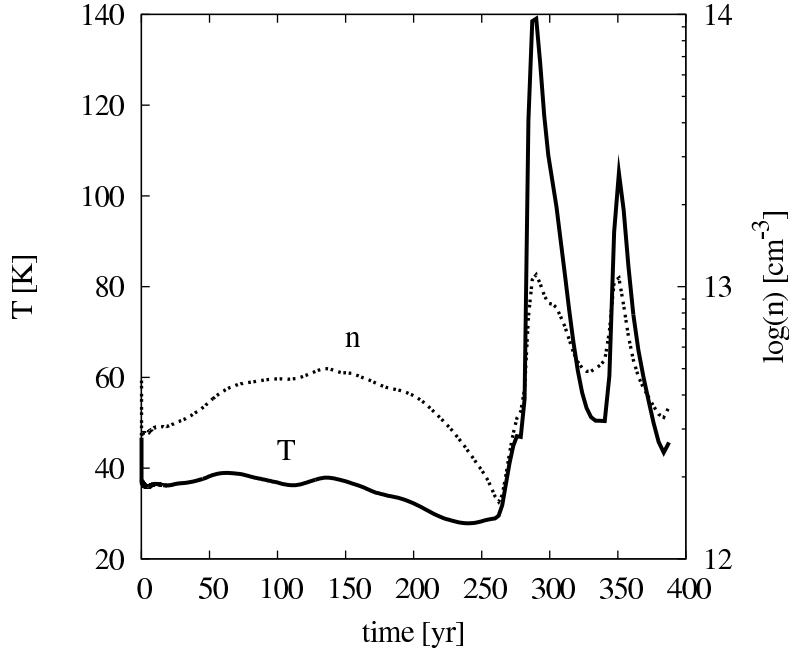


Figure 2.5: Temperature and number density history of a fluid element from the disc. This particular element encounters a shock at about 270 and 350 yr.

The network was expanded to include thermal desorption processes and some three-body reactions (discussed in detail below).

At each time-step in the chemical network (which differ from the time-steps considered in the physical model), the temperature and mass density of each fluid element are derived with cubic spline fits to the data provided for the element from the physical history. These interpolated values of the temperature and mass density are then used in the time-integration of the rate equations. The number density of nuclei, n , is calculated from the mass density, ρ , by

$$n = \frac{N_A}{M} \rho = n_H + n_{He} + n_Z, \quad (2.3)$$

where n_H , n_{He} and n_Z are the number densities of hydrogen, helium and more massive nuclei, respectively. We have assumed a molar mass of $M = 1.28 \text{ g mol}^{-1}$,

which is appropriate for a relative abundance of helium-to-hydrogen of 0.09 with trace amounts of more massive elements.

Initially, the chemical rate equations were integrated using the GEAR integration method. However, this was unable to cope with the rapid changes in temperature and density experienced by some of the fluid elements. The program was rewritten to use the DVODE integration method (see Brown *et al.*, 1989) to obtain the fractional abundance, $X(i) = n(i)/n$, of each species.

The rate equation for the gas-phase fractional abundance of the i th species is

$$\begin{aligned} \frac{d}{dt}X(i) = & \sum_{j,l,m} k(j)X(l)X(m)n - \sum_{j',m} k(j')X(i)X(m)n \\ & - 2 \sum_{j''} k(j'')X(i)^2n - \Gamma_{\text{cr}}(i)X(i) + S_3(i) + S_{\text{a,d}}(i), \end{aligned} \quad (2.4)$$

where $k(j)$ is the rate coefficient of the j th reaction and the summations are restricted so that only reactions involved in the formation or removal of the i th species are included. $\Gamma_{\text{cr}}(i)$ is the rate at which direct cosmic-ray ionisation and cosmic-ray-induced photoemission remove species i . $S_3(i)$ and $S_{\text{a,d}}(i)$ are source terms due to three-body reactions and adsorption on to and desorption from grain surfaces, respectively. We assume that the only third body of importance is H_2 , an assumption which introduces only an insignificant error. Thus,

$$\begin{aligned} S_3(i) = & \sum_{j,l,m} k(j)X(l)X(m)X(\text{H}_2)n^2 \\ & - \sum_{j',m} k(j')X(i)X(m)X(\text{H}_2)n^2 \\ & - 2 \sum_{j''} k(j'')X(i)^2X(\text{H}_2)n^2. \end{aligned} \quad (2.5)$$

Rate coefficients and rates

A brief summary of the forms of the gas phase rate coefficients and rates that were adopted is presented here. More detail can be found in the primary paper on the UMIST Rate 95 database (Millar *et al.*, 1997b). The reaction rates and coefficients that we use are provided online¹.

The rate coefficient for the j th two- or three-body reaction is of the standard Arrhenius form

$$k(j) = \alpha(j) \left(\frac{T}{300} \right)^{\beta(j)} \exp \left(\frac{-\gamma(j)}{T} \right), \quad (2.6)$$

where $\alpha(j)$ is the room temperature rate coefficient of the reaction (at 300 K), $\beta(j)$ describes the temperature dependence and $\gamma(j)$ quantifies the activation energy of the reaction.

The rate for the destruction of species i due to cosmic rays is given by

$$\Gamma_{\text{cr}}(i) = a(i)\zeta + \frac{\zeta P(i)}{1 - A}, \quad (2.7)$$

where $a(i)$ is a proportionality constant, $\zeta = 10^{-17} \text{ s}^{-1}$ is the cosmic ray ionisation rate, $P(i)$ is a constant and A is the dust grain albedo, which we take to be 0.5. Because the two terms on the right represent the physically distinct processes of direct cosmic ray induced ionisation and of destruction due to photoemission induced by the collisions of molecular hydrogen with energetic electrons produced by the ionisation, data tables give $a(i)$ and $P(i)$ separately. Though photoabsorption of radiation from external sources will affect the chemistry in the outer layers of a disc, we focus on the bulk of the disc material and assume that it is well shielded

¹<http://www.ast.leeds.ac.uk/~pyjdi/chemdisc/network.txt>

from external sources of photons, as would be the case in an embedded Class 0 YSO. Thus, we neglect photoabsorption, other than that of cosmic-ray-induced photoemission.

Gas-grain reactions

With minor exceptions, we assume that no surface chemistry occurs, though we recognise that surface chemistry is important in establishing the chemical initial conditions that we adopt. The exceptions concern the neutralisation of ions, which we assume occurs when they are adsorbed onto dust grains. While studies of the chemistry of discs including surface reactions and grain evolution have been performed (Henning *et al.*, 2010; Schreyer *et al.*, 2008; Semenov *et al.*, 2010; Semenov, 2011; Vasyunin *et al.*, 2011), such chemistry remains very uncertain. This is why we have assumed that the initial abundances reflect those of cometary ices (see Section 2.2.3).

The term $S_{a,d}(i)$ has contributions due to adsorption and desorption, and we take

$$S_{a,d}(i) = S_d(i) - S_a(i), \quad (2.8)$$

where

$$S_a = \pi a^2 S(i) \eta \sqrt{\frac{8kT}{\pi \mu m_H}} X(i) n. \quad (2.9)$$

The sticking coefficient $S(i)$ is set to unity, and we take the ratio of the number density of dust grains to the number density of nuclei to be $\eta = 3.3 \times 10^{-12}$, which is appropriate for a dust grain radius and grain-to-gas mass ratio of about $a = 0.1 \mu\text{m}$ and 0.01, respectively. T_g is the gas temperature, k is the Boltzmann constant, μ is the molecular mass in amu and m_H is the mass of a hydrogen atom.

We treat thermal desorption in the same way as Visser *et al.* (2009), and

$$S_d(i) = 1.26 \times 10^{-21} \sigma f(i) \nu_0(i) \exp\left(\frac{-E_b(i)}{k T_d}\right), \quad (2.10)$$

where σ is the surface density of binding sites, which we take to be $1.5 \times 10^{15} \text{ cm}^{-2}$. $E_b(i)$ is the binding energy of the i th species on the surface of the dust grain, T_d is the dust temperature (which we assume to be in equilibrium with T_g), the factor $f(i)$ represents the fraction of the surface of the dust grain covered by the i th species, given by

$$f(i) = \min\left(1, \frac{X^s(i)}{\eta N_b}\right), \quad (2.11)$$

where $X^s(i)$ is the solid fractional abundance of the i th species and N_b is the typical number of binding sites per grain, taken to be 10^6 . The characteristic vibrational frequency of the species attached to the grain is given by

$$\nu_0(i) = \sqrt{\frac{2\sigma E_b(i)}{m(i)\pi^2}}, \quad (2.12)$$

where $m(i)$ is the mass of the i th species (Hasegawa *et al.*, 1992). The binding energies were taken from Hollenbach *et al.* (2009), references therein, and the OSU database¹.

2.2.3 Chemical initial conditions

The initial gas phase fractional abundances were assumed to have the same ratios as the fractional abundances of the corresponding ices in comet Hale-Bopp as given by Ehrenfreund & Charnley (2000), and they are given in Table 2.1. Comets are

¹<http://www.physics.ohio-state.edu/~eric/research.html>

Table 2.1: Initial fractional abundances used for the chemical network ($X(i) = n(i)/n_{\text{H}}$).

Species	Abundance	Species	Abundance
He	1.00×10^{-1}	H ₂ CO	1.83×10^{-6}
C	3.75×10^{-4}	CO ₂	3.67×10^{-5}
CO	3.66×10^{-5}	HCN	4.59×10^{-7}
CH ₄	1.10×10^{-6}	HNC	7.34×10^{-8}
N	1.15×10^{-4}	S	1.62×10^{-5}
NH ₃	3.30×10^{-6}	H ₂ S	2.75×10^{-6}
O	6.74×10^{-4}	SO	1.47×10^{-6}
H ₂ O	1.83×10^{-4}	SO ₂	1.84×10^{-7}
Na	3.50×10^{-5}	OCS	3.30×10^{-6}

thought to have undergone significant chemical processing at the edges of discs, so this assumption may not be entirely appropriate. However, comparisons between the compositions of cometary ices and interstellar ices imply a general consistency between the two, though some discrepancies exist (Ehrenfreund & Charnley, 2000; Ehrenfreund & Schutte, 2000).

2.2.4 Timescales

As mentioned previously, the hydrodynamical simulation following the disc evolution is run at higher resolution for 388 yr. This is far longer than the orbital period of about 4 yr at the inner boundary and somewhat shorter than the orbital period of 390 yr at 60 au. Nearly all of the mass is at less than 50 au where the period is about 300 yr, and the gravitational instability develops fully and leads to well established spiral structure in about 200 yr. The spiral structure roughly corotates with the material between about 30 and 40 au; the orbital period at 35 au is 180 yr. The disc is not steady, and the mass infall rate varies with radius and

time from a factor of a few smaller than to a factor of a few larger than $10^{-4} M_{\odot}$, which implies a radial flow time of the order of 10^4 yr. These timescales are much longer than the shortest chemical timescales which are associated with adsorption and desorption; using Equation 2.9, one finds that the adsorption timescale for a number density of 10^{13} cm^{-3} is roughly an hour. The desorption timescale is very much larger or smaller, depending on the temperature.

The full simulation time of 388 yr is sufficient to allow the spiral shocks to develop fully. This disc is already exhibiting spiral structure that is typical in GI-active discs over many orbits. The purpose of the hydrodynamical simulation is to provide self-consistent shock profiles for the chemical model, which was achieved in a relatively short period of evolution.

We follow the chemistry of each fluid element through ten cycles of the temperature and number density history associated with it (e.g., the history shown in Figure 2.5), where in each subsequent cycle, we used the final fractional abundances from the previous cycle as initial input. Of course, this resulted in rapid variations in the physical conditions as each new cycle began. However, we followed the chemical evolution in this way to keep the amount of data produced by the model at manageable levels. We found that the chemical behaviour for a fluid element became periodic by the time that the chemistry had gone through ten cycles. All results presented here are from the final cycle, and we consider that $t = 0$ occurs at the beginning of that final cycle.

At the start of each integration, we used a logarithmically increasing time-step, which was initially 90 s. This allowed initially rapid reactions, such as the adsorption of species on to grains at the beginning of the first cycle, to be followed

with sufficient resolution. We limited the maximum time-step to approximately 10^3 s to avoid missing details in rapidly changing shock features.

2.3 Results & Discussion

The chemistry of the entire disc was calculated using the physical histories of the fluid elements described previously. Here we consider the chemistry in one fluid element as an illustrative example of the effect of shocks on the chemistry of the material.

2.3.1 An individual fluid element

Figure 2.6 shows the fractional abundances of 17 species (CO, SO, NH₃, H₂O, H₂S, OCS, O₂, HCO, HCO⁺, HNO, SO₂, CS, HCS, HCS⁺, HCN, HNC and OCN) as functions of time during the final cycle for the fluid element for which the density and temperature are given as functions of time in Figure 2.5.

The shocks induce increases in the gas phase fractional abundances of all 17 species. However, the increase in $X(\text{CO})$ is too small to be apparent from the figure, because nearly all CO is in the gas phase even in the coldest regions of the disc.

The increases of the fractional abundances of species for which results are shown in the upper two right hand panels of Figure 2.6 are due almost entirely to thermal desorption from the surfaces of dust grains. We define $N_g(i)$ to be the average number of molecules of the i th species on a grain. For each species for which results are given in those panels, $N_g(i)\eta + X(i)$ is nearly constant. This is due to adsorption and desorption being the only processes significantly affecting

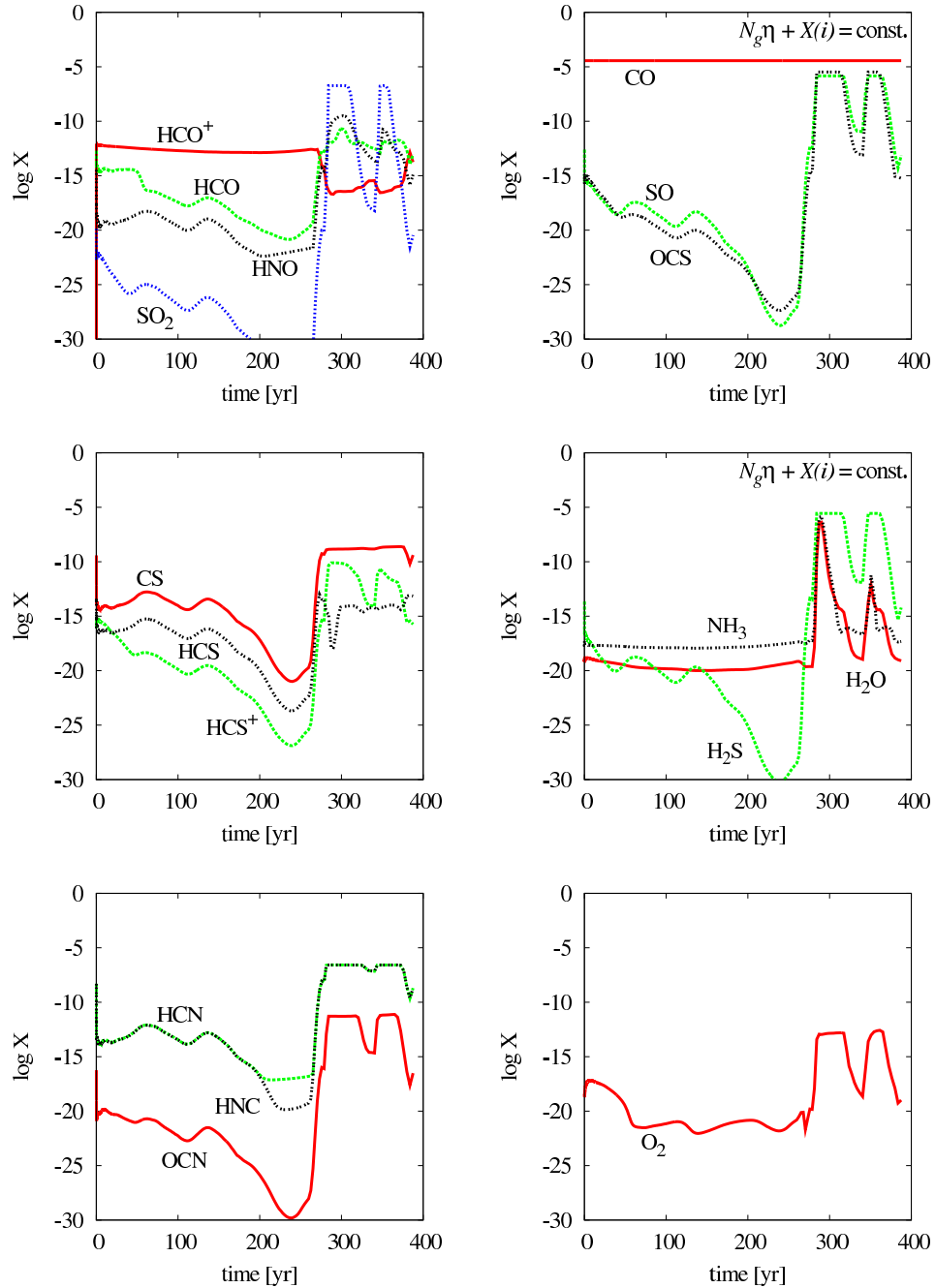


Figure 2.6: Fractional abundances of species as functions of time for the fluid element for which the physical structure is shown in Figure 2.5. The relatively cold, quiescent period for the first 270 yr shows the abundance of most species decreasing due to adsorption, or staying constant.

the gas phase fractional abundances of these species, and the fractional abundance of each of them depends almost entirely on the temperature only.

The fractional abundances of species for which results are shown in the other panels of Figure 2.6 are affected significantly by gas phase reactions, as well as desorption and adsorption. The higher temperatures in the shocks allow some reactions with activation energies and some endothermic reactions to occur at significant rates. Also species which undergo reactions that are exothermic and have small or no barriers are desorbed into the gas phase in shocked regions.

HCS is one species having a fractional abundance that is affected by gas phase reactions. It is formed by the reaction of S and CH₂. CS is formed by reactions of C with SO, and S with CN in almost equal proportions. OCN is formed by the reaction of CN and O₂. HNO forms by the reaction of NH₂ and O, and HCO forms mainly via NH₃⁺ reacting with H₂CO. The reaction of O with OH contributes to O₂ production throughout much of the disc; O₂ is also formed in the shocked regions by the reactions of He⁺ with CO₂ and SO₂.

2.3.2 The disc - face on

A major aim of the work reported here is the identification of the general features that should appear in images of gravitationally unstable protoplanetary discs obtained in molecular line emissions. Thus, here we present model column density maps for a number of molecular species.

The final spatial positions of the fluid elements constitute an irregular grid for which the model fractional abundances are known. The QHULL and QGRID3 interpolation routines contained within the IDL 5.5 libraries were used to obtain

the fractional abundances at the points of a three-dimensional regular Cartesian grid. The mass density at each of those grid points was calculated from the mass density distribution at the final time given by the full hydrodynamic results. We used the mass density distribution given by the full fluid results because the grid for which it was calculated is much more uniform than the grid for which the chemical results are available. Thus, for regions of low mass density, we were able to obtain more accurate interpolated results for the mass density than for the fractional abundances.

The column density $N(i, x, y)$ of the i th species on a line of sight perpendicular to the disc is

$$N(i, x, y) = \int nX(i, x, y, z) dz. \quad (2.13)$$

As the model only provides fractional abundances for the $z > 0$ region of the disc, we assumed that n and all $X(i, x, y, z)$ s are even functions of z when performing the integrals. This produced column densities representative of a disc spanning a full range of z -values, for the assumption of mirror symmetry about the midplane. Figures 2.7 and 2.8 show the column densities of selected species.

For each species for which results are given in Figure 2.7, $N_g(i)\eta + X(i)$ is nearly constant. This is due to adsorption and desorption being the only processes significantly affecting the gas phase fractional abundances of these species. Thus, the structure seen in each of these column densities is due to the variations in temperature and density and is not influenced by gas phase chemistry.

The quantity $N_g(i)\eta + X(i)$ is not constant for each of the species for which Figure 2.8 shows a gas phase column density map. Gas phase chemistry significantly affects the gas phase fractional abundance of each of these species. We have

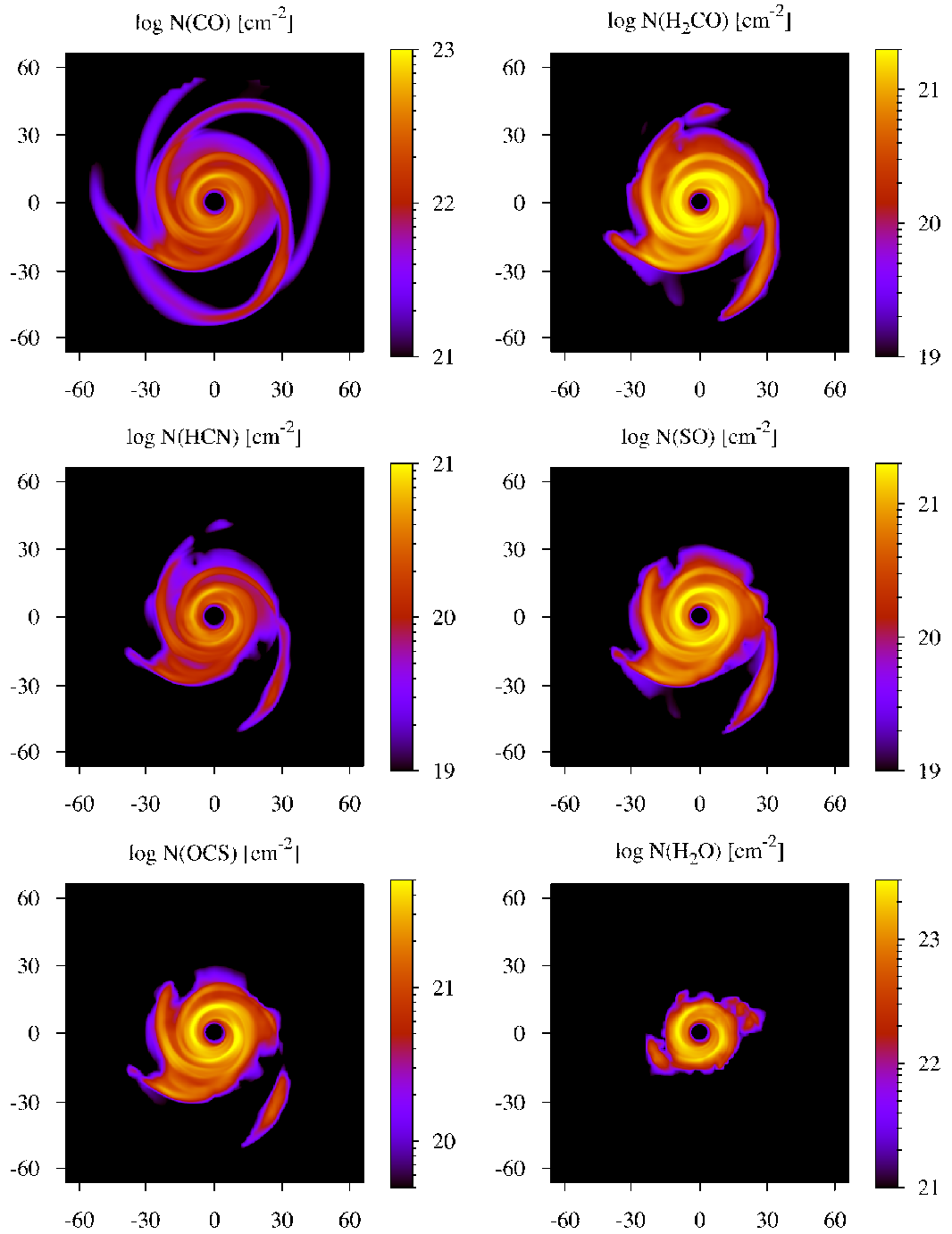


Figure 2.7: Gas phase column densities of molecules having gas phase fractional abundances determined primarily by desorption and adsorption, at $t = 388$ yr. Distances from the disc centre are in au.

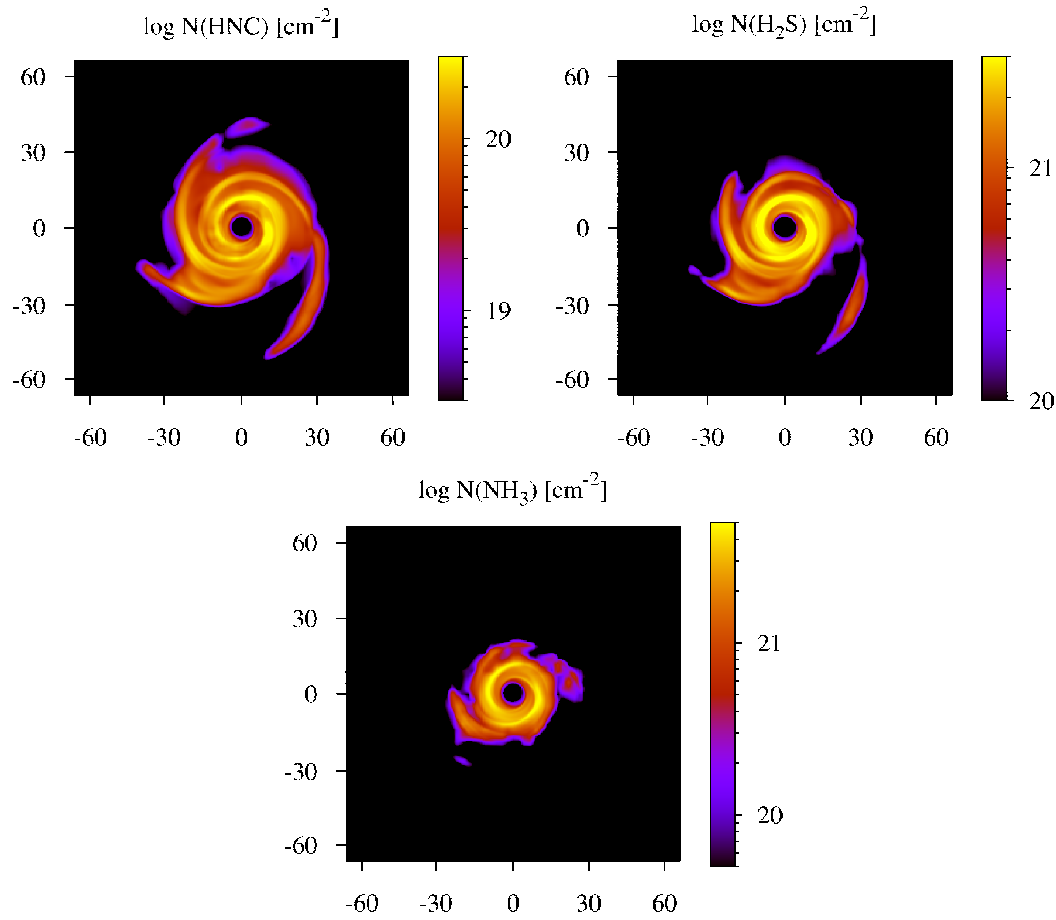


Figure 2.7: Continued.

already given some explanation for the evolution of most of the species for which results are displayed in Figure 2.8 in Section 2.3.1. The HCO^+ is anti-correlated with the H_2O and other species with which it charge exchanges. HCS^+ is also removed by charge exchange with H_2O , but its distribution differs somewhat from that of HCO^+ . This is due to CS being abundant in the gas phase only in regions in which it is efficiently desorbed and CO being abundant everywhere in the disc. Reactions of H_3^+ with CS and CO produce these ions.

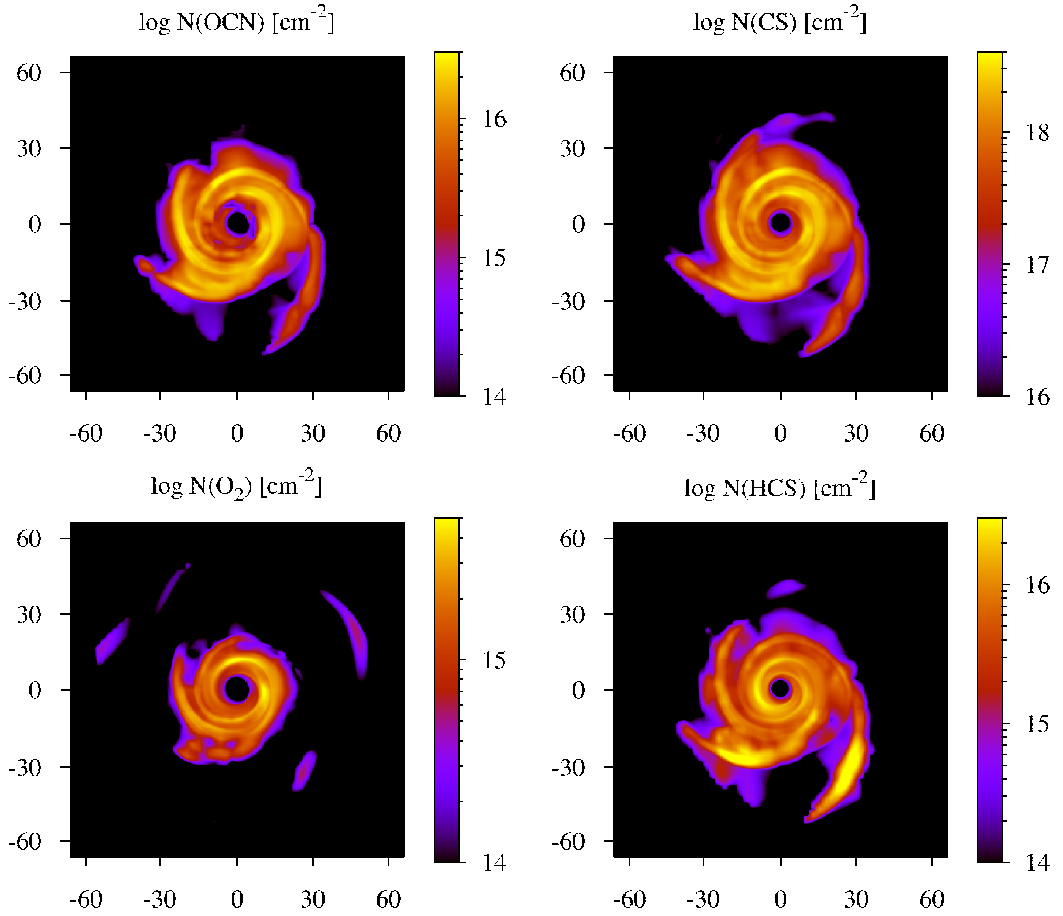


Figure 2.8: Column densities in the disc for several gas phase molecules whose total abundance (gas and surface) varies with time, at $t = 388$ yr. Distances from the grid centre are in au.

2.3.3 The disc - other perspectives

Figure 2.9 shows the column densities of selected species in the disc as viewed along the y -axis, toward $y = 0$, in Figure 2.1. Most of the edge-on maps show little structure (as with CO and H₂O), though some, such as the H₂CO and SO maps, show slightly higher column densities on the right side due to the presence of a large spiral arm in the disc.

Figure 2.10 shows slices of the fractional abundances in the interior of the disc

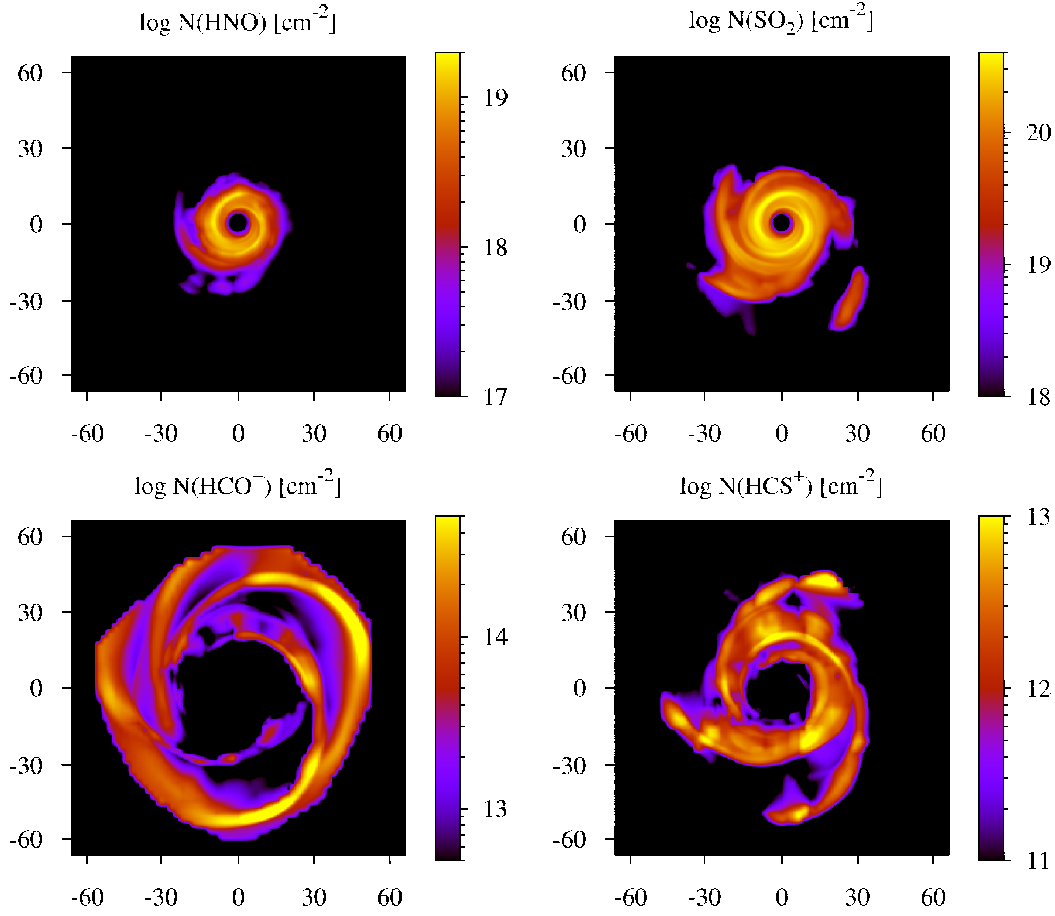


Figure 2.8: Continued.

for HCN and H_2CO . The spatial resolution of these maps are lower than the others presented because they have not been combined with the higher resolution physical data from the full simulation. Nevertheless, these slices of the disc interior clearly show that there is a large degree of homogeneity in the fractional abundances of species throughout the disc.

2.3.4 The effect of three-body reactions

The chemistry in each of several fluid elements was calculated both with the three-body reactions included and with them excluded. These three-body reactions

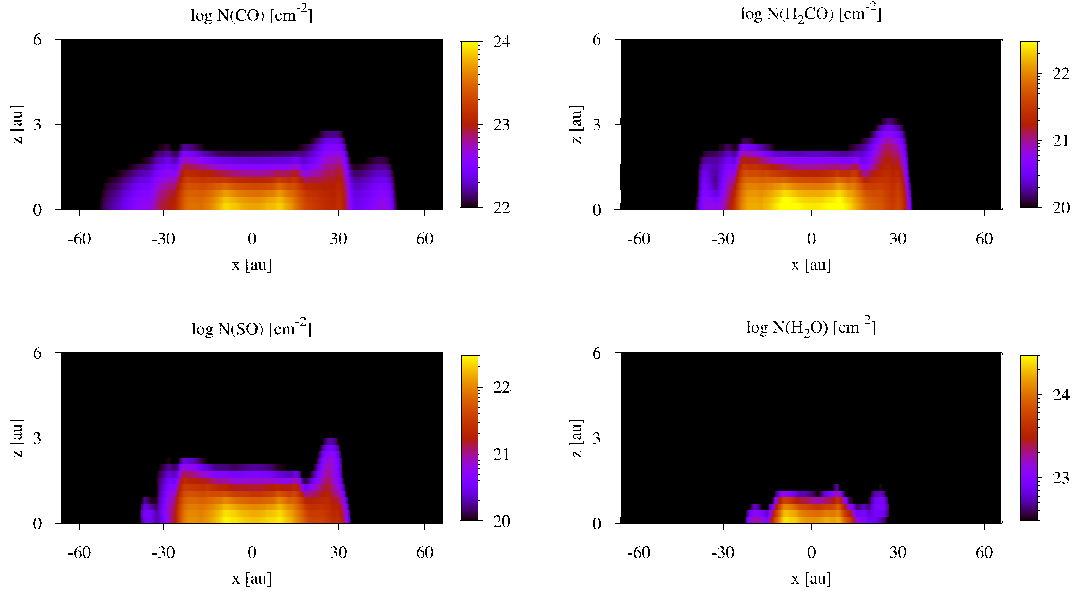


Figure 2.9: Column densities of the disc as viewed along the y -axis of Figure 2.1, towards $y = 0$, at $t = 388$ yr.

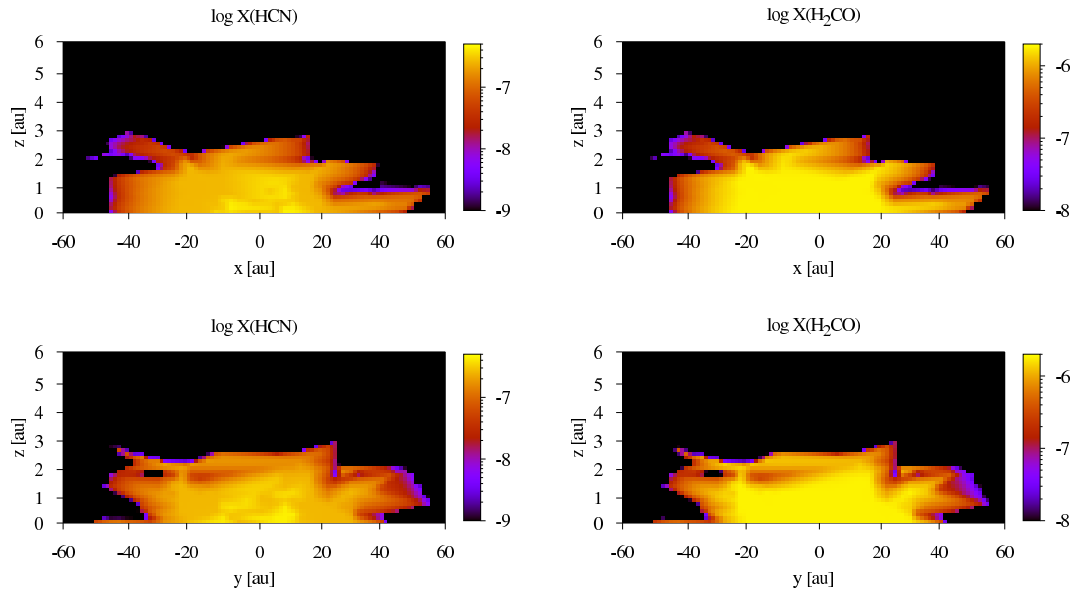


Figure 2.10: Slices of the fractional abundance of disc interior, oriented as in Figure 2.4, interpolated from the positions of the fluid elements at $t = 388$ yr.

occur primarily at high densities, and as expected, the largest differences occur in the denser inner regions of the disc and spiral arms, where $n > 5 \times 10^{26} \text{ cm}^{-2}$. However, even there the effects were insignificant for all species except some with low fractional abundances ($X(i) < 10^{-10}$).

A reduction of the fractional abundance of O_2 in one element from approximately 10^{-14} to 10^{-21} in a shocked region and an enhancement in the fractional abundance of NH from approximately 10^{-17} to 10^{-14} were amongst the most pronounced effects of including the three-body reactions. Species with fractional abundances higher than approximately 10^{-10} were not noticeably affected by the addition of the three-body reactions. All results that are presented were obtained with the three-body reactions included.

2.3.5 Comparison with other models

The three-dimensional nature of our chemical model and the qualitatively different dynamics of the disc make a direct comparison of our results with the previously existing chemical results for axisymmetric models of lower mass discs difficult. However, we give a rough comparison between the maximum fractional abundances of species given by our model and some obtained by others who have investigated chemistry for disc models. The results taken from the other papers are somewhat inaccurate because they were obtained through the examination of figures from which precise information was hard to infer. Table 2.2 shows the maximum fractional abundances recorded at the end of our simulation and the corresponding values from Walsh *et al.* (2010) and Ilgner *et al.* (2004) (hereafter W2010 and I2004 respectively).

Table 2.2: Maximum abundances reported in this work, W2010 and I2004. A dash signifies no data for that species were available in the original paper.

Species	Maximum log $X(i)$		
	This work	W2010	I2004
HCO ⁺	-10.8	-6	-14
HCN	-6.4	-6.5	-
CN	-7.8	-7.5	-
CS	-8.0	-8	-10
C ₂ H	-10.5	-7	-
H ₂ CO	-5.7	-9	-
N ₂ H ⁺	-19.6	-11	-
H ₂ O	-3.7	-4	-
CO ₂	-4.5	-4.5	-
OH	-12.8	-4	-14
S	-9.9	-	-15
SO	-5.8	-	-10
SO ₂	-6.5	-	-7
HCS ⁺	-12.5	-	-21
NH ₃	-5.5	-	-5

Our results are comparable to those of the other models for NH₃, SO₂, H₂O, CO₂, CN and HCN. We obtain a higher fractional abundance of HCO⁺ than I2004, but less than reported in W2010. Our fractional abundances of C₂H and N₂H⁺ are lower than those of W2010. However, we report a much higher fractional abundance of H₂CO.

Some of the discrepancies between the results of W2010 and I2004 arise because W2010 considered a much more extensive fraction of the disc than I2004, who studied only the material at radii less than 10 au. We studied material at radii between 10 and 60 au, where spiral structure and shocks are important in our dynamical model. Thus, in further discussion of the differences between our results

and those of others, we focus on a comparison of our results and those of W2010.

Some of these differences are due to the assumptions that we made concerning the initial chemical conditions. As mentioned earlier, in our model a number of species have gas phase abundances that depend only on the assumed initial conditions and the balance between desorption and absorption. H_2CO in particular is such a species. So its high abundance in our model compared to that found by W2010 is due to our assumption of a higher H_2CO abundance and neglect of species as massive as CH_3OH . Similarly, our assumption that no nitrogen is initially in N_2 leads to a lower abundance of N_2H^+ than found in W2010.

The high values of the HCO^+ and C_2H given for W2010 occur in regions with densities that are about four orders of magnitude lower than any that we consider. The chemistry in these low density regions is affected by the diffusion that W2010 assume to occur, but which we do not consider. The mid-plane value obtained by W2010 for the fractional abundance of HCO^+ for radii of 10 to 60 au is comparable to the maximum value that we report for it; this is to be expected because in both models most of the CO is in the gas phase, and HCO^+ is formed by a simple ionisation triggered reaction sequence. The mid-plane value obtained by W2010 for the fractional abundance of C_2H for radii of 10 to 60 au is less than the maximum value that we report for it; this is due to the desorption, caused by shock induced heating, occurring near the mid-plane in our models.

The slices of the disc interior in our model can be qualitatively compared to axisymmetric models, such as those in W2010. Figure 2.11 shows this comparison for the fractional abundances of H_2CO . The region from 0-60 au in the W2010 plot corresponds to the extent of our disc. It can be seen that the stratification in

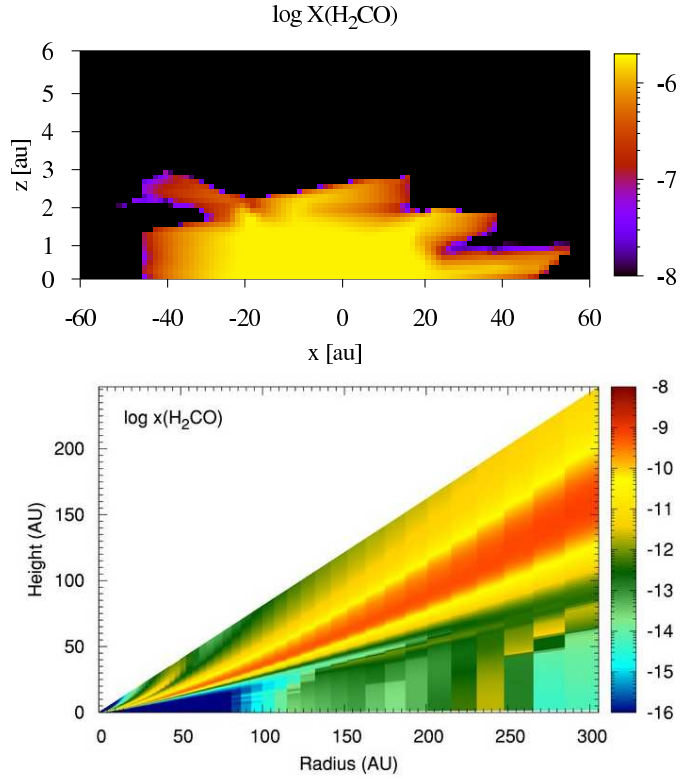


Figure 2.11: Comparison of slices of the disc interior showing fractional abundances of H₂CO in this work (top) and W2010 (bottom). Taken from Walsh *et al.* (2010).

W2010 is not present in our model, due to the mixing caused by the spiral shocks. Similar results were found for the other chemical species that were included in both models. However, our work cannot be directly compared to these axisymmetric models, because they are meant to represent a later stage of disc evolution in which the assumption of this symmetry is entirely appropriate. Rather, consideration of the chemical processing occurring in discs such as the one presented here could be used as the input to such models, to properly address the processing possibly occurring in young discs.

2.4 Conclusions & Future Work

We have constructed a chemical model of a $0.39 M_{\odot}$ protoplanetary disc, surrounding a solar-mass star, representative of a Class 0 or early Class I young stellar object. In the disc, gravitational instabilities cause spiral waves. The shocks associated with these waves induce the desorption of various chemical species from the surface of dust grains and increase their gas phase abundances. Though the gas phase fractional abundances of some of the species are not significantly affected by gas phase chemistry, some of the desorbed species are reactive. In some cases, the elevated temperatures in the shocked regions enhance the reactivity.

As most of the mass is concentrated in spiral structures, all of the gas phase molecular column densities show spiral structures. However, the structures are limited in extent in some species, e.g. H_2O , which possess the highest binding energies to grains, therefore higher temperatures are needed for desorption to occur. This also limits the extent of structure in species which form in the gas phase from these tightly bound species. Consequently, maps of the emissions of a number of species will reveal where shocks of differing strengths are and, thus, serve as diagnostics of the disc dynamics.

We find that three-body reactions have little effect on the chemistry of species with fractional abundances above 10^{-10} . Though they are most important in the hotter, densest regions of the disc, they do not alter the overall chemistry of the disc significantly.

A direct comparison of our results with those of other models is not straightforward, due largely to the very different nature of the disc dynamics that we have used. Some differences between the peak gas phase fractional abundances that we

obtained and those reported in other papers are due to the assumptions that we have made about chemical initial conditions. However, the major differences in the chemistry away from the outer boundaries of the disc arise from the fact that some other modellers assume diffusion plays an important role in enhancing the richness of the chemistry in the disc interior (e.g. Heinzeller *et al.*, 2011; Ilgner *et al.*, 2004); in many of these models, the chemistry at the midplane is not very rich over a very large fraction of the disc. In contrast, our model gives rise to substantial gas phase abundances near the midplane, even though we have not assumed that efficient microscopic mixing is a consequence of large-scale turbulence. Though inclusion of such mixing would be difficult in an approach in which individual fluid elements are followed, we have not neglected that type of mixing for that reason. Rather, we have chosen to focus on how gravitational instability generates shocks whose mixing of the disc material induces a rich gas phase chemical composition in the disc interior, even near the midplane.

ALMA will revolutionise observational studies of discs. For example, if used to observe a disc in the Taurus-Auriga cloud complex, ALMA, with its 5 milliarcsec resolution, will allow the mapping of features on scales of about 1 au, which is smaller than the widths of the prominent spiral structures of our model. The chemical results presented here are being used in the construction of radiative transfer models (Douglas *et al.*, 2013), to assess the observability of these structures using the molecular emission of various species. This will allow investigation of the different physical regimes, and will determine whether this spiral structure does indeed exist within massive, young protoplanetary discs.

Chapter 3

CO bandhead emission of massive young stellar objects

3.1 Introduction

Confirming the presence of discs around MYSOs presents a considerable observational challenge. Such objects are relatively rare, and still embedded in molecular cloud material, making them optically invisible and highly extinguished. There have been a handful of detections of discs around MYSOs (see Carrasco-González *et al.*, 2012; Jiménez-Serra *et al.*, 2007; Kraus *et al.*, 2010; Patel *et al.*, 2005) but the disc properties are difficult to determine. Observations at longer wavelengths (such as the far infrared and submillimetre) only probe disc properties at large distances from the central protostar. Furthermore, very few studies can be conducted with sufficient angular resolution to probe astronomical unit sized scales, which is necessary to study the inner regions of circumstellar discs. The exception is the observation of the MYSO G310.0135+00.3892 with the Very Large Telescope Interferometer (VLTI) and AMBER (Petrov *et al.*, 2007) reported by Kraus *et al.*

(2010), which achieved a maximum resolution of approximately 10 au. This provided unique information on the geometry of the K -band continuum emitting material. However, this study involved only a single object. Therefore, observations of a large sample of MYSOs using an alternative method that can probe close to the central protostar are required.

The inner regions of gaseous discs are difficult to access observationally, especially as near infrared (NIR) interferometric studies are limited to isolated objects which are bright in the near-infrared (Tatulli *et al.*, 2008; Wheelwright *et al.*, 2012b). Therefore, to study the inner discs of MYSOs, we must employ indirect methods. The CO molecule is an ideal tracer of these regions because the coupled rotational and vibrational excitation causes a distinctive emission feature, the CO bandhead, so called because they appear in bands in low-resolution spectra. The first overtone $v = 2-0$ bandhead emission at $2.3 \mu\text{m}$ occurs in warm ($T = 2500-5000 \text{ K}$) and dense ($n > 10^{11} \text{ cm}^{-3}$) gas. These are the conditions expected in the inner regions of accretion discs. This makes CO bandhead emission a valuable tool that allows us to trace these regions. In addition, because this feature is the result of transitions across a range of energy levels (and therefore, temperatures), it also allows us to probe the physical properties throughout the disc. Previous studies of CO bandhead emission have been successful in fitting spectra of young stars with a range of masses under the assumption that the emission originates from a circumstellar disc (Bik & Thi, 2004; Blum *et al.*, 2004; Carr, 1989; Chandler *et al.*, 1995; Davies *et al.*, 2010; Wheelwright *et al.*, 2010), but a study involving a significant number of MYSOs has yet to be performed.

In this chapter we study a subset of the RMS database¹. An extensive low

¹<http://www.ast.leeds.ac.uk/RMS/>

resolution spectroscopic survey of RMS sources (see, e.g. Clarke, A. J., 2007; Cooper *et al.*, 2013) was used to select objects for a high resolution spectroscopic study of CO bandhead emission in massive young stellar objects. We detect CO emission in 20 MYSOs (and two non-MYSOs), which is compared to kinematic models to assess whether the emission originates in circumstellar discs. Finally, we attempt to determine the properties of the CO emitting gas and constrain the accretion rates of these objects. Section 3.2.1 details the modelling of the CO emission, while Section 3.3 outlines the observations that were performed. Section 3.5 presents the observations and model fits to the spectra, along with an analysis of the best fitting parameters. Section 3.6 discusses the findings and Section 3.9 presents conclusions from this work.

3.2 Models

3.2.1 The CO emission model

The model of CO first overtone bandhead emission is the same as that for Wheelwright *et al.* (2010), which was based on the work of Kraus *et al.* (2000) and is described here. For an isothermal slab of CO gas with excitation temperature T and number density n_{co} , the energy levels of the CO molecule are calculated from

$$E(v, J) = hc \sum_{k,l} Y_{k,l} \left(v + \frac{1}{2} \right)^k (J^2 + J)^l, \quad (3.1)$$

where $Y_{k,l}$ represents the Dunham coefficients which were taken from Farrenq *et al.* (1991). The population of rotational levels, up to $J = 100$, for the $v = 2 - 0$ vibrational transition is determined assuming local thermodynamic equilibrium

and using the Boltzmann distribution,

$$n(v, J) = \frac{n_{\text{CO}}}{Z} (2J + 1) \exp\left(-\frac{E(v, J)}{kT}\right), \quad (3.2)$$

where Z is the partition function, calculated from

$$Z = \sum_v \exp\left(-\frac{E(v)}{kT}\right) \sum_J (2J + 1) \exp\left(-\frac{E(J)}{kT}\right), \quad (3.3)$$

and following the prescription of Berthoud (2008) we take a maximum of $v = 15$ and $J = 110$.

Once the level populations are calculated, they are used with the transition probabilities of the respective lines to determine the resulting absorption coefficients via

$$K_\nu = \frac{c^2 n_{vJ} A_{vJ, v'J'}}{8\pi\nu^2} \left(\frac{(2J + 1)n_{v'J'}}{(2J' + 1)n_{vJ}} - 1 \right) \Phi(\nu), \quad (3.4)$$

where v, J and v', J' are the upper and lower levels of a transition, respectively, $\Phi(\nu)$ represents the intrinsic line profile (which we take to be Gaussian), and $A_{vJ, v'J'}$ is the Einstein coefficient of the transition, taken from Chandra (1996). The absorption co-efficient is assumed to be constant along the line of sight, and thus the optical depth is taken to be

$$\tau_\nu = K_\nu N_{\text{CO}}, \quad (3.5)$$

where N_{CO} is the column density of CO. The intensity of the individual lines at the surface of the isothermal slab of CO gas is therefore

$$I_\nu = B_\nu(T)(1 - e^{-\tau_\nu}), \quad (3.6)$$

where $B_\nu(T)$ is the Planck blackbody function.

Figure 3.1 shows the effect of changing various physical quantities of the CO slab on the resulting spectrum. The upper panel shows the effect of decreasing the excitation temperature of the gas. At $T = 5000$ K, the emission is dominated by the bandhead peak, but as the temperature is lowered, the relative strength of the longer wavelength emission increases, because less energy is available to excite the higher-energy transitions near bandhead peak. The middle panel shows the effect of decreasing the surface density of the slab, and the lower panel shows the effect of increasing the intrinsic linewidth $\Delta\nu$ of the line profile $\Phi(\nu)$, which shows the longer wavelength transitions blending into one another for high values of linewidth, masking the two-component signature seen in the spectra with lower $\Delta\nu$.

3.2.2 A disc of CO

To create a synthetic spectrum of CO emission within a disc, we assume a physical model (which is discussed in detail in Section 3.2.3) and split the disc region into 75 radial rings, each with 75 azimuthal cells. Each cell is assigned a temperature and surface density from the physical model. We assume the disc rotates in a Keplerian manner, and the velocity of each cell to the line-of-sight is determined assuming the disc is at an inclination i to the vertical. The emission from each cell is calculated using the method in Section 3.2.1, then weighted by the solid angle subtended by the cell on the sky, and wavelength shifted with respect to the line-of-sight velocity due to the rotational velocity of the disc. The emission from all cells is then summed together to produce the entire CO bandhead profile for the disc. Figure 3.2 shows CO first overtone spectra produced by various discs

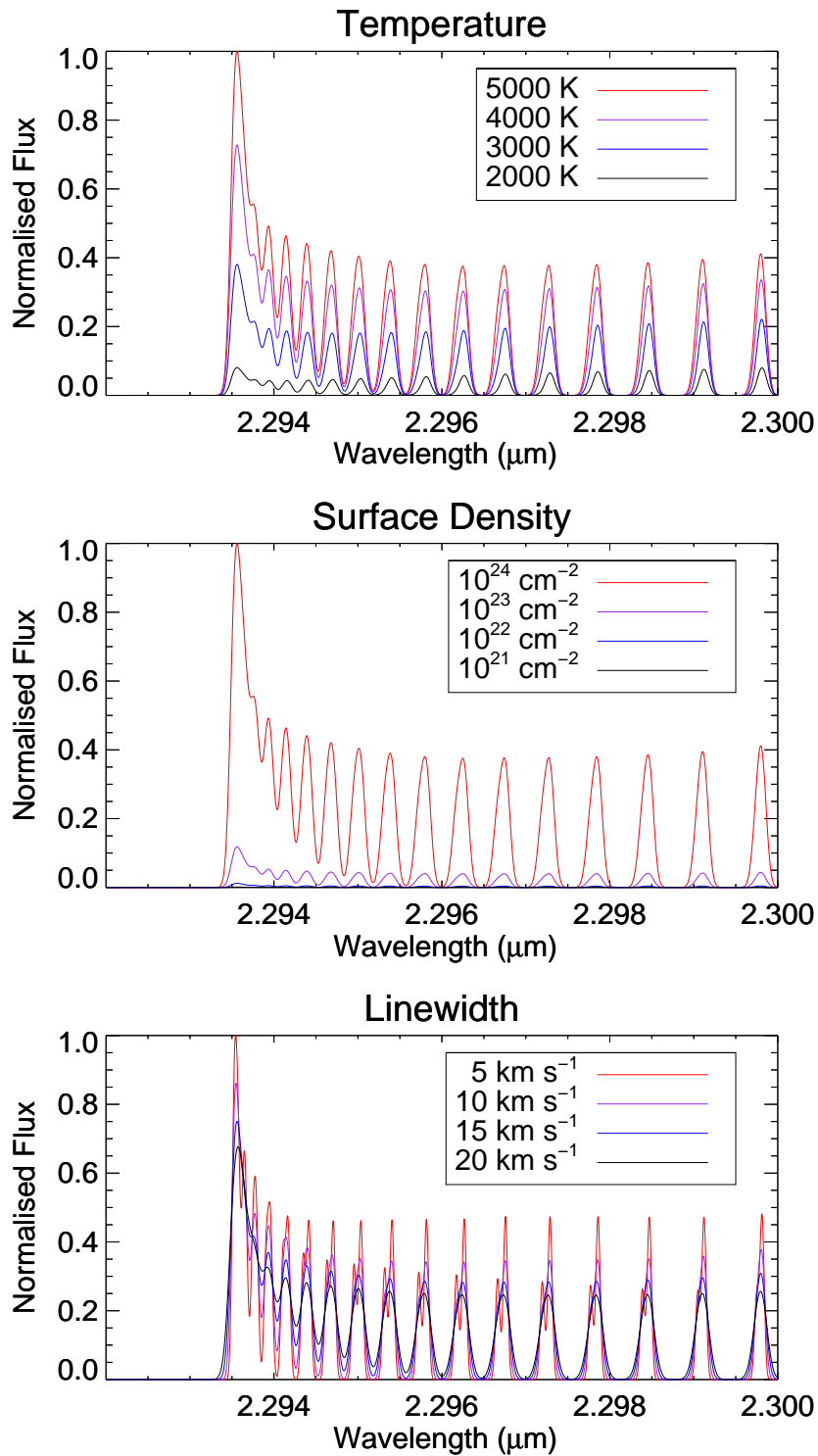


Figure 3.1: Spectra produced by a slab of CO in which the excitation temperature (upper), surface density (middle) and intrinsic linewidth (bottom) are changed while the other quantities are kept constant. The flux in each panel is normalised to the highest point of the strongest spectrum.

with identical temperature and density structure, but whose physical parameters are varied. The upper panel of Figure 3.2 shows a disc in which the inclination to the line of sight is changed. As the disc is moved from a low inclination (face-on), to a high inclination (edge-on), the rotation of the material within the disc begins to affect the spectrum. Rotational lines that were clearly distinguished at low inclinations become merged with neighbouring lines. This is because each transition now has a double peaked line profile due to the motion of the material in the disc. The peak of the bandhead widens, and a so-called ‘blue-shoulder’ on the short wavelength side of the bandhead peak appears, due to blue-shifted emission lines around the $J = 50$ transition.

3.2.3 The physical disc structure

There are several ways in which the physical parameters within the disc can be modelled. For example, Bik & Thi (2004) assume a simple isothermal disc, Berthoud *et al.* (2007) assume the surface density and temperature of the disc decrease as power laws. Carr (1989) and Chandler *et al.* (1995) determine the temperature and density structure by balancing the heating and cooling mechanisms at work on the surface of a thin α -disc (see Shakura & Sunyaev, 1973) which is isothermal in the vertical direction. The use of three different approaches to modelling the temperature and density structure of the disc have been investigated. Here, their differences are discussed.

Model A

The first model, model A, is purely analytic in nature (as in Berthoud *et al.*, 2007) and describes the excitation temperature and surface number density as decreasing

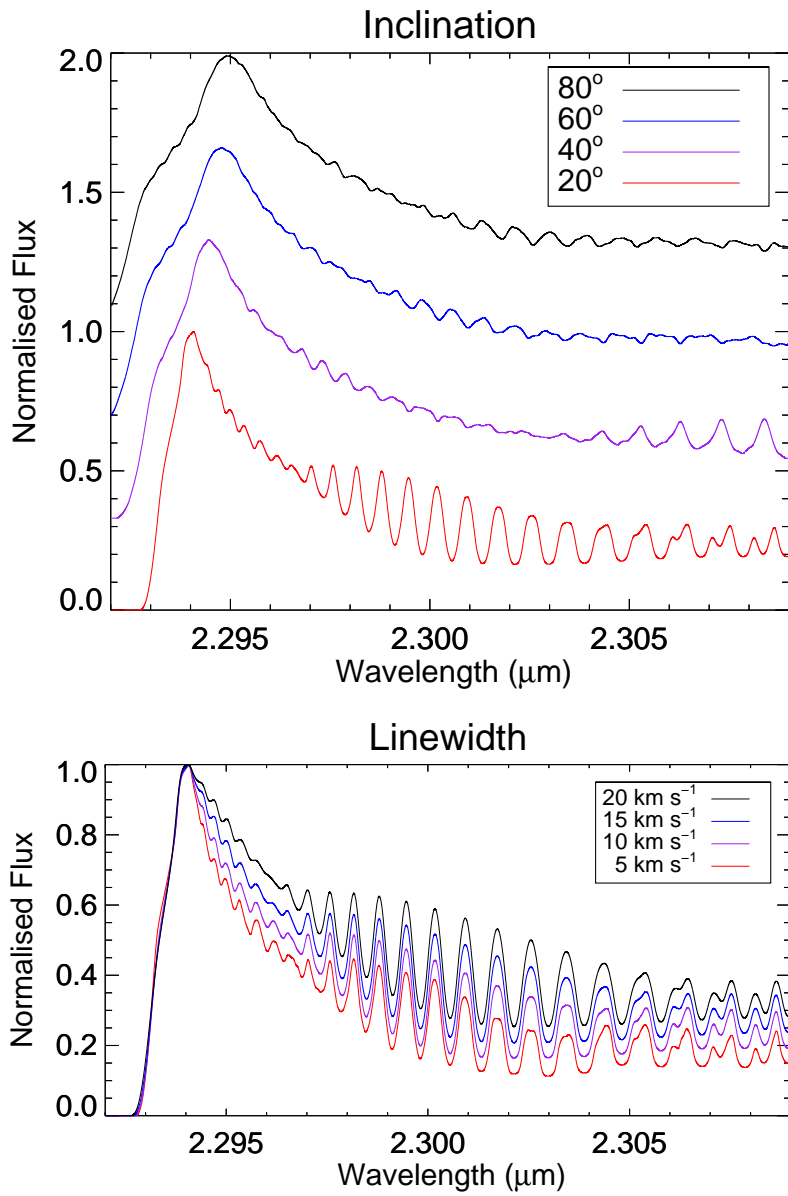


Figure 3.2: Spectra produced by discs of CO who possess identical temperature and density structures, but whose inclination (top panel) and intrinsic linewidth (bottom) panel are altered.

power laws,

$$T(r) = T_i \left(\frac{r}{R_i} \right)^p \quad (3.7)$$

$$N(r) = N_i \left(\frac{r}{R_i} \right)^q, \quad (3.8)$$

where T_i and N_i are the excitation temperature and surface density at the inner edge of the disc R_i , and p and q are the exponents describing the temperature and surface density gradient, respectively. The optical depth, τ , is taken to be the product of the absorption coefficient per CO molecule, and the CO column density. Since we are considering a geometrically thin disc, the column density is given by the surface number density N .

Model B

Our second model, model B, is based on balancing the heating and cooling descriptions of a disc as in Carr (1989), later updated by Chandler *et al.* (1995). The disc is assumed to be dominated by stellar heating, with a contribution from heating via viscosity, and thus the temperature considered is the surface temperature of the disc. The disc is assumed to be steady state, and thus has a constant accretion rate throughout. The disc is under local thermodynamic equilibrium. Finally, the disc is isothermal in the vertical direction, and is heated via absorption of the stellar radiation field and the conversion of gravitational potential energy into thermal energy via viscosity. The viscosity within the disc is described by the alpha prescription (Shakura & Sunyaev, 1973). The mass accretion rate of MYSOs is expected to be high (up to $10^{-3} M_\odot \text{yr}^{-1}$) and the discs are likely turbulent, therefore we adopt a value of $\alpha = 1.0$, corresponding to a highly viscous

disc environment. The heating via viscosity is calculated by

$$Q_{\text{acc}} = \frac{3GM_{\star}\dot{M}}{8\pi} \left(1 - \sqrt{\frac{R_{\star}}{r}}\right) r^{-3} \quad (3.9)$$

The heating by absorption of stellar radiation is

$$F_{\text{abs}} = \frac{\sigma T_{\text{eff}}^4}{\pi} \left(\phi - \frac{\sin 2\phi}{2}\right) \left(1 - \exp\left(-\frac{\tau(r)}{\sin \phi}\right)\right) \quad (3.10)$$

where $2\phi = \sin^{-1}(R_{\star}/r)$ is the angle subtended by the star at radius r . Cooling due to radiation from the disc is

$$Q_{\text{rad}} = \sigma T(r)^4 (1 - e^{-\tau(r)}). \quad (3.11)$$

To obtain the excitation temperature at a certain radius within the disc, we require that the heating and cooling rates are balanced, thus

$$Q_{\text{acc}} + F_{\text{abs}} = Q_{\text{rad}}. \quad (3.12)$$

This condition is iterated through with increasing temperatures until fulfilled, and the temperature is then set to that value. This is repeated throughout the disc. The surface number density is then calculated as

$$N = \frac{\dot{M}\mu\text{m}_{\text{H}}}{6\pi\alpha k T_{\text{eff}}} \sqrt{GM_{\star}} \left(1 - \sqrt{\frac{R_{\star}}{r}}\right) r^{-\frac{3}{2}} \quad (3.13)$$

Model C

Our third model, model C, is again based on balancing the heating and cooling mechanisms of a disc, but as described in Vaidya *et al.* (2009). In this disc, the

heating via viscosity is assumed to dominate the temperature structure, and as such the temperature here can be considered the midplane temperature of the disc. The disc is steady state and we again adopt $\alpha = 1.0$.

To determine the midplane temperature, we assume that the heating due to viscosity is as in Equation 3.9, and that the energy radiated by the disc is

$$Q_{\text{rad}} = \frac{16\sigma}{3\kappa N} T^4. \quad (3.14)$$

We balance the heating and cooling as before by requiring that $Q_{\text{rad}} = Q_{\text{acc}}$, which provides the temperature at a specific radius within the disc via iteration. The heating due to irradiation from the star is not included in this iteration because we are considering the midplane temperature of the disc, but is instead added to the temperature reported from this convergence, yielding the final excitation temperature. The number density is again determined using Equation 3.13.

In both model B and C, the mass accretion rate directly sets the temperature structure throughout the disc. The inner edge of the emission region is set to the radius at which the temperature reaches 5000 K (where we assume CO is destroyed), and the outer edge of the disc is set to where the temperature drops below 1000 K (where we assume CO is no longer sufficiently ro-vibrationally excited to be detected). The optical depth is taken to be $\tau = \kappa\rho H$ where H is the scale height of the disc, and κ is the opacity taken from Ferguson *et al.* (2005).

3.3 Observations and sample selection

Table 3.1 presents the observational parameters of the 20 MYSO, and two non-MYSO targets in our study that possessed CO emission. The data were taken using the CRIFRES near-infrared cryogenic spectrograph (Kaeufl *et al.*, 2004) on the Very Large Telescope (VLT) over three nights in June 2007. A spectral resolution of $R \sim 30\,000$ was achieved ($\Delta\lambda = 0.08\text{ nm}$ at $\lambda = 2.3\ \mu\text{m}$) using a slit width of 0.6 arcsec. Standard ABBA nodding along the slit was used. The seeing conditions varied from 0.8 to 1.2 arcsec. A single pixel element represents 0.011 nm, while a resolution element covers approximately seven pixels. Using a central wavelength of $\lambda_c = 2.286\ \mu\text{m}$, the CO emission spans chips three and four of the detector. The CO bandhead peak is located on the third detector chip. Telluric standard stars of spectral type A, featureless in the wavelength range of interest, were observed between science targets using an identical instrumental set-up and at similar airmasses to ensure similar sky conditions.

The data were reduced using the ESO provided CRIFRES pipeline, via the GASGANO data organiser (version 2.2.7). Dark current was removed and detector linearity corrections applied, then master flat frames and bad pixel maps were used to correct the spectra. The final spectra were extracted using the optimal extraction algorithm. Wavelength calibration was performed using a cross correlation with the HITRAN model catalogue (Rothman *et al.*, 1998) and OH lines. The standard stars were reduced and extracted in the same manner. The final spectra were obtained by division of the object spectra by their corresponding standard star to remove telluric spectral features. To further remove the effect of bad pixels, the spectra were cleaned using a sigma-clipping algorithm that removed any pixels

with a value above three times the standard deviation of the pre-bandhead portion of the spectrum. This was determined to be the maximum amount of cleaning that could be performed without affecting the appearance of real spectral features.

3.3.1 Observational results

The spectra, presented in Section 2.3, exhibit a range of bandhead shapes and strengths. Ten objects possess a so-called ‘blue shoulder’, in which there is prominent emission on the shorter wavelength side of the bandhead peak. This is caused by doppler-shifted rotational lines, and may be indicative of rotational motion in a circumstellar disc, or an outflowing wind (Kraus *et al.*, 2000). The other ten objects show steep rises in the bandhead slope. Several objects (for instance, G270.8247–01.1112) possess a residual telluric feature in the pre-bandhead portion of the spectrum, but this did not affect our analysis.

The signal to noise ratio of the spectra ranges from approximately 20–150. The average bolometric luminosity of the objects is $5 \times 10^4 L_{\odot}$, typical of other objects within the RMS Survey (Mottram *et al.*, 2011). The objects are generally bright in the K –band, but this is a selection effect based on observational requirements.

The objects G332.9457+02.3855 and G338.5459+02.1175 were originally classified as MYSOs, but since the observation date have been found to have too low a luminosity for this to be the case, and are likely to be lower mass young stellar objects instead. However, since they both possess strong CO emission we have included them in the final sample and discuss them in Section 3.8.

Figure 3.3 shows the bandhead of IRAS 08576–4334, which is a good example of the CO bandhead feature due to the prominent emission and the high signal-

Table 3.1: Observational information for each object. The bolometric luminosity L_{Bol} , 2MASS K -band magnitude and distance d_{kin} are all taken from the RMS database unless otherwise stated.

Object	RA (J2000)	Dec. (J2000)	L_{Bol} (L_{\odot})	K (mags)	d_{kin} (kpc)	t_{int} (h)	Blue Shoulder	Chip Four	S/N	CO σ
MYSOs										
G012.9090−00.2607	18:14:39.56	−17:52:02.3	5.4×10^4	9.2	3.8	5.0	Y	Y	63	12
G033.3891+00.1989	18:51:33.82	+00:29:51.0	1.0×10^4	7.2	5.1	0.3	N	Y	81	10
G035.1979−00.7427	18:58:12.99	+01:40:31.2	3.1×10^4	12.6	2.2	1.6	N	N	18	7
G270.8247−01.1112	09:10:30.89	−49:41:29.8	9.9×10^3	10.1	7.7	8.3	Y	Y	61	11
G282.2988−00.7769	10:10:00.32	−57:02:07.3	8.9×10^3	7.0	5.5	0.1	Y	Y	114	11
G287.3716+00.6444	10:48:04.55	−58:27:01.5	2.8×10^4	7.5	5.6	0.3	N	N	128	12
G293.8947−00.7825	11:32:32.82	−62:15:43.1	1.2×10^4	8.8	10	2.1	N	Y	102	6
G296.2654−00.3901	11:53:10.93	−62:30:20.0	4.5×10^3	8.9	8.9	2.1	N	Y	58	8
G305.2017+00.2072	13:11:10.45	−62:34:38.6	4.9×10^4	9.4	3.6	2.1	N	Y	63	18
G308.9176+00.1231	13:43:01.70	−62:08:51.2	1.4×10^5	6.4	4.6	0.1	Y	N	64	7
G310.0135+00.3892	13:51:37.85	−61:39:07.5	5.7×10^4	4.9	3.3	0.1	Y	N	120	8
G332.0939−00.4206	16:16:16.46	−51:18:25.2	1.8×10^5	5.9	3.5	0.1	-	N	58	5
G332.9868−00.4871	16:20:37.81	−50:43:49.6	2.6×10^4	9.3	3.5	3.3	Y	N	47	10
G338.9377−00.4890	16:45:08.23	−46:22:18.5	2.1×10^3	9.1	3.2	2.1	Y	N	50	7
G339.6816−01.2058	16:51:05.95	−46:15:52.4	1.6×10^4	8.5	2.6	0.3	-	N	74	4
G347.0775−00.3927	17:12:25.81	−39:55:19.9	1.8×10^3	8.5	1.6	2.1	Y	Y	62	7
IRAS08576−4334 [§]	08:59:27.40	−43:45:03.7	-	9.4	2.2	5.0	N	Y	41	40
IRAS16164−5046 [§]	16:20:11.06	−50:53:16.2	$1.0 \times 10^{5\dagger}$	9.5 [†]	3.6 [†]	5.0	Y	Y	61	14
IRAS17441−2910 [§]	17:44:09.60	−29:10:58.0	$5.2 \times 10^{5*}$	5.3	9.8 [*]	0.4	Y	Y	33	9
M8E-IR [§]	18:04:53.26	−24:26:42.3	-	4.4	1.9 [‡]	0.2	N	Y	125	12
Non-MYSOs (see Section 3.8)										
G332.9457+02.3855	16:08:12.08	−48:40:38.5	860	9.7	1.9	0.04	N	Y	36	8
G338.5459+02.1175	16:32:32.19	−44:55:30.6	16	7.2	0.3	5.0	N	Y	60	17

§: Object is not a member of the RMS database, but was selected based on previously observed CO emission. †: From Bik *et al.* (2006). ‡: From Chini & Neckel (1981). *: From Walsh *et al.* (1997). ||: Kinematic distance from the rotation curve of Brand & Blitz (1993) and $v_{\text{LSR}} = 7.5 \text{ km s}^{-1}$ (Bronfman *et al.*, 1996).

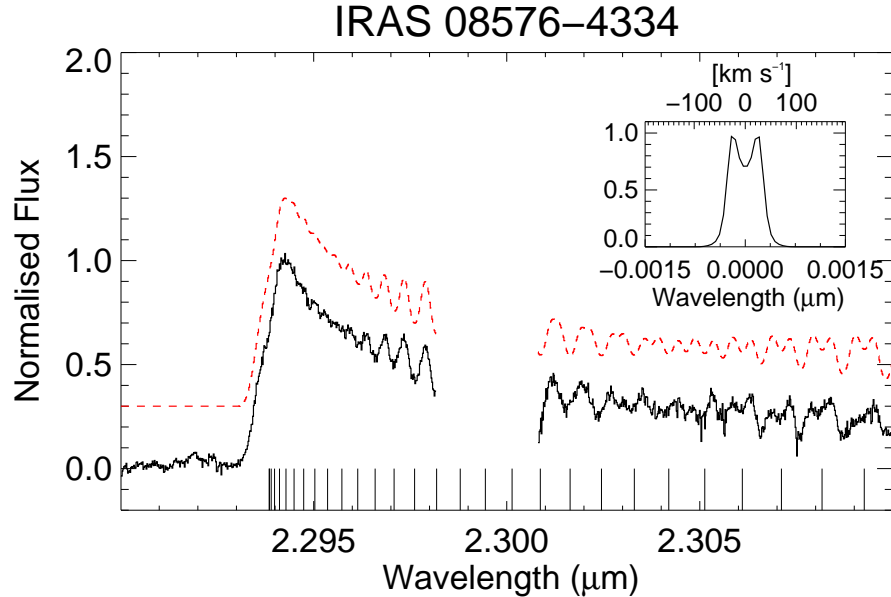


Figure 3.3: Spectrum of the first overtone bandhead emission of IRAS 08576–4334 (solid black). The gap in the data is due to the spacing between chips three (left) and four (right) of the detector. The best fitting model is shown above (dashed red) and has been shifted upwards for clarity. The theoretical wavelengths of the transitions that make up the bandhead are marked on the abscissa, and have been shifted to account for relative motion. The panel shows the line shape of the $J = 51-50$ transition that was adopted for the best fitting model.

to-noise ratio. Plotted above the data is our final best fitting model (discussed in Section 3.2.3). The inset shows the line shape of the $J = 51-50$ transition that is the result of the best fitting model, displaying a double peaked profile due to the motion in the disc.

3.4 Fitting the data

3.4.1 The fitting procedure

The best fitting model is determined using the downhill simplex algorithm, implemented by the AMOEBA routine of the IDL distribution. The input spectra are

Table 3.2: Allowed ranges of parameters for the model fitting procedure, for disc models A, B and C. Note that density refers to the surface number density.

Parameter	Used in	Range
Mass accretion rate \dot{M}	B, C	$10^{-7.5} < \dot{M} < 10^{-3.5} M_{\odot} \text{ yr}^{-1}$
Inclination i	A, B, C	$0 < i < 90^{\circ}$
Intrinsic linewidth $\Delta\nu$	A, B, C	$1 < \Delta\nu < 30 \text{ km s}^{-1}$
Inner disc radius R_i	A	$1 < R_i < 100 R_{\star}$
Inner disc temperature T_i	A	$1000 < T_i < 5000 \text{ K}$
Inner disc density N_i	A	$10^{12} < N_i < 10^{25} \text{ cm}^{-2}$
Temperature exponent p	A	$-5 < p < 0$
Density exponent q	A	$-5 < q < 0$

first continuum subtracted (which is assumed to be linear given the small range in wavelength), and then normalised to the peak of the bandhead emission. Model fits are compared to the data using the reduced chi-squared statistic, χ_r^2 , and the error in the data is taken to be the standard deviation of the flux in the pre-bandhead portion of the spectra.

The fitting routine is repeated with six starting positions spread across the parameter space to avoid recovering only local minima in χ_r^2 . Table 3.2 shows the ranges over which we search in parameter space. The stellar mass, radius and effective temperature are fixed parameters, and are calculated from the bolometric luminosity of each object using interpolation of the main sequence relationships in Martins *et al.* (2005), unless otherwise stated in Table 3.1. The free parameters of the fit are, for model A: the inner disc radius, temperature and surface density R_i, T_i, N_i , the temperature and density exponents p, q , the disc inclination i and the intrinsic linewidth $\Delta\nu$. For models B and C, the free parameters are: the mass accretion rate \dot{M} , disc inclination i and intrinsic linewidth $\Delta\nu$.

3.4.2 A test of the disc models - W33A

The object G012.9090–00.2607 (hereafter W33A) is a well known MYSO that has been studied extensively in recent years (de Wit *et al.*, 2010; Wheelwright *et al.*, 2012a), and thus offers a useful check of our models. The work of de Wit *et al.* (2010) determined the inclination of the system to be $40^\circ < i < 70^\circ$ through modelling of the SED. The spectrum of W33A was fitted using the three disc models described in Section 3.2.3, to test which is most applicable to the circumstellar environment of MYSOs. Figure 3.4 shows the data and the best fits, and Table 3.3 shows the best fitting parameters for each model.

Model A clearly gives the best fit to these data, as can be seen from both a qualitative assessment of the fit and the reduced chi-squared statistic. All models reproduce the peak of the bandhead and blue side slope well. However, only model A accurately reproduces the individual line profiles between 2.296–2.298 μm with a sufficiently small intrinsic linewidth. Models B and C both have similar chi-squared values, which are approximately twice that of model A. Furthermore, the inclinations of models B and C (13° and 27°) are too low to agree with the result of de Wit *et al.* (2010).

In addition to using the downhill-simplex algorithm AMOEBA to fit the data, the reduced chi-squared landscape for both models B and C was also investigated in a regular fashion, as can be seen in Figure 3.5. The reduced chi squared value χ_r^2 was determined for various values of mass accretion rate \dot{M} and inclination i , while the intrinsic linewidth $\Delta\nu$ was set to the best fitting value in Table 3.3. The values were changed in increments of $\log \dot{M} = 0.25 M_\odot \text{yr}^{-1}$ and $i = 2^\circ$, respectively.

The top panel of Figure 3.5 shows that fits to the spectrum of W33A using disc

Table 3.3: Best fitting parameters using disc models A, B and C for the spectrum of G012.9090–00.2607 (W33A).

Disc Model	\dot{M} ($M_{\odot} \text{ yr}^{-1}$)	Δv (km s^{-1})	i ($^{\circ}$)	χ_r^2
A	-	21	37	1.4
B	7.76×10^{-6}	29	13	2.8
C	2.14×10^{-5}	29	27	2.8

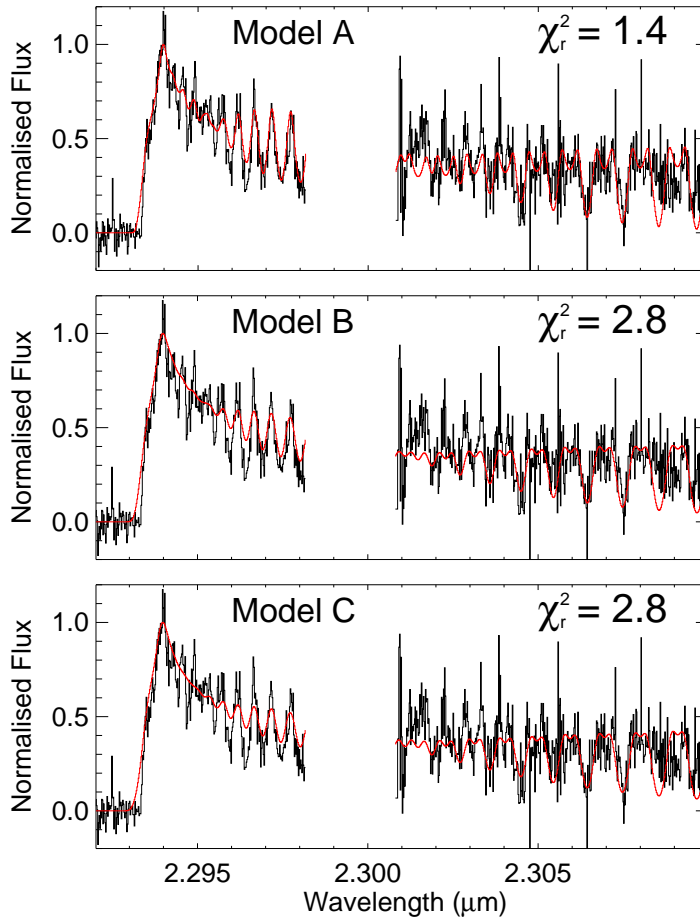


Figure 3.4: Best fitting models to G012.9090–00.2607 (W33A) using each disc model. Best fitting parameters are shown in Table 3.3. Model A provides the best fit as can be seen from the reduced chi squared statistic. Models B and C struggle to reproduce the peak to trough variation seen in the spectrum between 2.296 – 2.298 μm . All models struggle to fit the initial data points on chip four.

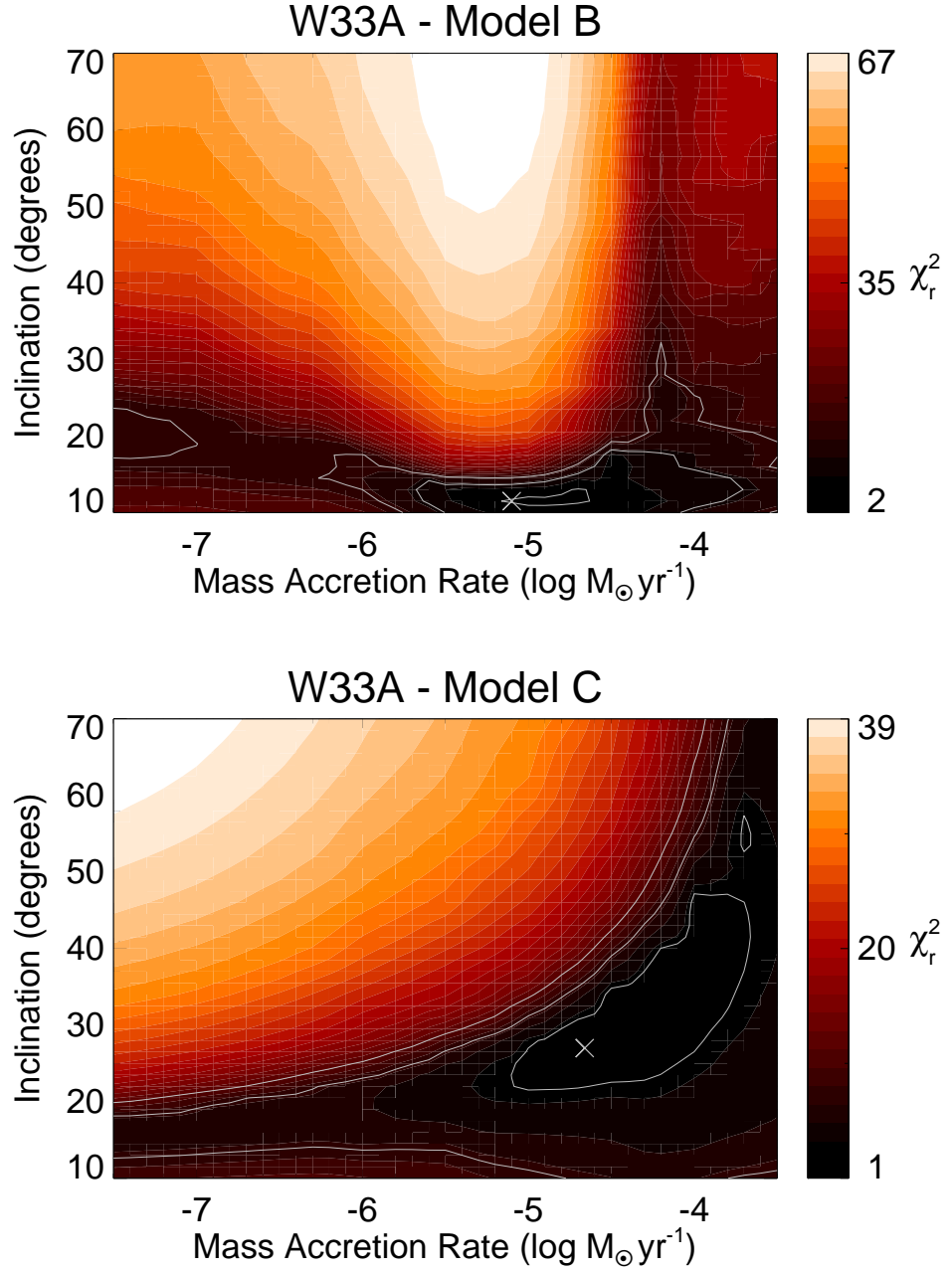


Figure 3.5: An exploration of the reduced chi squared values for fits to the spectrum of W33A using disc models B and C. The location of the minimum, $\chi_r^2(\text{min})$, corresponding to the values in Table 3.3, is denoted by a white cross, and contours show the levels of $\chi_r^2(\text{min})+1$, $+5$ and $+9$, respectively. In both cases, the intrinsic linewidth is set to the best fitting value as determined by the fitting routine.

model B are very sensitive to the inclination of the disc, and are confined to a very small range of low inclinations, while the fits are less sensitive to the mass accretion rate, where a range of values from $6 \times 10^{-6} - 3 \times 10^{-6} M_{\odot} \text{ yr}^{-1}$ are contained within the $\chi_r^2 + 1$ contour. Fits using model C allow higher inclinations to be reached, however these inclinations are still lower than the $40\text{--}70^\circ$ determined by de Wit *et al.* (2010).

Model C is more sensitive to high accretion rates, which allows higher temperatures in the disc to be reached. As can be seen, higher mass accretion rates are reported than in model B. The hotter disc means that the CO emission region is located further out in the disc, and therefore suffers from less rotational broadening. This is why model C reports a higher inclination. However, this is still too low to be consistent with de Wit *et al.* (2010).

The models of massive young stellar objects in Hosokawa & Omukai (2009) suggest that high accretion rates affect the state of the central protostar. In particular, they suggest the radius of the central protostar can increase to over 100 solar radii for certain stellar masses. If this were the case in W33A, the assessment of the stellar parameters based on the standard main sequence relationships would be inaccurate. For the mass of W33A, Hosokawa & Omukai (2009) suggests a radius of approximately $30 R_{\odot}$, which is five times greater than the radius we adopt. To test how this may affect the fitting of the bandhead, the χ_r^2 plots for W33A were recreated under the assumption that the central protostar was bloated to $30 R_{\odot}$, which are shown in Figure 3.6.

The fit to W33A using model B and a bloated central protostar shifts the χ_r^2 minimum to higher accretion rates, and increases the range of inclinations with

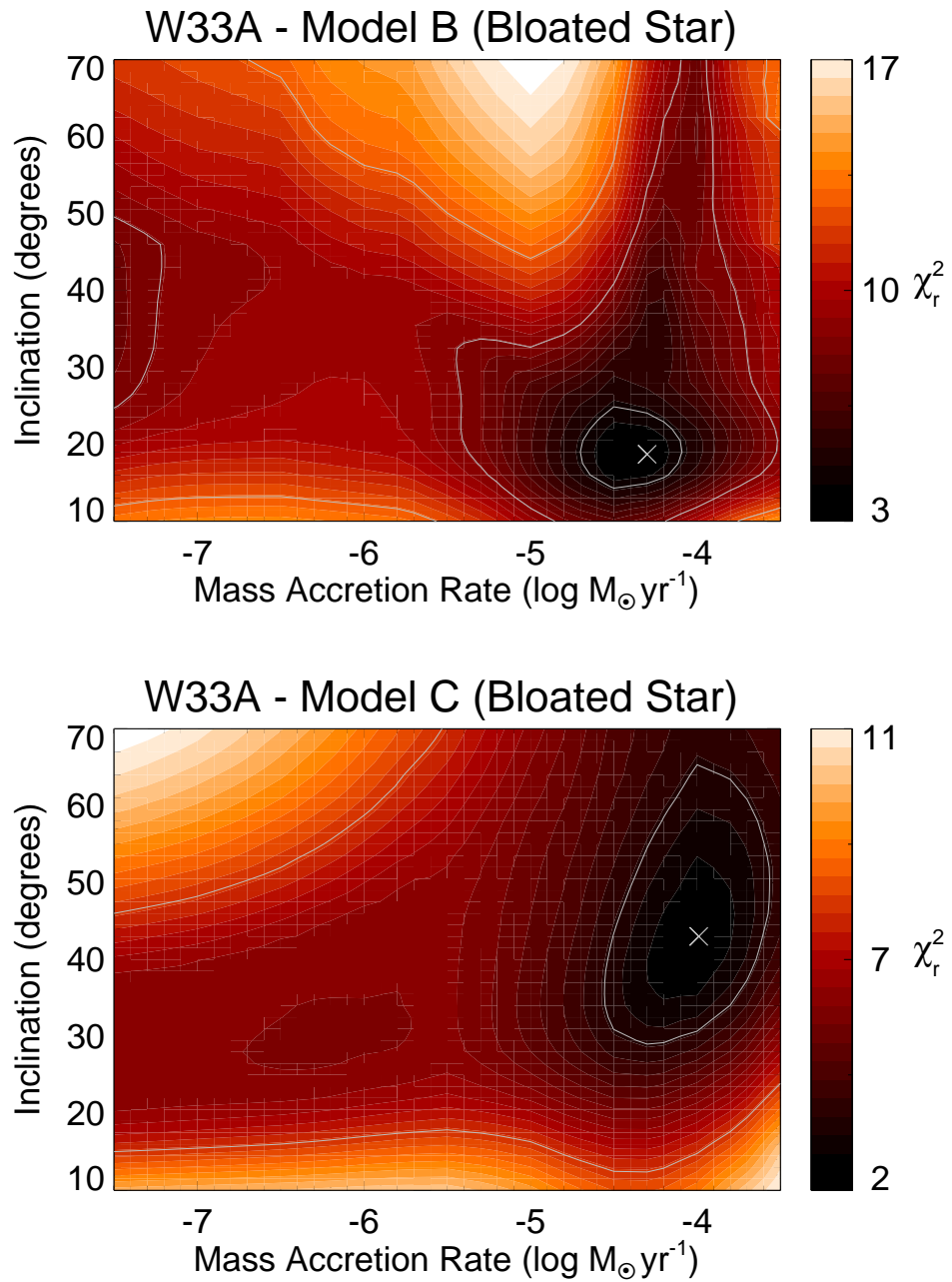


Figure 3.6: As Figure 3.5, but the stellar radius has been increased to five times the original radius - $30 R_{\odot}$.

small χ_r^2 values, but these inclinations are still below the range reported in de Wit *et al.* (2010). The fit using model C and a bloated central protostar produces minimum χ_r^2 values at similar mass accretion rates to model B, but the inclination is much higher, reaching comfortably into the required 40–70° range. However, while the overall location of the minimum has been shifted into an acceptable parameter space, the resulting minimum in χ_r^2 is still approximately 2.8, and visual inspection of the resulting best fitting spectrum confirmed that the fit was not a good match to the data.

In general, model A provides additional parameters in the temperature and density exponents, and their respective values at the inner edge of the CO emission region. This allows the model to effectively change the amount of material within the disc, and provides a better fit to these data. While models B & C are both based on physical descriptions of accretion discs, they may not contain all of the relevant details. For example, these models also assume emission from a flat disc, but in reality different disc geometries may need to be considered, such as flared discs, or discs with discrete vertical layers. For this reason, disc model A was chosen as a basis for the fitting routine for the other MYSOs, as it allows freedom to account for different emission geometries and is not reliant upon possibly inaccurate assumptions regarding the temperature and density structure of these discs.

Adopting disc model A, fits to all objects were obtained as described in Section 3.4.1. The errors were calculated by holding all but one parameters constant at their best fitting value, and varying the selected parameter until the difference in χ_r^2 was equal to one. For some parameters, the 1-sigma error values were beyond

the range of allowed parameters for our fitting routine. For all objects, fitting was attempted using data from both chips three and four of the detector. If a satisfactory fit was not obtained, the wavelength range of fitting was limited to only include data from chip three, and the fitting routine was repeated. Tests with individual objects showed that extrapolation of a fit using only the wavelength range of chip three, on to chip four, produced similar results to a fit involving both chips. This can be seen in several objects (for instance G296.2654–00.3901 and M8E-IR) where the extrapolated fit across chip four is consistent with the location of the rotational lines that were not included in the fitting range due to a poor signal-to-noise at these wavelengths.

3.5 Full sample results

The model is able to fit all objects with spectra that have sufficiently strong CO emission, found to be above approximately six times the rms noise in the pre-bandhead section of the spectrum. Eight MYSOs and the two lower mass YSOs are fitted across the full chip three and four wavelength range, and also use only chip three (or a portion of chip three) to fit the remaining 9 MYSOs. Three objects (G293.8947–00.7825, G332.0939–00.4206 and G339.6816–01.2058) were determined to have CO emission that was too weak, or a signal-to-noise ratio that was too low, to provide a reliable fit, but for completeness their spectra are included in Section 3.8. The two reclassified low mass YSO objects, G332.9457+02.3855 and G338.5459+02.1175, are excluded from the analysis here and discussed in Section 3.8.

Figure 3.7 presents the spectra and best fitting models using disc model A, to

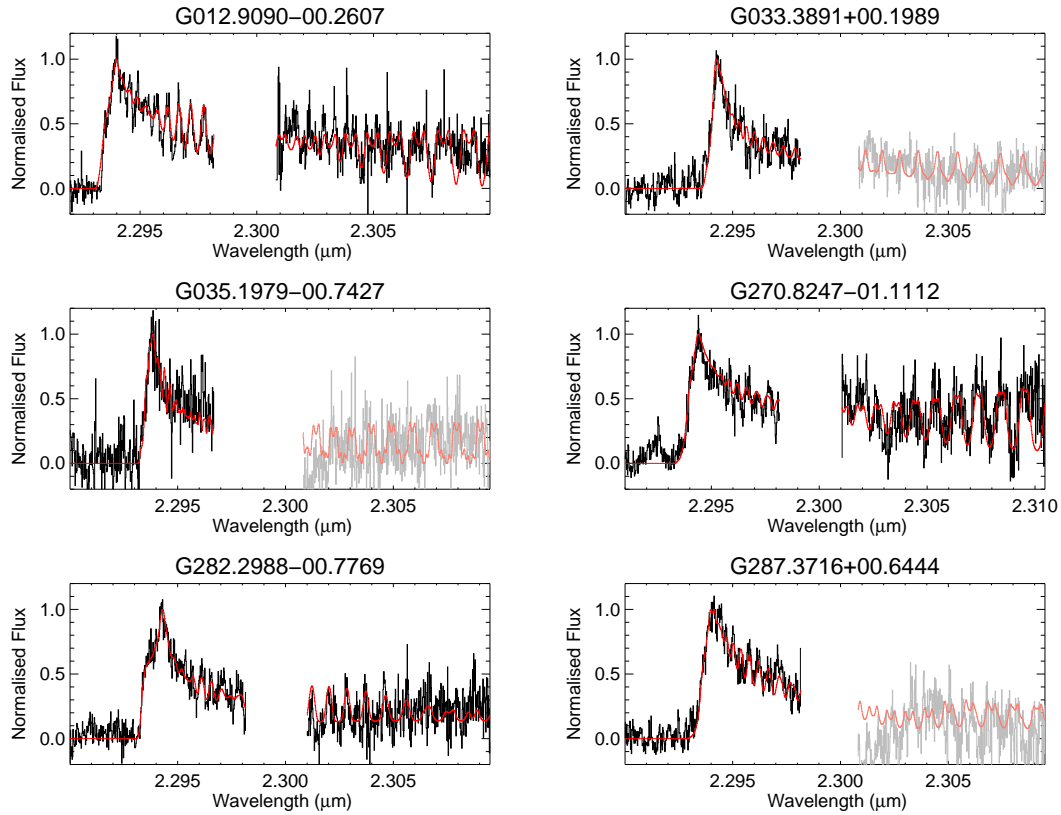


Figure 3.7: Spectra (black) and model fits (red) to the CO emission of the objects in the sample, using disc model A. Data that are greyed out are not included in the fitting procedure because of poor quality, but have been included for completeness.

each of the MYSOs with CO emission. Objects where only chip three has been used for the fitting routine are indicated with a greyed-out chip four region. Table 3.5 shows the best fitting model parameters for each of the objects, with associated 1-sigma errors. Errors marked with an asterisk should be considered lower limits, as the full 1-sigma error value was beyond our allowed parameter range.

In general, across the 7 objects whose inclinations have been constrained before, the best fitting parameters agree with the previous results, within error margins. Comments and comparisons on an object by object basis are presented in Section 3.7. The majority of objects have discs beginning within a few astronomical units

Table 3.4: Stellar parameters used for the model fitting. The stellar mass M_\star , radius R_\star and effective temperature T_{eff} are derived from observed bolometric luminosity in Table 3.1 using interpolation from the main sequence relationships described in Martins *et al.* (2005), unless otherwise stated.

Object	M_\star (M_\odot)	R_\star (R_\odot)	T_{eff} (K)
MYSOs			
G012.9090−00.2607	21.2	7.0	33500
G033.3891+00.1989	12.3	4.8	26500
G035.1979−00.7427	17.7	6.1	31200
G270.8247−01.1112	12.3	4.8	26500
G282.2988−00.7769	11.8	4.7	26100
G287.3716+00.6444	17.1	6.0	30800
G296.2654−00.3901	9.6	4.0	23600
G305.2017+00.2072	20.4	6.8	33100
G308.9176+00.1231	31.7	9.0	37400
G310.0135+00.3892	21.8	7.0	33800
G332.9868−00.4871	16.6	5.9	30400
G338.9377−00.4890	7.4	3.4	21400
G347.0775−00.3927	7.0	3.3	20900
IRAS 08576−4334	6.1 [◦]	3.0	19200
IRAS 16164−5046	34.9	9.8	38300
IRAS 17441−2910	56.9	14.3	41300
M8E-IR	13.5 [†]	5.1	27800
Non-MYSOs (see Section 3.8)			
G332.9457+02.3855 [§]	0.5	3.0	5000
G338.5459+02.1175 [§]	0.5	3.0	5000

◦: Determined from the position in the K versus J−K diagram of Bik *et al.* (2006), as in Wheelwright *et al.* (2010). †: Taken from Linz *et al.* (2009), which is based on the best fitting model from Robitaille *et al.* (2007). §: The stellar mass, radius and effective temperature of these objects is estimated from typical T Tauri star values (Covey *et al.*, 2011).

Table 3.5: Best fitting disc parameters to the CO spectra. The outer disc radius is defined at the point in the disc in which the temperature drops below 1000 K, so no error is presented.

Object	R_i (au)	R_o (au)	T_i (K)	N_i (cm^{-2})	p	q	i ($^\circ$)	$\Delta\nu$ (km s^{-1})	χ_r^2
MYSOs									
G012.9090−00.2607	$2.3^{+0.9*}_{-1.0}$	76	2300^{+50}_{-480}	$2.2^{+40}_{-*} \times 10^{21}$	$-0.25^{+0.25*}_{-4.75*}$	$-4.10^{+1.80}_{-0.90*}$	37^{+16}_{-11}	$21.0^{+9.0*}_{-16}$	1.4
G033.3891+00.1989	$2.1^{+0.1*}_{-1.0}$	3200	4600^{+400*}_{-1800}	$0.4^{+7}_{-*} \times 10^{21}$	$-0.06^{+0.06*}_{-4.94*}$	$-1.70^{+0.30}_{-3.30*}$	40^{+50*}_{-25}	$29.0^{+1.0*}_{-17}$	2.8
G035.1979−00.7427	$2.3^{+0.5*}_{-2.0}$	440	3100^{+10}_{-3100*}	$1.4^{+*}_{-*} \times 10^{23}$	$-0.20^{+0.20*}_{-4.80*}$	$-4.00^{+1.40}_{-1.00*}$	36^{+54*}_{-20}	$2.9^{+10}_{-2.9*}$	1.8
G270.8247−01.1112	$1.1^{+0.5*}_{-1.0}$	93	3600^{+10}_{-960}	$0.4^{+1.9}_{-0.4} \times 10^{22}$	$-0.32^{+0.10}_{-0.20}$	$-1.60^{+0.40}_{-0.70}$	89^{+1*}_{-40}	$18.9^{+21.1*}_{-13}$	2.8
G282.2988−00.7769	$1.7^{+0.5*}_{-0.6}$	9	4800^{+10}_{-1500}	$0.1^{+2.3}_{-*} \times 10^{21}$	$-0.97^{+0.60}_{-2.20}$	$-1.40^{+1.40*}_{-3.60*}$	80^{+10*}_{-30}	$16.3^{+13.7*}_{-16.3*}$	2.8
G287.3716+00.6444	$0.1^{+0.1}_{-0.1}$	3	4200^{+80}_{-720}	$9.1^{+*}_{-4.2} \times 10^{24}$	$-0.45^{+0.10}_{-0.10}$	$-0.88^{+0.88*}_{-0.10}$	17^{+4}_{-2}	$3.1^{+1.2}_{-0.6}$	7.1
G296.2654−00.3901	$1.7^{+0.2*}_{-1.0}$	530	3400^{+60}_{-1280}	$0.1^{+3.1}_{-0.0} \times 10^{23}$	$-0.20^{+0.20*}_{-0.40}$	$-2.20^{+0.90}_{-0.80}$	23^{+67*}_{-23*}	$28.0^{+2.0*}_{-22}$	1.3
G305.2017+00.2072	$0.6^{+0.3}_{-0.3}$	52	2930^{+20}_{-480}	$2.1^{+1.6}_{-1.7} \times 10^{21}$	$-0.27^{+0.10}_{-0.10}$	$-1.61^{0.20}_{-0.40}$	43^{+13}_{-8}	$14.5^{+15.5*}_{-8}$	4.7
G308.9176+00.1231	$0.7^{+1.6}_{-0.6}$	9	4430^{+30}_{-3200}	$4.8^{+*}_{-*} \times 10^{21}$	$-0.59^{+0.20}_{-4.80*}$	$-0.14^{+0.14*}_{-3.6*}$	67^{+23*}_{-38}	$12.6^{+17.4*}_{-12.6*}$	0.9
G310.0135+00.3892	$2.8^{+0.5*}_{-2.0}$	69	3760^{+100}_{-1400}	$3.8^{+*}_{-*} \times 10^{12}$	$-0.43^{+0.20}_{-4.57*}$	$-0.50^{+0.50*}_{-4.5*}$	67^{+23*}_{-41}	$25.5^{+4.5*}_{-25.5*}$	2.0
G332.9868−00.4871	$0.5^{+0.8}_{-0.3}$	7	4400^{+120}_{-1600}	$0.1^{+1.9}_{-*} \times 10^{21}$	$-0.59^{+0.20}_{-0.4}$	$-0.01^{+0.01*}_{-1.3}$	78^{+12*}_{-38}	$29.7^{+0.3*}_{-28}$	1.9
G338.9377−00.4890	$0.3^{+0.3}_{-0.2}$	1	4900^{+100*}_{-2200}	$0.4^{+2.1}_{-*} \times 10^{20}$	$-1.22^{+0.90}_{-3.78*}$	$-1.63^{+1.63*}_{-3.37*}$	89^{+1*}_{-45}	$29.9^{+0.1*}_{-29.9*}$	1.2
G347.0775−00.3927	$0.4^{+1.1*}_{-0.3}$	3	4600^{+10}_{-2000}	$0.3^{+4.7}_{-*} \times 10^{21}$	$-0.79^{+0.60}_{-4.21*}$	$-1.14^{+1.14*}_{-3.86*}$	84^{+6*}_{-61}	$26.5^{+3.5*}_{-26.5*}$	1.9
IRAS 08576−4334	$0.6^{+0.1}_{-0.1}$	7	4980^{+20*}_{-800}	$2.8^{+6.4}_{-6.4} \times 10^{21}$	$-0.71^{+0.05}_{-0.05}$	$-0.001^{+0.001*}_{-0.60}$	$65^{+4.1}_{-11}$	$15.7^{+2.4}_{-3}$	2.9
IRAS 16164−5046	$1.9^{+0.1}_{-0.1}$	5	4380^{+10}_{-1900}	$0.1^{+2.1}_{-*} \times 10^{22}$	$-1.45^{+0.90}_{-3.55*}$	$-1.37^{+1.37*}_{-3.63*}$	62^{+16}_{-12}	$11.9^{+18.1*}_{-8}$	1.7
IRAS 17441−2910	$6.0^{+0.6*}_{-0.1}$	13	3880^{+10}_{-400}	$3.8^{+0.2}_{-*} \times 10^{21}$	$-1.72^{+1.30}_{-0.10}$	$-1.00^{+1.00*}_{-4.00*}$	53^{+2}_{-16}	$3.7^{+0.6}_{-3.7*}$	0.6
M8E-IR [‡]	$1.5^{+0.9*}_{-0.4}$	54	2300^{+10}_{-320}	$0.2^{+10}_{-*} \times 10^{20}$	$-0.24^{+0.24*}_{-4.76*}$	$-2.16^{+1.1}_{-2.84*}$	14^{+10}_{-14*}	49^{+11*}_{-13}	2.1
Non-MYSOs (see Section 3.8)									
G332.9457+02.3855	$0.7^{+0.7*}_{-0.6}$	4	3240^{+10}_{-880}	$2.5^{+5.3}_{-*} \times 10^{20}$	$-0.73^{+0.73*}_{-4.27*}$	$-2.60^{+2.60*}_{-2.40*}$	66^{+24*}_{-66*}	$29.8^{+0.2*}_{-29.8*}$	2.7
G338.5459+02.1175	$1.2^{+0.2*}_{-0.4}$	61	5000^{+0*}_{-1000}	$1.5^{+6.0}_{-0.9} \times 10^{22}$	$-0.36^{+0.00}_{-0.20}$	$-3.77^{+1.40}_{-1.23*}$	87^{+3*}_{-61}	$28.4^{+1.6*}_{-11}$	3.9

*: The value of χ_r^2 did not change by one over the allowed parameter range. ‡: The wavelengths fitted and ranges of allowed fit parameters were altered to obtain a good fit, see text for details.

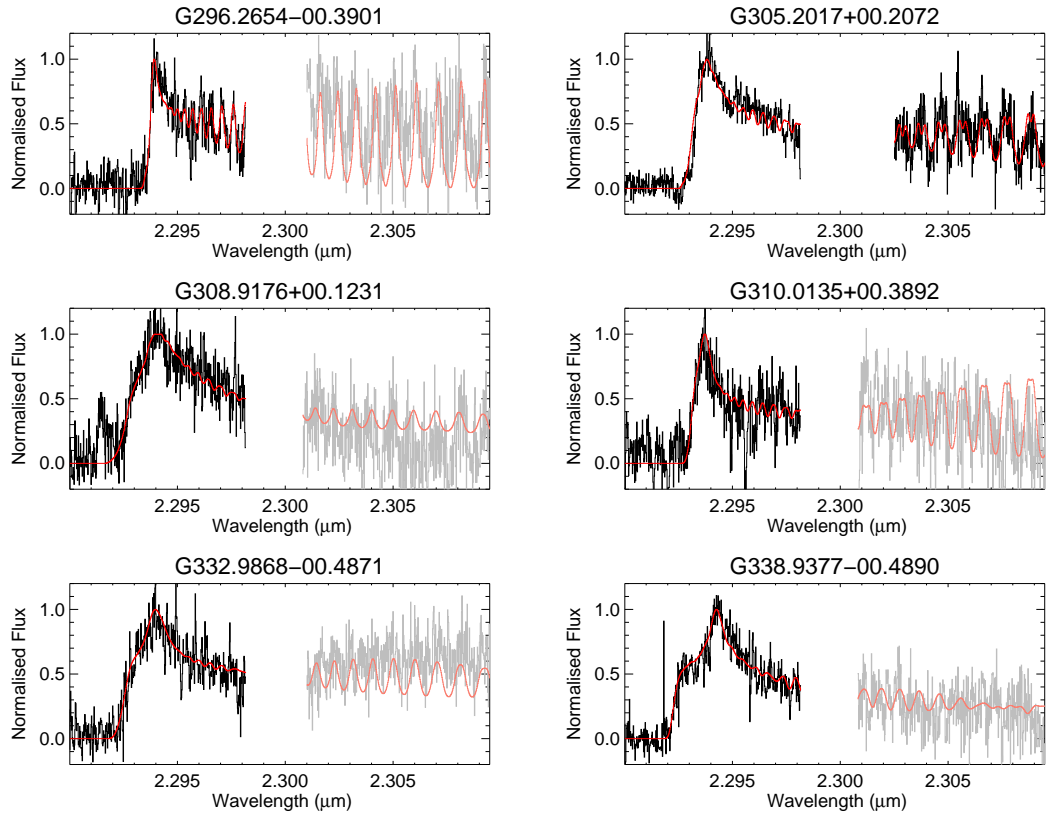


Figure 3.7: Continued.

of the stellar surface, and inner disc temperatures close to the dissociation temperature of CO (5000 K). The distribution of the inner surface densities of the disc has a geometric average of $\bar{N}_i = 5.5 \pm 8 \times 10^{20} \text{ cm}^{-2}$. It should be noted that even though CO should be dissociated by stellar UV flux at these small distances, it is found as in Bik & Thi (2004) and Wheelwright *et al.* (2010) that the density is sufficient for self-shielding to occur ($N > 10^{15} \text{ cm}^{-2}$, van Dishoeck & Black 1988).

Figure 3.8 shows the distribution of the best fitting inclinations and the temperature and density exponents of the MYSOs. While our inclinations are consistent with most previously published data for objects, IRAS 08576–4334 is not, and this is discussed in detail in Section 3.7. The distribution of the best fitting inclinations

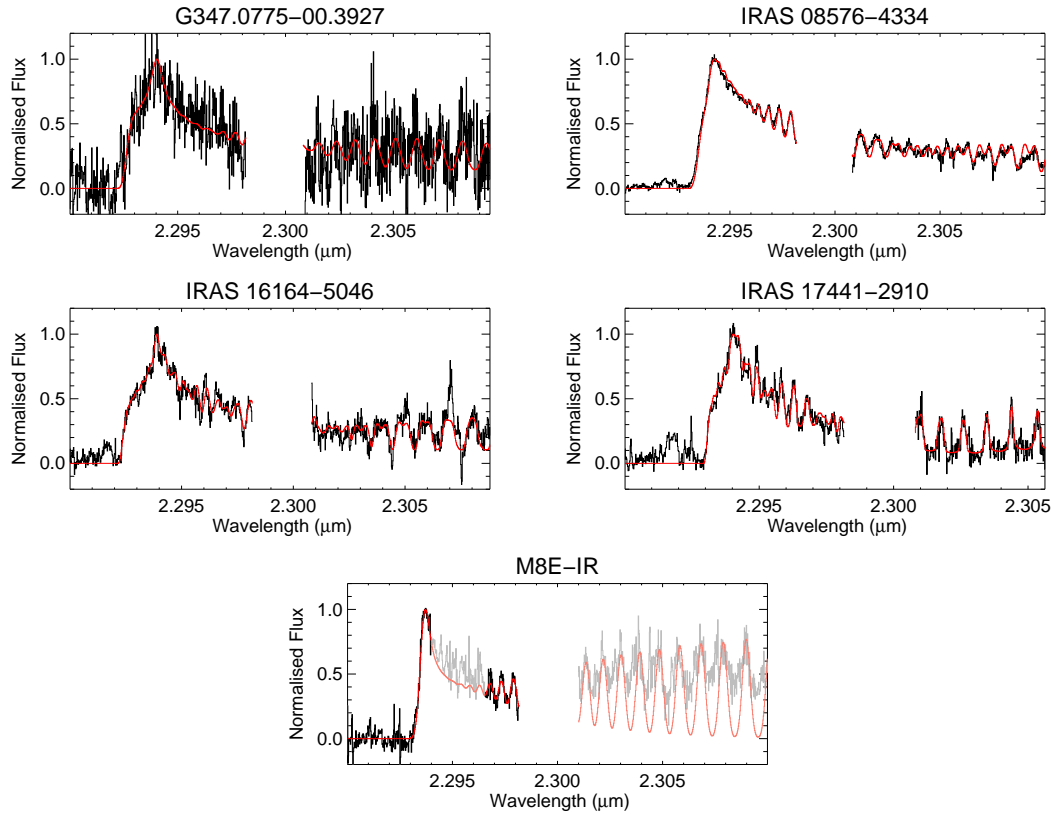


Figure 3.7: Continued.

is essentially consistent with the inclinations being random ($\bar{i} = 60^\circ$), as the mean inclination value is $\bar{i} = 55 \pm 25^\circ$. The temperature gradients are skewed toward higher values, but have a mean of $\bar{p} = -0.6 \pm 0.5$, close to the -0.75 suggested for a flat accretion disc. We note that two objects show well constrained temperature gradients of -0.43 , which are consistent with flared, irradiated discs (Chiang & Goldreich, 1997). The surface density gradients are more evenly spread across the parameter space, with a mean of $\bar{q} = -1.5 \pm 1.2$. This is consistent with the surface density gradient for a flat accretion disc, although it is associated with a large error. The average intrinsic linewidth of the fits is $\overline{\Delta\nu} = 20 \pm 12 \text{ km s}^{-1}$. Apart from two objects (G287.3716+00.6444 and IRAS 17441-2910) the linewidths are

approximately ten times the thermal linewidths expected for CO between 1000–5000 K, suggesting that the emitting material is dominated by macro-turbulent motions or infall.

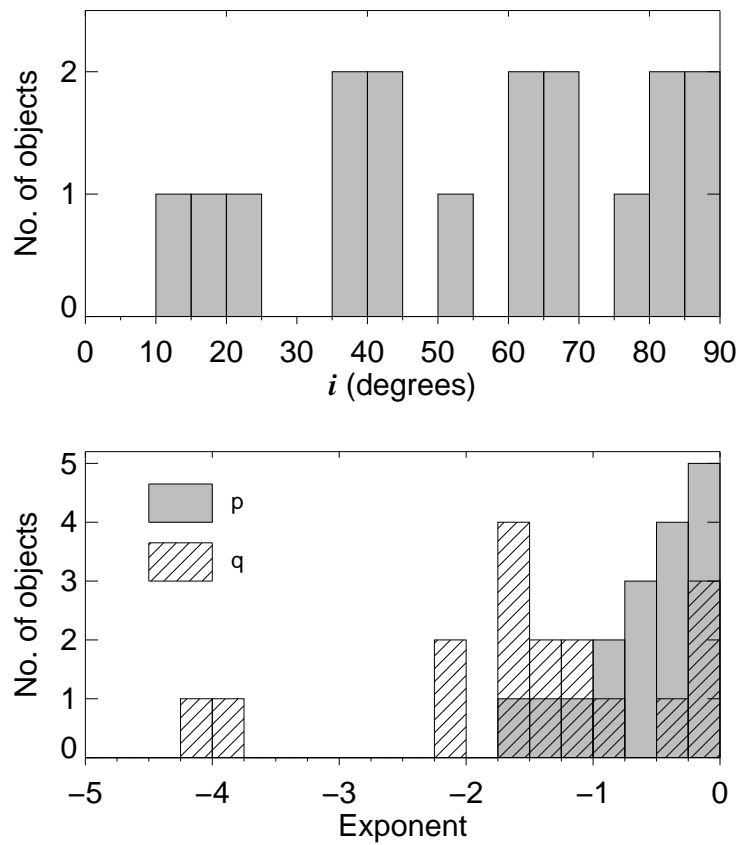


Figure 3.8: Distributions of inclinations (top), and temperature and surface density exponents (p and q , respectively, bottom) determined from the fits to the 17 MYSOs with detected CO bandhead emission.

3.6 Discussion

3.6.1 Disc sizes - the location of the emission

A range of disc sizes are found from the results. However, in the majority of cases, the inner edge of the CO emission region is within a few au. The outer edge of the emission region varies much more, giving rise to three very large discs. However, the objects with very large discs have temperature exponents that are poorly constrained. This allows very shallow gradients (as seen in Figure 3.8), which in turn produce large outer disc radii, because this is defined as where the excitation temperature drops below 1000 K. Thus, these large disc sizes are likely not physical and much smaller discs can be produced with an exponent that is still within the uncertainty in the best fitting value.

To compare the location of the CO emission to the circumstellar disc as a whole, one can calculate the dust sublimation radius, R_S , in au for each object:

$$R_S = 1.1\sqrt{Q_R} \left(\frac{L_\star}{1000 L_\odot} \right)^{0.5} \left(\frac{T_S}{1500 \text{ K}} \right)^{-2}, \quad (3.15)$$

where Q_R is the ratio of absorption efficiencies of the dust, and T_S is the temperature at which the dust sublimates (Monnier & Millan-Gabet, 2002). We take $Q_R = 1$ and $T_S = 1500$ K. This is then compared to both the inner and outer radii of the CO emission disc from our model fits. Figure 3.9 shows histograms of the ratios between these quantities.

As expected, it is found that the majority of objects, approximately 75 per cent, have CO discs whose inner extent is less than the dust sublimation radius. Approximately 30 per cent have CO discs with an outer extent below the dust

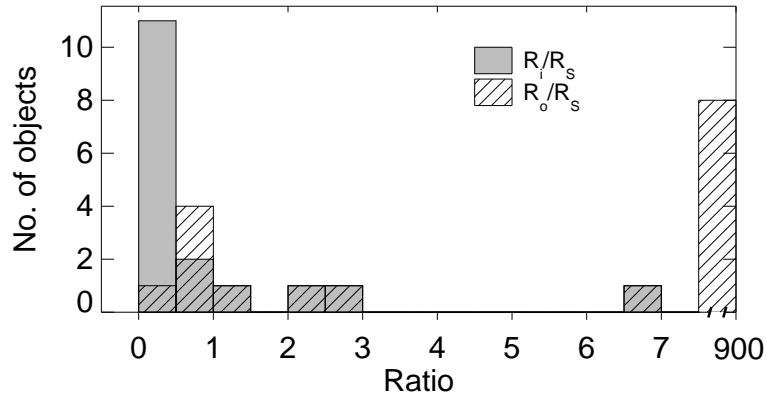


Figure 3.9: Ratio of inner and outer CO disc radii, R_i , R_o , compared to the dust sublimation radius R_S for each object. The majority of objects have inner radius well below the dust sublimation radius, and in some cases the entire CO disc is inside the sublimation radius. Most of the discs are within a few dust sublimation radii. Note that the final bin in the histogram is uneven and extends from 7.5–900.

sublimation radius. However this percentage is increased if the artificially large discs discussed earlier are excluded. Concerning the remaining objects, there are several cases where the inner and/or outer disc radii are only a few times larger than the dust sublimation radius. The treatment of the sublimation is simplistic. Factors such as rapid accretion rates, back-warming and non-homogeneous dust grain sizes may increase the dust sublimation radius to several times the value that is predicted. Therefore, the best fitting disc properties appear consistent with physical expectations. Consequently, it is suggested that, in general, the best fitting discs can be associated with gaseous accretion discs that are close to the central star. As this is the largest sample of MYSOs with CO bandhead emission studied to date, this provides strong evidence for the existence of small scale accretion discs around these objects.

3.6.2 Determining mass accretion rates

As discussed previously, the use of a physical disc model that directly includes the relevant physics needed to determine a mass accretion rate is attractive. However, as these models did not fit our data well, we were unable to find accretion rates directly from the fits, and thus we obtained analytic descriptions of how the temperature and density vary as a function of radius within the discs.

Therefore, comparing the radial profiles of the temperature and density from our fits using the analytic model (model A) to the radial profiles predicted by model C for different mass accretion rates ($\dot{M} = 10^{-3.5}-10^{-7.5} M_{\odot} \text{ yr}^{-1}$) was investigated. It was postulated that if these radial profiles agree for both the temperature and the density, then it would be possible to assign a mass accretion rate to each object based on this comparison. However, it was found that, for many of the objects, the mass accretion rates obtained from the temperature profile and the density profile differed by orders of magnitude. Also, several accretion rates were difficult to determine due to very different gradients between the fits using model A and the various model C radial profiles (which were fixed), and the values obtained are therefore unreliable. On average, we found that the mass accretion rate from the temperature gradients suggested $\dot{M} > 10^{-4} M_{\odot} \text{ yr}^{-1}$ while the surface density distribution suggested $\dot{M} < 10^{-7} M_{\odot} \text{ yr}^{-1}$.

It is concluded that our model fits cannot currently be used to determine the mass accretion rates of MYSOs. While this has been performed in previous studies of lower mass young stellar objects (Carr, 1989; Chandler *et al.*, 1995), the higher resolution of our data demonstrates there are many rotational lines that cannot be fitted using these simple disc models. These models may be inadequate

in accurately representing the physical situation that gives rise to CO bandhead emission from discs with high accretion rates. Also, the study of only a single bandhead may not offer sufficient information to reliably determine the physical properties of discs and thus cannot accurately constrain mass accretion rates in this way.

3.6.3 Are these typical MYSOs?

In this section we consider whether the MYSOs with CO emission differ from those without. An important question since the detection rate of CO emission in the spectra of MYSOs is approximately 25 per cent.

MYSOs are typically red objects with a featureless continuum in the optical and NIR, so we cannot accurately constrain their stellar properties such as effective temperature and radius. Therefore, we investigate whether the parameters of the best fitting models display a pattern which may explain why only some MYSOs exhibit this emission. In particular, it is conceivable that for CO emission to be observed, the inclination of the disc is required to be close to face on. However, the inclinations of the objects are spread relatively evenly between 0 and 90°, with a slight preference for higher inclinations, suggesting this is not the case. In addition, we note that the average bolometric luminosity of our sample of objects with CO emission is $5 \times 10^4 L_{\odot}$, which is typical of objects within the RMS survey. Therefore, we conclude that the properties of the MYSOs that exhibit CO bandhead emission do not indicate what specific geometry and/or conditions are required for the presence of this emission.

Consequently, it is not certain why the presence of CO bandhead emission is

not ubiquitous in the spectra of MYSOs. It is possible that the objects with CO emission represent a different evolutionary stage of MYSOs than those without. It is difficult to test this hypothesis. As an initial test, the infrared colours of the observed MYSOs were investigated, which are likely affected by key factors such as circumstellar geometries on astronomical unit scales, inclination and envelope mass/infall rate. To determine whether the MYSOs with CO bandhead emission appear representative of MYSOs in general or are a specific subset of MYSOs, their NIR colours were compared with those of approximately 70 objects from the RMS database, which are shown in the upper panel of Figure 3.10. To ensure a valid comparison with our objects, the control sample was selected to have a high luminosity ($L > 10^4 L_{\odot}$) and be bright in the K -band ($K < 10$ magnitudes). The $J - K$ and $H - K$ colours of the two samples were compared using the Kolmogorov–Smirnov (KS) test and it was found that the hypothesis that the NIR colours of the MYSOs with CO bandhead emission are drawn from the distribution of NIR colours exhibited by the RMS population cannot be discounted with any significance. The objects observed to have CO bandhead emission are generally bright in the K -band. However, this is a selection effect and does not imply that only objects with such emission are intrinsically brighter in the K -band.

Also examined were the mid-infrared (MIR) colours of the sample. Specifically, the *MSX* ($F_{21\mu\text{m}} - F_{8\mu\text{m}}$), ($F_{21\mu\text{m}} - F_{12\mu\text{m}}$) and ($F_{21\mu\text{m}} - F_{14\mu\text{m}}$) colours of the objects with CO bandhead emission were compared to the RMS population mentioned earlier. The lower panel of Figure 3.10 shows the cumulative distribution of the ($F_{21\mu\text{m}} - F_{8\mu\text{m}}$) colours. Using the KS test, it was found that the hypothesis that the MIR colours of the objects with CO emission are drawn from the total RMS distribution of MIR colours cannot be discounted with any significance. Therefore,

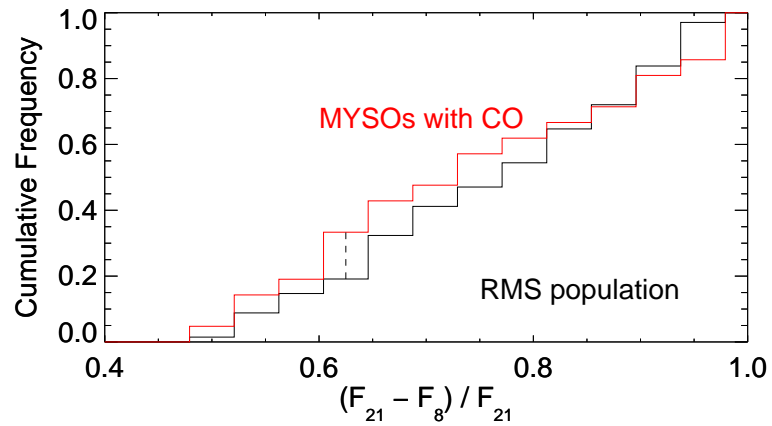
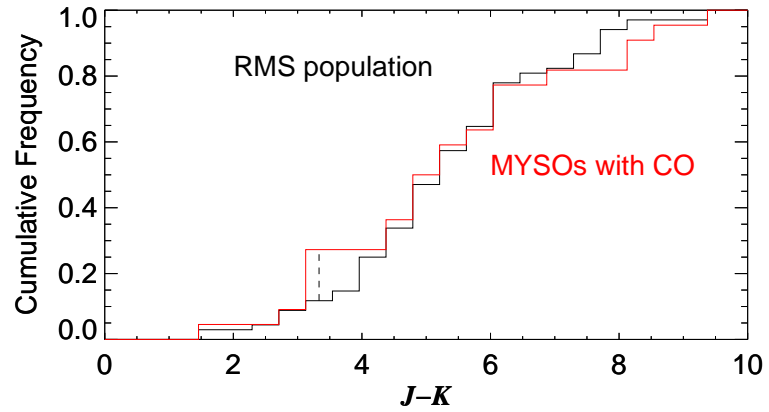


Figure 3.10: Cumulative frequency of the NIR $J - K$ and normalised MIR $(F_{21\mu\text{m}} - F_{8\mu\text{m}})$ colours of the MYSOs with CO emission and the RMS population. The dashed vertical lines indicate the largest deviation between the distributions. Similar distributions were found for the $H - K$, $(F_{21\mu\text{m}} - F_{12\mu\text{m}})$ and $(F_{21\mu\text{m}} - F_{14\mu\text{m}})$ colours.

the objects with and without CO emission appear no different in terms of both their NIR and MIR colours, suggesting these objects are representative of the RMS population as a whole.

It is therefore unclear from this analysis why only some MYSOs possess CO emission. It has been predicted that models of circumstellar discs of MYSOs can be unstable (Krumholz *et al.*, 2007) and that the accretion rate in these discs is not constant (Kuiper *et al.*, 2011). Unstable discs may disrupt the circumstellar material and lead to physical conditions in which CO ro-vibrational emission no longer occurs. If the disc accretion rate is high, this will increase the mid-plane temperature of the disc and move the CO emission region further away from the central protostar, possibly into the surrounding envelope, which may cause the emission to cease. However, without a method to determine the accretion rate of these objects, this hypothesis is difficult to test.

3.7 An object by object comparison with previous studies

This section discusses and compares, on an object by object basis, the findings with that of previous studies on a selection of our sample where data was available.

G033.3891+00.1989

The work of Wheelwright *et al.* (2010) fitted the CO bandhead emission of this object using fixed power law relations for the disc. They found a disc from 0.24–2.0 au, at an inclination of 18°, with an intrinsic linewidth of 20 km s⁻¹ (which was

not well constrained) and a CO number density of $9 \times 10^{21} \text{ cm}^{-2}$. The inclination, number density and linewidth agree with our best fitting model within error ranges, but the size of our disc is much larger, due to a shallow temperature gradient.

G035.1979–00.742

The object G035.1979–00.74 has been observed using ALMA by Sánchez-Monge *et al.* (2013). Images of the CH₃CN and HC₃N emission were obtained, probing scales up to 2500 au from the central object. A best fit to the data was found with a disc model at an inclination of 71°. Our derived inclination of 36° is not well constrained due to the poor quality of the spectrum across the fourth detector chip, but is consistent with their findings.

G287.3716–00.6444

Wheelwright *et al.* (2010) do not find a satisfactory fit to the CO bandhead of this object assuming a circumstellar disc (with fixed temperature and density profiles), nor an isothermal non-rotating body of CO. They discuss other possible origins for the emission, including a disc with an outer bulge, a dense neutral wind, a shock, or a disc in which the receding side is much brighter than the approaching side. We note that our temperature exponent is close to -0.43 , which would be consistent with a flared, irradiated disc (Chiang & Goldreich, 1997) which may act in the same way as a disc with an outer bulge.

G308.9176+00.1231 (AFGL 4176)

The work of Wheelwright *et al.* (2010) finds a disc from 1–8 au at an inclination of 30°. The size of the disc agrees well with our results, but we find a higher

inclination of 67° , with 30° at the lower limit of our error range. Our linewidth of 12.6 km s^{-1} agrees with their value of 14 km s^{-1} , however our inner density is one order of magnitude lower. Boley *et al.* (2012) find their observations described well by a large circumstellar disc at an inclination of 60° , agreeing with our best fitting model, and consistent with the prominent blue shoulder in our data.

G310.0135+00.3892

G310.0135+00.3892 (IRAS 13481–6124) has previously been observed using the VLTI and AMBER in the K -band by Kraus *et al.* (2010) who report an elongated structure that is consistent with a disc viewed at a moderate inclination of approximately 45° . Wheelwright *et al.* (2012a) fitted the SED using a model with an inclination of 32° . Our relatively high inclination of 67° is not well constrained, due to the poor quality of the data, but agrees with these values within the error range.

Kraus *et al.* (2010) find a temperature gradient of $p \sim -0.4$, which they suggest is consistent with a flared, irradiated disc based on the work of Chiang & Goldreich (1997). We find a temperature gradient of $p = -0.43$, which is consistent with this hypothesis. Our inner disc temperature of 3800 K is warmer than the value of approximately 1500–2000 K assumed in Kraus *et al.* (2010), but is consistent as we are concerned with a gaseous disc as opposed to a dust disc. We find a smaller inner radius (2.8 au) for our disc than their study (9.5 au).

G332.9868–00.4871

Wheelwright *et al.* (2012a) determine an inclination of 15° to G332.9868–00.4871, which is far from our reported value of 78° even considering the large error. How-

ever, we note that our data have a relatively low signal-to-noise ratio, and no rotational lines in the fourth chip can be observed, thus our fit is likely not the best fit for the object.

G347.0775–00.3927

Wheelwright *et al.* (2010) find a similar sized disc to our best fitting model, from 0.5–4 au but with a lower inclination of 30° . However, our inclination of 84° is not well defined, and this does lie within our lower error bound. It should also be noted that the bolometric luminosity from the RMS database used in their study has since been revised to a lower value, which we use here.

IRAS 08576–4334

IRAS 08576–4334 has been extensively studied in recent years. Bik & Thi (2004) model the CO emission using an isothermal disc from 0.2–3.6 au, with an inclination angle of 27° , a CO number density of $3.9 \times 10^{21} \text{ cm}^{-2}$ and an excitation temperature of 1600 K. Wheelwright *et al.* (2010) used a similar method, but utilise a disc model with fixed power laws, and show the data to be well fit with a 0.09–0.78 au disc, at an inclination of 18° , with a CO number density of $7.9 \times 10^{21} \text{ cm}^{-2}$ and an intrinsic linewidth of 20 km s^{-1} .

Ellerbroek *et al.* (2011) find double peaked He I and Fe I emission lines, with a separation of $60\text{--}100 \text{ km s}^{-1}$, which they conclude must originate from a circumstellar disc. They suggest IRAS 08576–4334 is likely an intermediate mass YSO with a mass accretion rate of $10^{-6}\text{--}10^{-5} M_\odot \text{ yr}^{-1}$, obtained from the determination of the outflow mass loss rate.

In contrast to Bik & Thi (2004) and Wheelwright *et al.* (2010), we find our observations are best fitted with larger disc from 0.6–6.5 au, at an inclination of 65°. We note that data of Wheelwright *et al.* (2010) does not have sufficient wavelength range to observe double-peaked emission lines beyond 2.297 μm , and that the lower resolution of the Bik & Thi (2004) data may mask the presence of these features, especially as they are not well defined and asymmetric in our data. Our best fitting model possesses a double peak width of approximately 50 km s^{-1} , similar to that of the He I and metal emission lines in Ellerbroek *et al.* (2011).

We note that the rotationally broadened lines from 2.306–2.309 μm show asymmetry, with a depletion on the blue side. These transitions likely correspond to the cooler material further out in the disc, and as such may be evidence for asymmetry in the disc, which cannot be fitted with our axisymmetric disc model.

IRAS 16164–5046

Bik & Thi (2004) model the CO emission of IRAS 16164–5046 using an isothermal disc from 3.1–3.2 au (with large errors) at an inclination of 30°, with an excitation temperature of 4480 K and a number density of $4 \times 10^{20} \text{cm}^{-2}$. The extent of the disc is consistent with our results within errors, however we find a best fit that is closer to the central star, which would account for our larger inner number density. Our disc inclination of 53° is higher.

Bik *et al.* (2006) find CO emission and Pfund series emission with a width comparable to that of the CO emission, suggesting a common kinematic origin. However, due to the different conditions required for both emission, they suggest the CO emission comes from the midplane of a disc, while the Pfund lines comes from the ionised upper layers. They also note CO absorption from 2.33–2.35 μm ,

indicative of cold, foreground molecular gas.

M8E-IR

Wheelwright *et al.* (2010) were able to fit the emission of this object with a disc from 0.3–2.6 au at an inclination of 16° , with an inner number density of $1 \times 10^{23} \text{ cm}^{-2}$ and a linewidth of 7 km s^{-1} . Linz *et al.* (2009) find an inclination of 18.5° and a density exponent of $q = -2.05$ using $\alpha = 0.013$.

Our fits to M8E-IR did not satisfactorily converge using many starting positions across the initial parameter space. The spectrum was highly reddened, and the fit suffered from several minima with similar χ_r^2 values. The only change applied between these fits was the level of continuum subtraction applied. There were two issues with the data. Firstly, the level of the chip 4 flux seemed too high to be reproduced by the model, meaning that even solutions that reproduced the rotational line structure were assigned poor χ_r^2 values. Secondly, the model was unable to reproduce the relatively narrow structures on the red side of the bandhead edge, which may be noise. Because these features were across a larger range of wavelength than the three broader lines at the edge of chip 3, the fitting routine assigned them a higher weight which resulted in poor fits to the bandhead slope and the broader lines.

To address this, we restricted the range of fitting to exclude this region (as can be seen in Figure 3.7), and increased the allowed upper linewidth to 60 km s^{-1} , which produced a better fit to the data, and produced similar best fitting parameters similar to those in Linz *et al.* (2009).

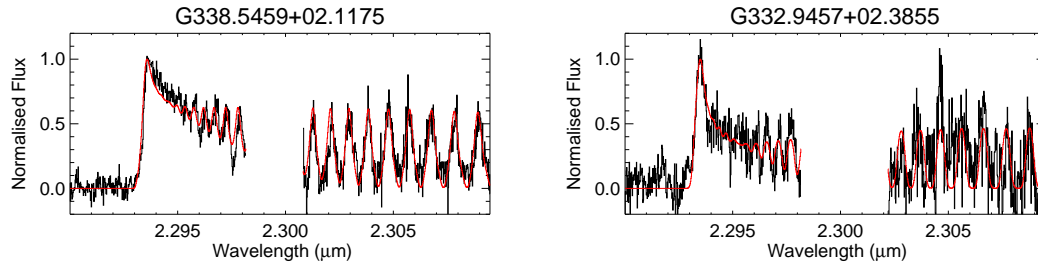


Figure 3.11: Objects that were later confirmed to be non-MYSO sources, but possess strong CO emission and were fitted with our disc model.

3.8 Lower mass YSOs and objects that were not fitted

The objects G332.9457+02.3855 and G338.5459+02.1175 were originally thought to be MYSOs at the time of observing, but subsequent determination of their bolometric luminosity has shown the objects too faint for this to be the case, and they are likely lower mass young stellar objects. We could not base our estimation of their stellar parameters on the main sequence relationships, so we have estimated their stellar parameters at the values shown in Table 3.5, which lie in the range of typical T Tauri star values. Changes to these parameters within these ranges had little effect on the final fits. The fits are presented in Figure 3.11.

Magnetically channelled accretion funnels have been suggested as a possible source for CO bandhead emission in T Tauri stars (Martin, 1997). We obtain good fits to the data of two young stellar objects using a simple disc model. The sizes of the discs are beyond the typical co-rotation radii for these objects. In addition, the intrinsic linewidths of both objects are similar to those of the massive YSOs. This suggests that the emission originates from circumstellar discs regardless of the mass of the central YSO, and not from accretion funnels.

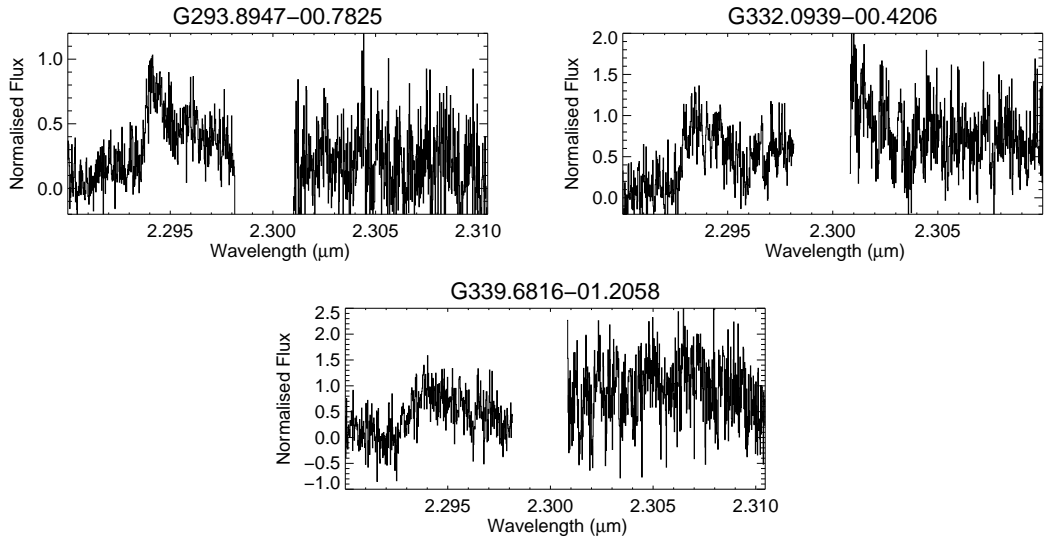


Figure 3.12: Objects that possessed CO emission that was too weak for an accurate fit to be obtained.

Finally, we note that three objects in the sample had CO emission that was too weak, or a signal-to-noise ratio that was too low for an accurate fit to be obtained. For completeness, we include their spectra in Figure 3.12.

3.9 Conclusions

This chapter has presented the near-infrared spectra of 20 massive young stellar objects that possess CO first overtone bandhead emission, the largest sample studied in this way to date. The spectra of these objects are fit with a model of emission originating in a circumstellar disc in Keplerian rotation. Three approaches to describing the properties of such circumstellar discs are investigated, and it is found that the spectra were best fit by using an analytic approach to describe the temperature and density within the disc. The main findings are:

1. All spectra are well fit by a model of a Keplerian rotation disc.

2. The best fitting disc parameters are consistent with previously published information. The inclinations are spread across a wide range of angles. The best fitting temperature and density exponents are, on average, consistent with flat circumstellar discs (subject to some scatter), a handful of objects have exponents consistent with flared, irradiated discs.
3. Essentially all the best fitting discs are located close to the dust sublimation radius, which is consistent with the existence of small scale gaseous accretion discs around these objects.

It is found that the mass accretion rates of the objects are not easily determined from examination of the disc structure as traced by a single CO bandhead. The analysis of further bandheads may allow these accretion rates to be determined.

The physical processes occurring during massive star formation are still not well understood. It is thought accretion proceeds through circumstellar discs at high rates, which are believed to affect the state of the central protostar (Hosokawa & Omukai, 2009; Hosokawa *et al.*, 2010). Furthermore, recent simulations indicate that high accretion rates result in massive discs and that gravitational torques in such self-gravitating discs provide a mechanism to transport angular momentum outwards (Kuiper *et al.*, 2011). Therefore, it is becoming apparent that accretion discs play a central role in the formation of massive stars. However, it is difficult to confirm this observationally. In most cases, the large distances to MYSOs, and their embedded nature, prevent detections of astronomical unit scale circumstellar discs (the exception being IRAS 13481, see Kraus *et al.*, 2010). In some cases, high infall rates have been detected towards massive star forming regions (see e.g. Beuther *et al.*, 2012; Herpin *et al.*, 2012; Qiu *et al.*, 2012; Wyrowski *et al.*, 2012).

However, these observations probe scales of approximately 1000 au and larger. Therefore, it is difficult to establish that this material will be accreted by a single object. Consequently, our observational overview of massive star formation is still incomplete.

With this in mind, it is noted that this sample constitutes the largest sample of MYSOs with CO bandhead emission studied to date (several times that of Wheelwright *et al.*, 2010). Therefore, by confronting the observations with a kinematic model, an extensive investigation can be conducted into the circumstellar environment of these objects. It is demonstrated that all the observed bandhead profiles can be successfully fitted with a model of a circumstellar disc in Keplerian rotation. In addition, it is shown that essentially all these models can be associated with gaseous discs interior to the dust sublimation radii of these objects. Finally, it is demonstrated that the objects in question appear no different to the ensemble of objects in the RMS catalogue, the largest most complete catalogue of MYSOs to date. Therefore, the fact that the CO bandhead emission of all the objects observed can be fitted with a disc model supports the scenario in which all MYSOs are surrounded by small scale (< 100 au) accretion discs. The objects observed constitute a large sample of circumstellar discs around MYSOs and provide promising targets for future observations and inspiration for detailed modelling of the accretion environment of such objects.

Chapter 4

Determining accretion rates in Herbig Ae/Be stars

4.1 Introduction

Pre-main sequence Herbig Ae and Be (HAeBe) stars lie in the mass range between T Tauri stars ($M < 2M_{\odot}$) and massive young stellar objects ($M > 8\text{--}10M_{\odot}$). Across this mass range, there is evidence for a change in the mechanism that transfers material from the cloud and disc on to the central protostar. The mechanism is thought to switch from T Tauri-like magnetospheric accretion (Bouvier *et al.*, 2007), to some other phenomenon. The interiors of HAeBes are thought to be mostly radiative (Hubrig *et al.*, 2009), and therefore they lack the interior convection needed to power a strong magnetic field that would be required for such magnetospheric accretion. Herbig Ae stars may possess sub-atmospheric convection zones which can power magnetic fields (Mottram *et al.*, 2007), but the situation for the higher mass Herbig Be stars is not known.

Thus, the study of HAeBes offers a unique insight into the formation mechanisms of high mass stars. The rate that material is transferred from the disc to the star (the mass accretion rate, \dot{M}) is an important parameter that determines the structure and dynamics of circumstellar discs (D'Alessio *et al.*, 1999, 2001), and varies with stellar age. Models of massive stars have also shown that the mass accretion rate affects the state of the central protostar (Hosokawa & Omukai, 2009). Therefore, it is important to understand how the mass accretion rate may change across this mass range.

Previously, methods to study accretion rates in young stars have involved examining either infrared excess continuum emission (caused by viscous dissipation in a circumstellar disc), or ultraviolet (UV) continuum excess (emitted by an accretion shock where disc material impacts on to the central protostar). Infrared excess is often contaminated with reprocessed stellar radiation, and measurements of UV continuum excess are only possible for stars with low extinction. Therefore, other, more observationally accessible tracers of accretion have been investigated.

In the near infrared, the $n = 7-4$ transition of atomic hydrogen (Br γ) occurs at $\lambda = 2.16 \mu\text{m}$. It is therefore ideally suited for use as a probe of embedded objects that are extinguished, such as HAeBes, because these NIR wavelengths are less scattered by the surrounding circumstellar material. Previous studies have shown that Br γ is a reliable probe of the accretion luminosity of young stellar objects. Muzerolle *et al.* (1998) found that the Br γ line luminosity in a sample of low mass ($0.2-0.8 M_{\odot}$) T Tauri stars was tightly correlated with the accretion luminosity as measured from blue continuum excess. Calvet *et al.* (2004) extended this investigation to YSOs with masses up to $4 M_{\odot}$, and find good agreement with

the previous study, and the relationship was used to examine the accretion rates of 36 Herbig Ae stars by Garcia Lopez *et al.* (2006). More recently, Mendigutía *et al.* (2011) determined accretion luminosities from 38 Herbig Ae and Be stars by examining the UV excess in the Balmer discontinuity, and found a correlation with Br γ luminosity similar to Garcia Lopez *et al.* (2006).

This Chapter investigates two methods of determining the accretion rates of HAeBes - via their Br γ emission, and via modelling of their CO bandhead emission - using spectra obtained from VLT/X-SHOOTER. Section 4.2 discusses the observations and steps taken to reduce the data and remove telluric features. Section 4.3 presents the results obtained from measuring the strength of the Br γ emission, and Section 4.4 presents the results of the CO model fitting. Section 4.5 discusses the relationships between these two results, and Section 4.6 discusses the effect that higher resolution data would have on our CO fitting method.

4.2 Observations & sample selection

The observations were performed with the X-SHOOTER wide-band spectrograph (Vernet *et al.*, 2011) on the VLT in service mode between October 2009 and March 2010 (the first semester of operation). VLT/X-SHOOTER provides simultaneous wavelength coverage from 300–2480 nm using three spectrograph arms - UVB, VIS, and NIR. The original sample of 90 Herbig Ae/Be stars were taken from the catalogues of Thé *et al.* (1994) and Vieira *et al.* (2003), and were selected on sky co-ordinates appropriate for the observing semester. A small number were discarded due to insufficient brightness or ambiguous assignment as a HAeBe star. This resulted in a sample larger than most other published studies by a factor

of 2–5. In addition to the large sample size, the use of X-SHOOTER allows comparison of many spectral features from a single observation, which is important given that HAeBes have been shown to be both photometrically and spectrally variable (Oudmaijer *et al.*, 2001). This Chapter utilises data from the NIR arm, and concentrates on the subset of five objects from the full sample that were determined to exhibit CO first overtone bandhead emission at $2.3\ \mu\text{m}$. A log of the observations of these objects is shown in Table 4.1, and their astrophysical parameters are given in Table 4.2.

Table 4.1: Log of the observations performed with VLT/X-SHOOTER.

Object	Other name	RA (J2000)	Dec (J2000)	S/N	CO (σ)	Br γ (σ)	Date
PDS 133	SPH 6	07:25:04.95	−25:45:49.7	63	5	28	2010-02-24
V596 Car	HD 85567	09:50:28.53	−60:58:03.0	114	17	37	2010-03-06
PDS 37	Hen 3–373	10:10:00.32	−57:02:07.3	136	10	41	2010-03-31
V1052 Cen	HD 101412	11:39:44.46	−60:10:27.9	29	4	42	2010-03-30
PDS 69	Hen 3–949	13:57:44.12	−39:58:44.2	24	3	56	2010-03-29

Table 4.2: Astrophysical parameters of the sample.

Object	Spectral Type	K (mags)	d (pc)	$T_{\text{eff}}^{(8)}$ (K)	$A_{\text{V}}^{(8)}$ (mags)	$L_{\text{bol}}^{(8)}$ (L_{\odot})	$M_{\star}^{(8)}$ (M_{\odot})	$R_{\star}^{(8)}$ (R_{\odot})
PDS 133	B6e ⁽⁵⁾	9.29	590 ⁽¹⁾	14 000	1.92	7.0	3.6	2.2
V596 Car	B7–8Ve ⁽⁶⁾	5.77	1500 ⁽²⁾	12 500	0.76	5000	3.2	2.7
PDS 37	B2e ⁽⁵⁾	6.97	720 ⁽⁵⁾	22 000	5.46	8900	8.3	3.5
V1052 Cen	A0III/IVe ⁽⁷⁾	7.47	118 ⁽¹⁾	10 000	0.62	4.3	2.4	2.5
PDS 69	B4Ve ⁽³⁾	7.15	630 ⁽³⁾	17 000	1.55	250	5.8	3.5

- 1: de Zeeuw *et al.* (1999), 2: Manoj *et al.* (2006), 3: Reipurth & Zinnecker (1993),
4: Drew *et al.* (1997), 5: Vieira *et al.* (2003), 6: van den Ancker *et al.* (1998),
7: Guimarães *et al.* (2006), 8: van den Ancker (priv. communication).

The observations achieved a spectral resolution of $R \sim 8000$ ($\Delta\lambda = 0.28\ \text{nm}$ at

$\lambda = 2.3 \mu\text{m}$) using a slit width of 0.4 arcsec. A single pixel element covers 0.06 nm, while a resolution element covers 4.3 pixels. The atmospheric seeing conditions varied from 1.1–1.6 arcsec between observations. The exposure times ranged from several minutes for the brightest sources, up to 30 minutes for the faintest ones. Nodding along the slit was performed to allow background subtraction. The data were reduced with the ESO pipeline software, which was verified with manually reduced data for a handful of objects to ensure consistency. The data were of high quality, with signal to noise ratios of 100–140 in most cases across the entire sample of HAeBes. Standard stars of spectral type B were observed during each night to allow for removal of telluric spectral features across the NIR range. However, due to the template utilised for standard star observations (which could not be changed), these observations were not integrated for a sufficiently long time to possess the high signal to noise ratio of the science targets, giving them a signal to noise ratio between 30–50 per cent lower.

4.2.1 Telluric line removal

The standard stars observed during the service mode observations did not possess the high signal to noise ratios of the science targets. In an effort to avoid introducing unnecessary random noise into the final reduced spectra, a different method of telluric line removal was investigated.

A model of the transmission of the atmosphere above the observatory was used as a substitute for a telluric standard star. The model atmosphere spectrum was obtained from ESO online interface to the SM-01 advanced sky model¹. For

¹<http://www.eso.org/observing/etc/skycalc/skycalc.htm>

each object, the airmass, season and night period of observation were input to the calculator, and all other inputs were given their default values. The resulting telluric spectrum for each object was returned with a very high spectral resolution of $R \sim 10^6$. For each object, the atmosphere spectrum needed to be ‘tuned’ to the observations by altering three key parameters - the wavelength shift between the two spectra, the broadness of the spectral features, and the strength of the spectral features. Here we discuss how each of these steps was performed:

- The wavelength shift between the model atmosphere spectrum and the object spectrum was obtained by computing the cross correlation function between the two spectra, $P_{\text{obs,atm}}(\Delta x)$, using the `C_CORRELATE` function of IDL, over a specified range of shifts, Δx . The value of Δx giving a minimum difference between the two spectra is chosen as the final wavelength shift.
- The broadness of the spectral features in the model atmosphere spectrum was increased to match the observations by convolving the spectrum with a Gaussian function, $G(\Delta w_\lambda)$, whose width Δw_λ was altered over a specified range of values. For each value of Δw_λ , the standard deviation of the ratio of the object spectrum to the smoothed atmospheric spectrum was calculated, e.g.

$$\sigma(\Delta w_\lambda) = \text{stdev} \left(\frac{F_{\text{obj}}}{G(\Delta w_\lambda) * F_{\text{atm}}} \right). \quad (4.1)$$

For a perfectly matched spectrum, $\frac{F_{\text{obj}}}{F_{\text{atm}}}$ would be equal to one across the wavelength range considered, and $\sigma(\Delta w_\lambda)$ would be equal to zero. For progressively differing spectra, the value of $\sigma(\Delta w_\lambda)$ will increase. Thus, choosing a value of Δw_λ producing a minimum in $\sigma(\Delta w_\lambda)$ corresponds to the best match between the two spectra.

- The strength of the spectral features of the model atmosphere spectrum is scaled to match the object spectrum using the following function,

$$F_{\text{scaled}} = \frac{F_{\text{atm}} + k}{1 + k}, \quad (4.2)$$

where k is a positive or negative constant. As with the broadness of the spectral features, we again calculate the standard deviation of the ratio between the two spectra,

$$\sigma(k) = \text{stdev} \left(\frac{F_{\text{obj}}}{F_{\text{scaled}}} \right), \quad (4.3)$$

and choose a value of k producing a minimum in $\sigma(k)$.

Correcting for each of these factors has an effect on each of the others, so the three tuning steps needed to be performed more than once. The number of cycles of correction was determined on an object by object basis, and was ceased when further correction had no effect on the output spectrum, i.e. when the sequence had converged.

Figure 4.1 shows an illustrative example following both the standard star method (right) and model atmosphere method (left) to remove the telluric absorption lines around the Br γ emission line (upper) and the first two CO first overtone bandheads (lower) in V596 Car. The model atmosphere method performs well across the Br γ region of the spectrum (upper left). The telluric absorption features are almost completely removed by division of the model atmosphere, after the appropriate level of tuning is performed. Applying the standard star method to Br γ (upper right) is complicated by the presence of a Br γ absorption feature in the spectrum of the standard star, creating an artificial increase across the wings

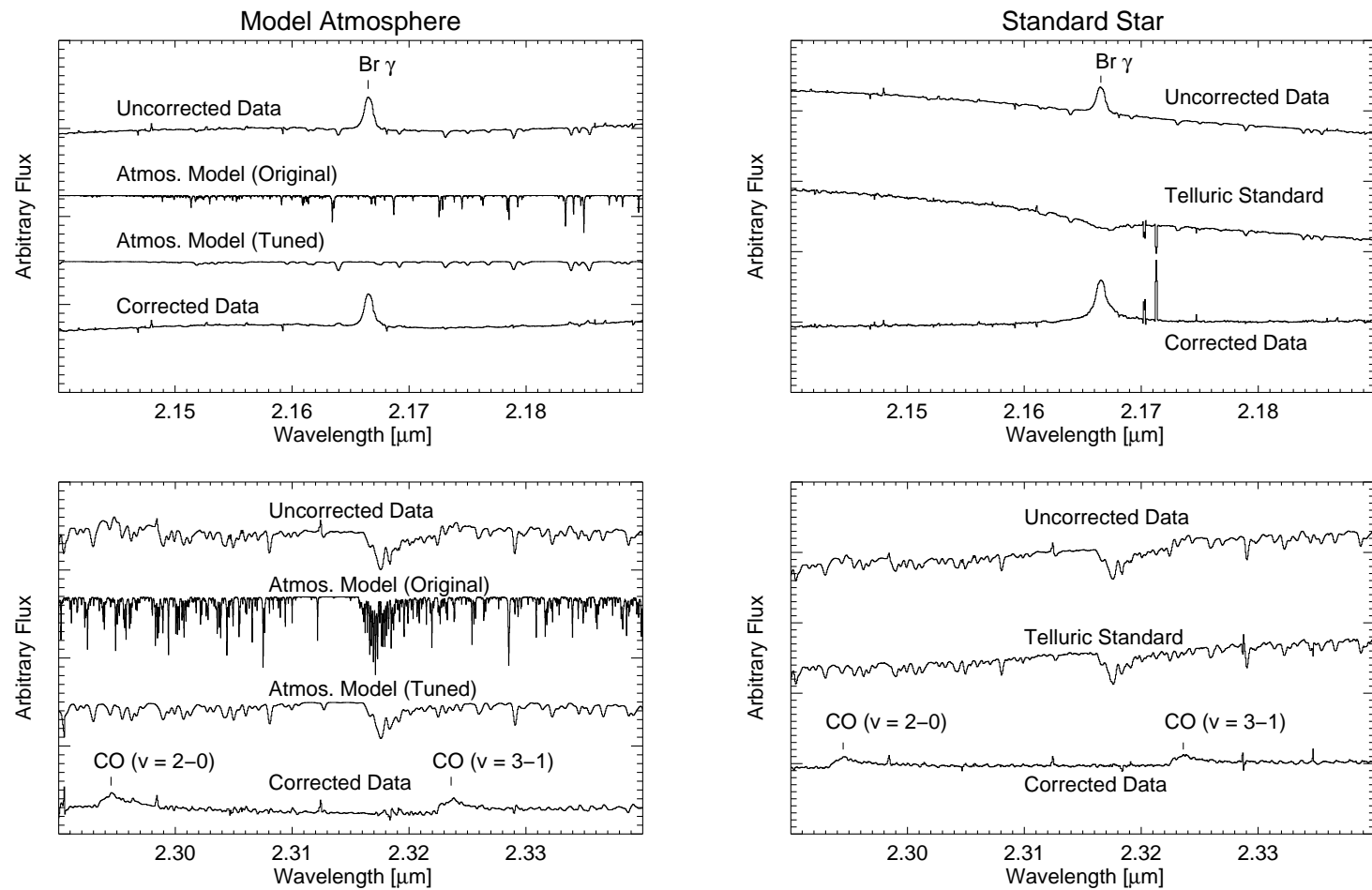


Figure 4.1: Examples of different methods of telluric removal in the spectrum of V596 Car for both Br γ and CO. The left panels show the use of a model atmosphere spectrum, and the right panels show the original telluric standard star method. Scales are the same for all axes.

of the Br γ line in the corrected spectrum.

In contrast, for the CO region of the spectrum, tuning the model atmosphere to an appropriate level is complicated by the many telluric absorption features across this wavelength range, and the relative weakness of the CO emission. As a result, the corrected CO spectrum contains many artefacts of over- and under-correction. For the spectrum of V596 Car, the result could be slightly improved by correcting over smaller wavelength ranges. However, it should be noted that this spectrum has the best quality CO emission of the objects in our sample, and the tuning procedure was much more difficult for other, lower quality spectra. Applying the standard star method to the CO bandheads removed the telluric features much more consistently, at the expense of a slight increase in the noise level of the data.

It was therefore decided to utilise the model atmosphere correction method for the Br γ portion of the spectra, and the original telluric standard stars for the CO portion. While using the standard star method does introduce extra noise to the spectra, this is preferable to the alternative of over and under-correction, which could be mistaken as individual rotational transitions within the bandheads, and would cause problems during subsequent analysis.

4.3 Results from Br γ

In order to derive accretion rates using the methods mentioned earlier, the Br γ line luminosity is required. This is determined from the observations by measurement of the strength of the line by determining the equivalent width, W . The equivalent widths are converted to line luminosities via $L_{\text{line}} = F_{\lambda} W 4\pi d^2$, where F_{λ} is the extinction corrected flux of the object at the wavelength of the spectral feature

(where we assume $A_K = \frac{1}{10}A_V$), d is the distance to the object, and the quantity $F_\lambda W_{\text{line}}$ can be considered the flux of the line, F_{line} . Table 4.3 shows these quantities for the 5 objects in our sample, which are shown in Figure 4.2.

Table 4.3: Br γ line widths (FWHM), equivalent widths (W), line fluxes (F), and line luminosities (L), measured for the spectra shown in Figure 4.2.

Object	FWHM		W	$F_{\text{Br } \gamma}$	$L_{\text{Br } \gamma}$
	(\AA)	(km s^{-1})	(\AA)	(W m^{-2})	(L_\odot)
PDS 133	13.5 ± 0.1	190 ± 1	4.3 ± 0.2	4.0×10^{-17}	4.3×10^{-4}
V596 Car	11.8 ± 0.2	163 ± 3	3.1 ± 0.1	6.4×10^{-16}	4.5×10^{-2}
PDS 37	11.8 ± 0.1	163 ± 1	5.9 ± 0.4	6.4×10^{-16}	1.0×10^{-2}
V1052 Cen	14.6 ± 0.3	200 ± 5	1.0 ± 0.1	4.5×10^{-17}	1.9×10^{-5}
PDS 69	8.7 ± 0.2	120 ± 3	5.5 ± 0.5	3.5×10^{-16}	4.4×10^{-3}

The FWHM and equivalent widths of the lines were measured using the interactive IDL package FEATURE. For each object, ten measurements were taken, and an average of these was reported as the final result, with the error given as the standard deviation. The spectrum of V1052 Cen shows a double peaked line profile, with a separation of 50 km s^{-1} . As the source of this double peaking is unknown, the FWHM is measured across the full width of the line, and should be considered a maximal value.

4.3.1 Accretion rates

As mentioned above, the luminosity of Br γ has previously been shown to correlate well with the accretion luminosity of intermediate mass YSOs, giving rise to several calibrated relationships between the two quantities. For YSOs with masses up to those of Herbig Ae stars, Calvet *et al.* (2004) and Garcia Lopez *et al.* (2006) found

that

$$\log \frac{L_{\text{acc}}}{L_{\odot}} = (0.9 \pm 1.4) \times \log \frac{L_{\text{Br}\gamma}}{L_{\odot}} + (2.9 \pm 4.4). \quad (4.4)$$

More recently, Mendigutía *et al.* (2011) looked at a large sample of Herbig Ae and Be stars and determined that

$$\log \frac{L_{\text{acc}}}{L_{\odot}} = (0.91 \pm 0.27) \times \log \frac{L_{\text{Br}\gamma}}{L_{\odot}} + (3.55 \pm 0.80). \quad (4.5)$$

We have used these two relationships (henceforth known as C1 and C2) to determine the accretion luminosities of the objects. Once the accretion luminosity has been determined, the relation

$$\dot{M} = \frac{L_{\text{acc}} R_{\star}}{GM_{\star}} \quad (4.6)$$

can be used to determine the mass accretion rate, provided the stellar parameters are known. Table 4.4 shows the accretion luminosities and mass accretion rates that were determined for each object.

Table 4.4: Accretion luminosity and mass accretion rates of the objects from Br γ based on the relationships of C1: Garcia Lopez *et al.* (2006) and C2: Mendigutía *et al.* (2011).

Object	$L_{\text{acc}} (L_{\odot})$		$\dot{M} (M_{\odot} \text{ yr}^{-1})$	
	C1	C2	C1	C2
PDS 133	0.9	3.1	$2.0_{-1}^{+3} \times 10^{-8}$	$6.3_{-4}^{+10} \times 10^{-8}$
V596 Car	60	210	$1.6_{-1}^{+1} \times 10^{-6}$	$6.3_{-2}^{+4} \times 10^{-6}$
PDS 37	16	55	$2.0_{-1}^{+3} \times 10^{-7}$	$8.0_{-4}^{+8} \times 10^{-7}$
V1052 Cen	0.05	0.18	$2.0_{-2}^{+10} \times 10^{-9}$	$6.3_{-5}^{+30} \times 10^{-9}$
PDS 69	7.3	25	$1.6_{-1}^{+5} \times 10^{-7}$	$5.0_{-4}^{+10} \times 10^{-7}$

It is found that the relationship C2 gives mass accretion rates that are ap-

proximately 3–4 times higher than those determined with relationship C1. The C2 relationship was determined from a sample of stars most similar to those in our sample, so it is likely that the accretion rates determined from C2 are more applicable. However, for completeness, we include the accretion rates obtained from both relationships in our subsequent analysis.

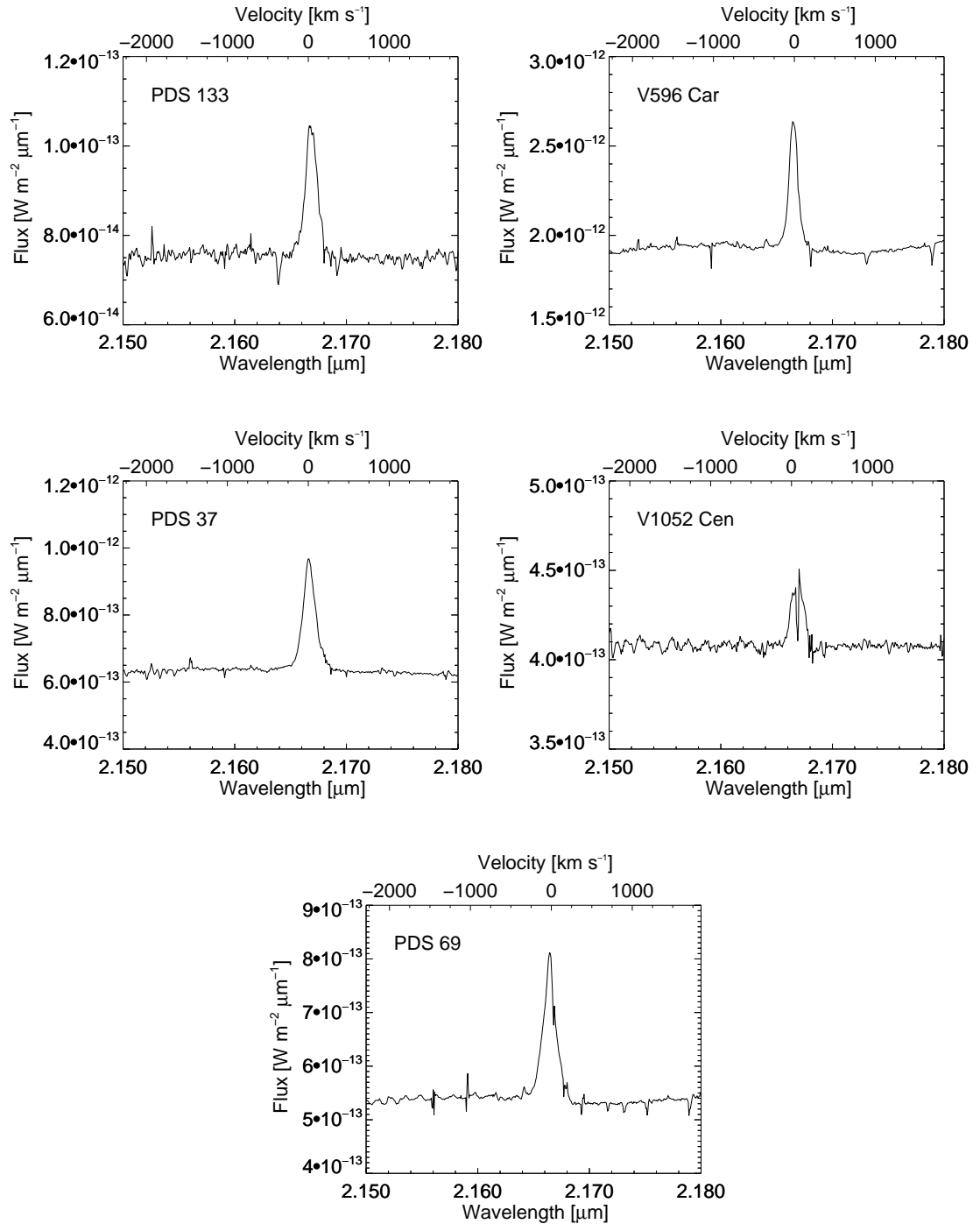


Figure 4.2: Br γ emission lines for the sample of HAeBes, corrected for continuum slope. The velocity scale is centred on 2.165 μm .

4.4 Results from CO

The five HAeBe objects described in Table 4.1 were chosen based on the detection of CO first overtone bandhead emission in their spectra. This emission has been modelled using precisely the same methods as described in Chapter 3.

4.4.1 A case study: V596 Car

The disc model used within the CO fitting routine needs to be established. Two possible choices are considered - disc model A; an analytic model, and disc model B; a physical model based on Carr (1989) and Chandler *et al.* (1995) (see Chapter 3 for full details). To determine which disc model was most appropriate to fit these data, best fits obtained with both disc models to the spectrum of V596 Car were compared. The fitting routines were repeated with multiple starting positions spread across the parameter space, to ensure no local minima were recovered. The fit with the lowest χ_r^2 value was chosen as the final best fit for the spectrum. For disc model B, we take the anomalous viscosity parameter, α , to be 0.01, following the SED fitting of a HBe object by Merín *et al.* (2004). Figure 4.3 shows the results of the fitting for each disc model.

The best fit to the V596 Car spectrum using the analytic disc model A struggles to reproduce the shoulders of the $v = 2 - 0$ and $4 - 2$ bandheads, and overestimates the peaks of the $v = 3 - 1$ and $4 - 2$ bandheads. This model fit also struggles to reproduce the level of the rotational transitions in the $v = 3 - 1$ bandhead. The best fit involving model B also struggles slightly to reproduce the shoulders of the $v = 2 - 0$ and $3 - 1$ bandheads, however the strength of the rotational transitions and the level of the bandhead peaks in the model are more consistent with the

data, which is reflected in the lower χ_r^2 value.

The number of free parameters in model A may be too large for the downhill simplex algorithm to accurately obtain a best fit using data of this quality, even with multiple starting positions in parameter space. Model B reproduces all of the observed bandheads with good accuracy. Therefore, it was decided to perform the fitting of the full sample of objects using disc model B.

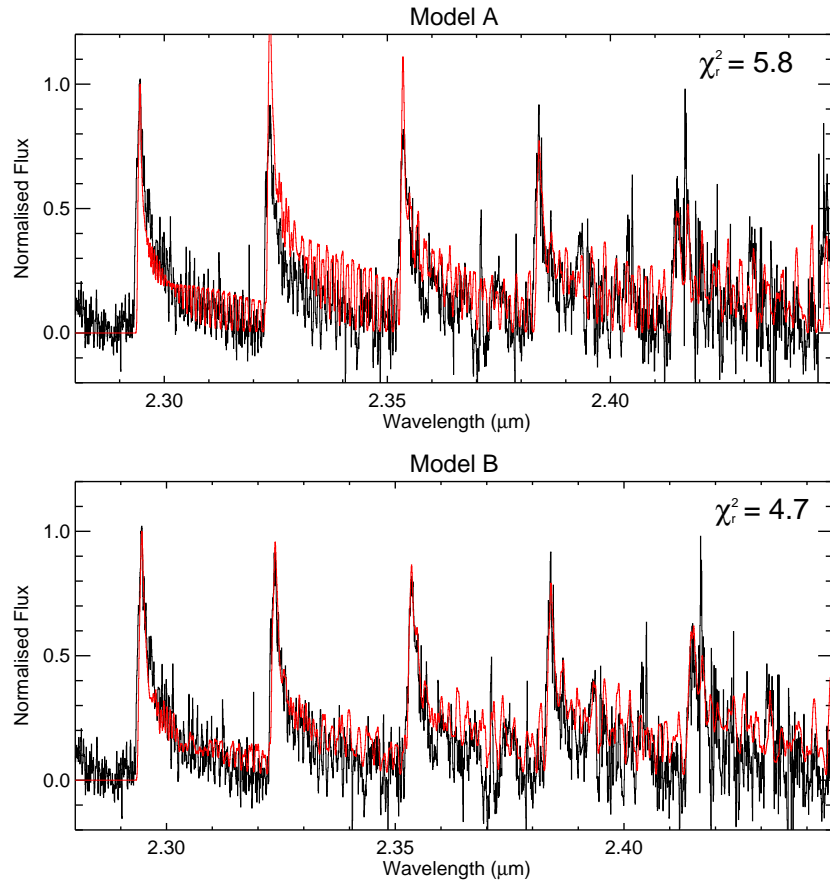


Figure 4.3: Comparison of best fitting models to the spectrum of V596 Car using disc model A and disc model B. The fit using model B provides the best fit, which is reflected in the lower χ_r^2 value.

Table 4.5: Measured observational parameters from the first bandhead of the CO first overtone emission.

Object	W (Å)	F_{CO} (W m ⁻²)	L_{CO} (L_{\odot})
PDS 133	7.9±0.2	7.3×10 ⁻¹⁷	7.0×10 ⁻⁴
V596 Car	13.1±0.1	2.7×10 ⁻¹⁵	2.0×10 ⁻¹
PDS 37	6.2±0.3	6.4×10 ⁻¹⁶	1.0×10 ⁻²
V1052 Cen	8.2±0.3	3.5×10 ⁻¹⁶	1.5×10 ⁻⁴
PDS 69	10.3±0.5	6.3×10 ⁻¹⁶	7.8×10 ⁻³

4.4.2 Multiple bandheads

The larger wavelength range of X-SHOOTER allows more than a single CO bandhead to be investigated. The CO emission model has been extended to include up to the $v = 6 - 4$ bandhead. Figure 4.4 shows the effect of altering the free parameters of disc model B on these five bandheads. Each spectrum has been normalised to its peak flux and shifted vertically for clarity. The effect of an increase in the mass accretion rate (top panel) changes the ratio of the bandhead peaks to one another. This is due to high \dot{M} causing an increase in viscous heating, which in turn causes a hotter disc (allowing higher energy levels to become more populated), and an increase in surface density in the disc increasing optical depths. At low inclinations, corresponding to a more face-on disc, the individual rotational lines are much more prominent, and a blue shoulder on the bandheads is not apparent. At high inclinations (a more edge-on disc), the shoulder is clearly seen across all bandheads, and the rotational lines appear less clear due to the red- and blue-shifted components from each transition. The effect of an increase in line width also changes the relative heights of the different bandheads, and also acts to raise the level of the rotational transitions with respect to the bandhead peaks, which

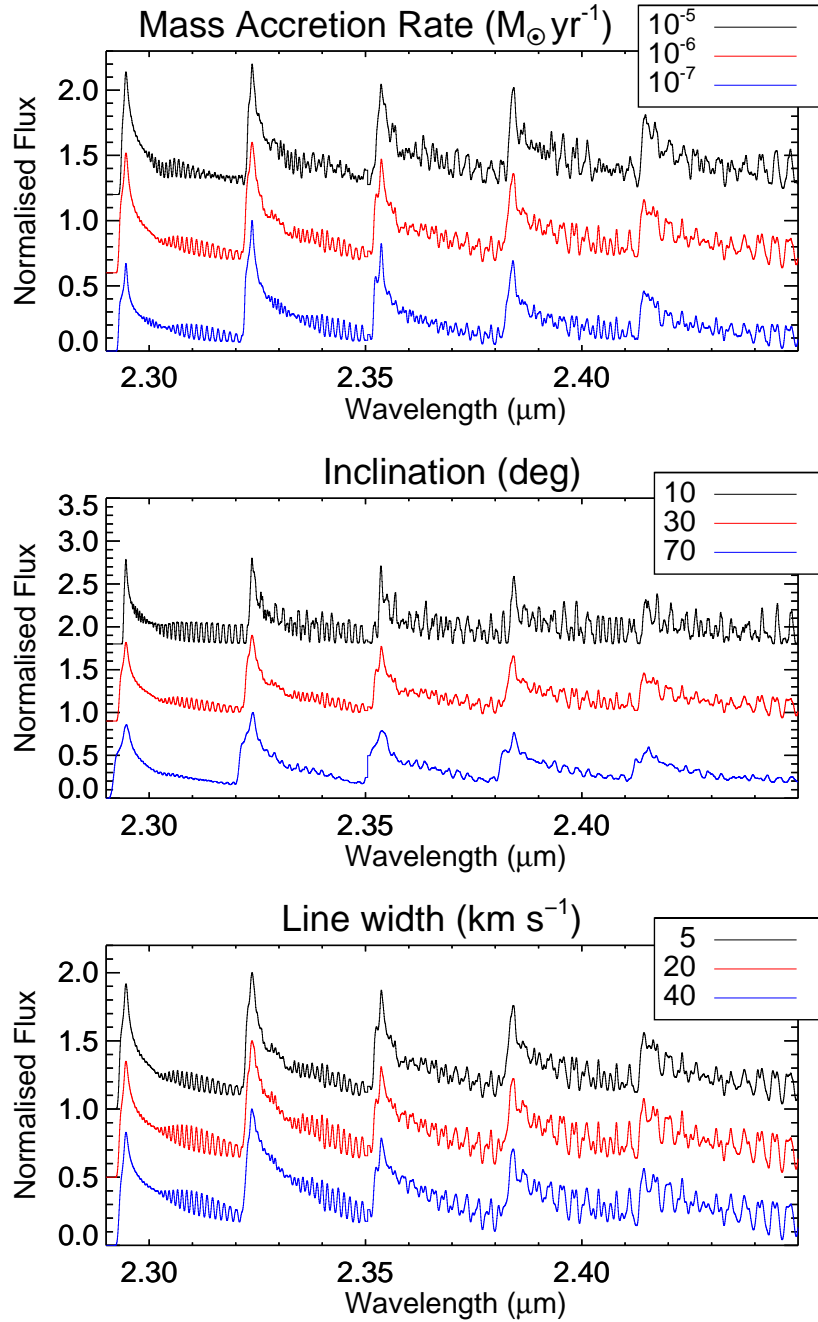


Figure 4.4: Spectra produced using disc model B while varying mass accretion rate (top), disc inclination (middle), and intrinsic line width (bottom). Each spectrum is normalised to its peak flux, and vertically shifted for clarity. The spectral resolution is consistent with the X-SHOOTER data, $R \sim 8000$.

is caused by the broader intrinsic line shapes that are assigned to each individual rotational transition.

The inclusion of the additional first overtone bandheads on the fitting process was also investigated. Again, V596 Car is used as a case study. The fitting routine was performed as usual, however the wavelength range over which the χ_r^2 statistic was calculated was restricted to include only the first, second and third bandhead peaks (corresponding to the $v = 2 - 0$, $3 - 1$ and $4 - 2$ bandheads, respectively). Therefore, the parts of the spectrum beyond these wavelength ranges was not considered when deciding whether the goodness of fit. Figure 4.5 and Table 4.6 show the results of this.

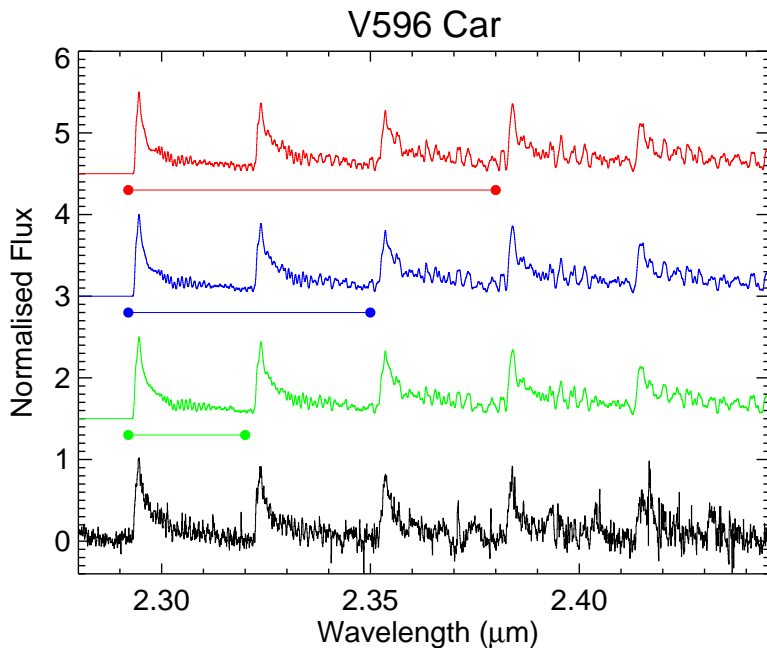


Figure 4.5: Fits obtained to the spectrum of V596 Car (black) while considering one (green), two (blue) and three (red) bandheads within the AMOEBA fitting routine, using disc model B. Horizontal lines show the wavelength range over which the χ_r^2 statistic was calculated during the fitting process.

Table 4.6: Best fitting parameters for the fits shown in Figure 4.5, and the final best fit obtained.

Bandheads fit	R_i (au)	R_o (au)	\dot{M} ($M_\odot \text{ yr}^{-1}$)	$\Delta\nu$ (km s^{-1})	i ($^\circ$)	χ_r^2
1	0.03	0.22	3.8×10^{-8}	2.7	19	1.4
2	0.03	0.22	5.2×10^{-8}	2.4	16	2.4
3	0.03	0.22	3.2×10^{-8}	2.5	15	3.4
All	0.03	0.23	$1.3_{-*}^{+24} \times 10^{-7}$	2.4_{-3*}^{+1}	13_{-11}^{+10}	4.7

*: The value of χ_r^2 did not change by one over the allowed parameter range.

It can be seen that, qualitatively, the fit involving only the first bandhead reproduces the other four bandheads relatively well, and shows little difference to the fit involving three bandheads. This is reflected quantitatively in the fit parameters, apart from the mass accretion rate, \dot{M} , which is underestimated when using the single bandhead, when compared to the best fit involving all five bandheads (shown in Section 4.4). However, it can be seen from the associated errors of the mass accretion rate, which are large, that this parameter is not well constrained by our modelling. The inclination, i , is also higher in the single bandhead fit, but lies within the error ranges of the final best fit to V596 Car. This would suggest that fits involving a smaller number of bandheads can be extrapolated to longer wavelengths with reasonable accuracy, but that the mass accretion rate may be difficult to determine from such fits.

4.4.3 Full sample results

The spectrum of each object was corrected for telluric features using the method described previously in Section 4.2.1. The continuum was subtracted using fits obtained with the IRAF packages ONEDSPEC and CONTIN. The spectra were

then normalised to the peak emission of the first bandhead ($v = 2 - 0$) which was obtained by smoothing the peak, to reduce the effect of noise. The fitting procedure was then performed using disc model B. The number of bandheads visible within the spectra differed, and therefore the wavelength range of fitting was determined on an object by object basis, and included at least three bandheads in all cases, before excessive noise in the data made detection of further bandheads problematic. Figure 4.6 and Table 4.7 show the results of the model fitting and their associated best fitting parameters, and Figure 4.7 shows a graphical comparison of the best fitting parameters for each HAeBe.

Table 4.7: Parameters obtained from the CO fitting for each of the five HAeBes. Solid lines indicate the mean of each quantity, and dashed lines indicate the standard deviation.

Object	R_i (au)	R_o (au)	\dot{M} ($M_\odot \text{ yr}^{-1}$)	$\Delta\nu$ (km s^{-1})	i ($^\circ$)	χ_r^2
PDS 133	0.02	0.21	$3.2^* \times 10^{-8}$	3.8_{-4}^{+16}	11_{-11}^{+44}	2.8
V596 Car	0.03	0.23	$1.3_{-*}^{+24} \times 10^{-7}$	2.4_{-3}^{+1}	13_{-11}^{+10}	4.7
PDS 37	0.07	0.59	$9.0^* \times 10^{-8}$	2.6_{-3}^{+5}	13_{-13}^{+11}	3.9
V1052 Cen	0.02	0.16	$8.2^* \times 10^{-8}$	1.8_{-2}^{+10}	9_{-9}^{+23}	1.9
PDS 69	0.05	0.43	$4.2^* \times 10^{-8}$	2.2^*	22^*	1.0

*: The value of χ_r^2 did not change by one over the allowed parameter range.

In all objects, the shoulders of the bandheads are well fit by the model spectra. These regions of the spectra are affected most by the inclination of the disc, therefore this suggests the inclinations of the objects should be well constrained. However, it can be seen from the model fitting errors that the inclinations are poorly constrained (with the exception of V596 Car). The level of noise in the spectra is close to, or greater than, the strength of the individual rotational lines,

making them difficult to distinguish and fit. Without the combination of well defined rotational lines and bandhead shoulders, the fitting routine struggles to constrain the inclinations of the objects. This is also reflected in the intrinsic linewidths of the fits, which are also poorly constrained (even in the case of V596 Car), because the fitting routine cannot easily distinguish the rotational lines from the background noise.

The mass accretion rate is particularly poorly constrained compared to the other fit parameters, with only V596 Car displaying a single error limit within the entire accretion rate range explored. However, this is not surprising given that the exploration of models with varying mass accretion rates (shown in Figure 4.4) display relatively small changes in the spectra, which would be lost in the noise of data of this quality.

In an attempt to overcome the problem of noise in the spectra disrupting the fitting routine, the spectra were re-fit by only considering the minimisation of χ_r^2 over the $v = 2 - 0$ bandhead, which is the strongest in most cases and is therefore less affected by such noise. As before, the fitting routine was started with multiple positions across the parameter space to avoid local minima, and the final best fit was determined by the lowest χ_r^2 value. However, each individual fitting run resulted in minima with similar χ_r^2 values (with less than 5 per cent difference in all cases), but fit parameters that varied considerably across the fitting range. While consideration of a single bandhead can be used to extrapolate the fit to other bandheads when the data quality is reasonably high (see Section 4.4.2), when data quality is lower, this leads to poorly constrained fits. Therefore, because of this degeneracy in the results, it was decided to proceed with the results obtained from

the fits to multiple bandheads, where this information was retained in the fitting process.

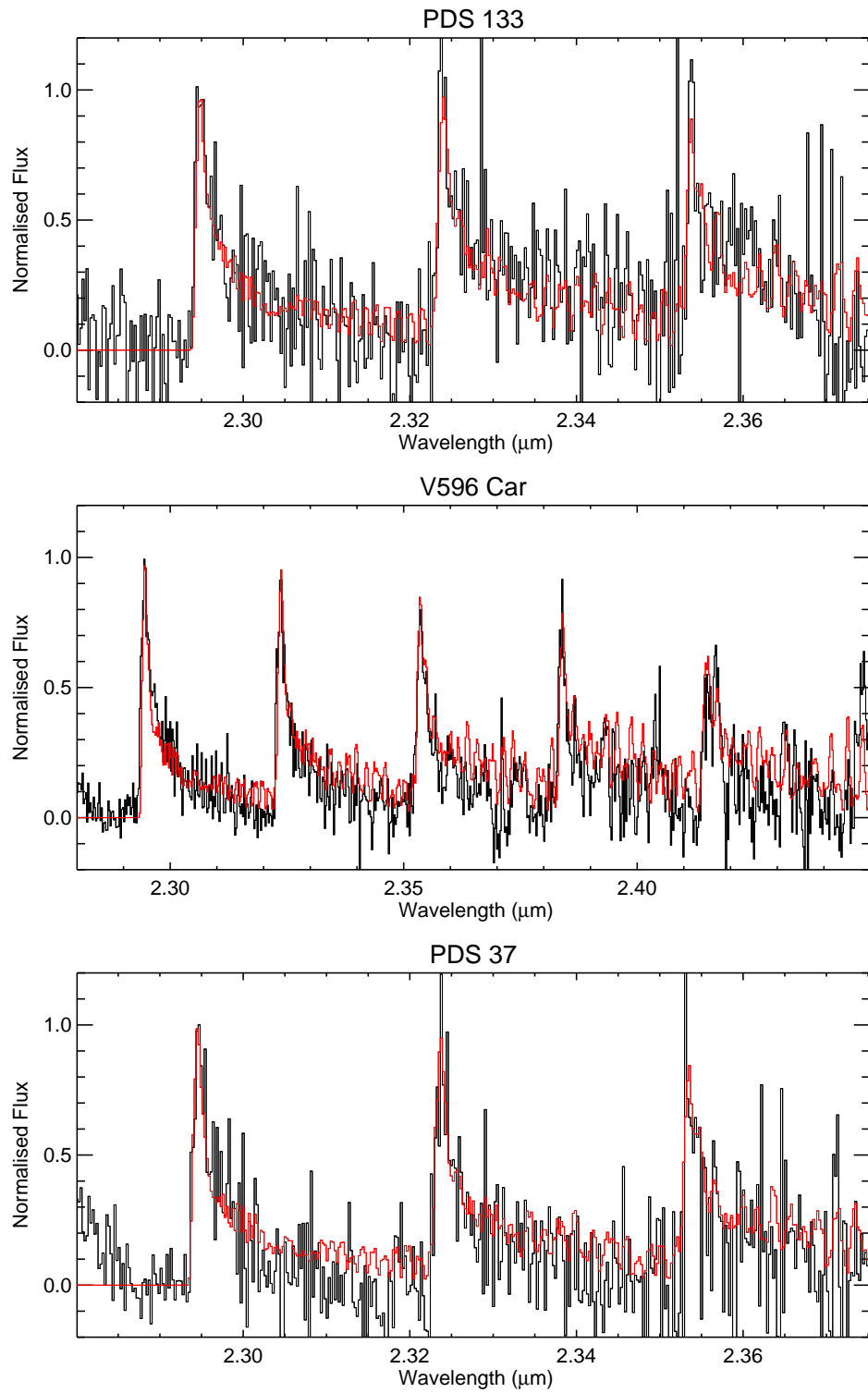


Figure 4.6: Spectra (black) and model fits (red) to the CO emission of the objects in the sample, using disc model B. For clarity, the spectra have been re-binned by a factor of 4.

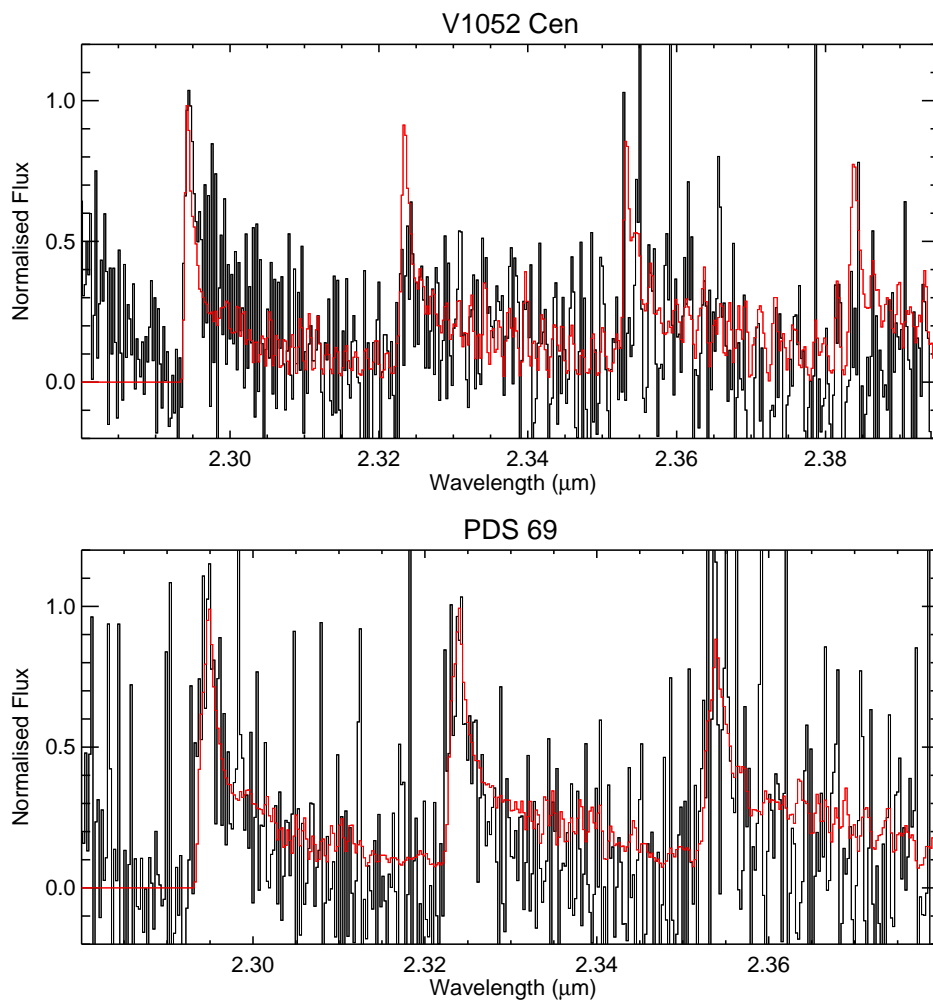


Figure 4.6: Continued.

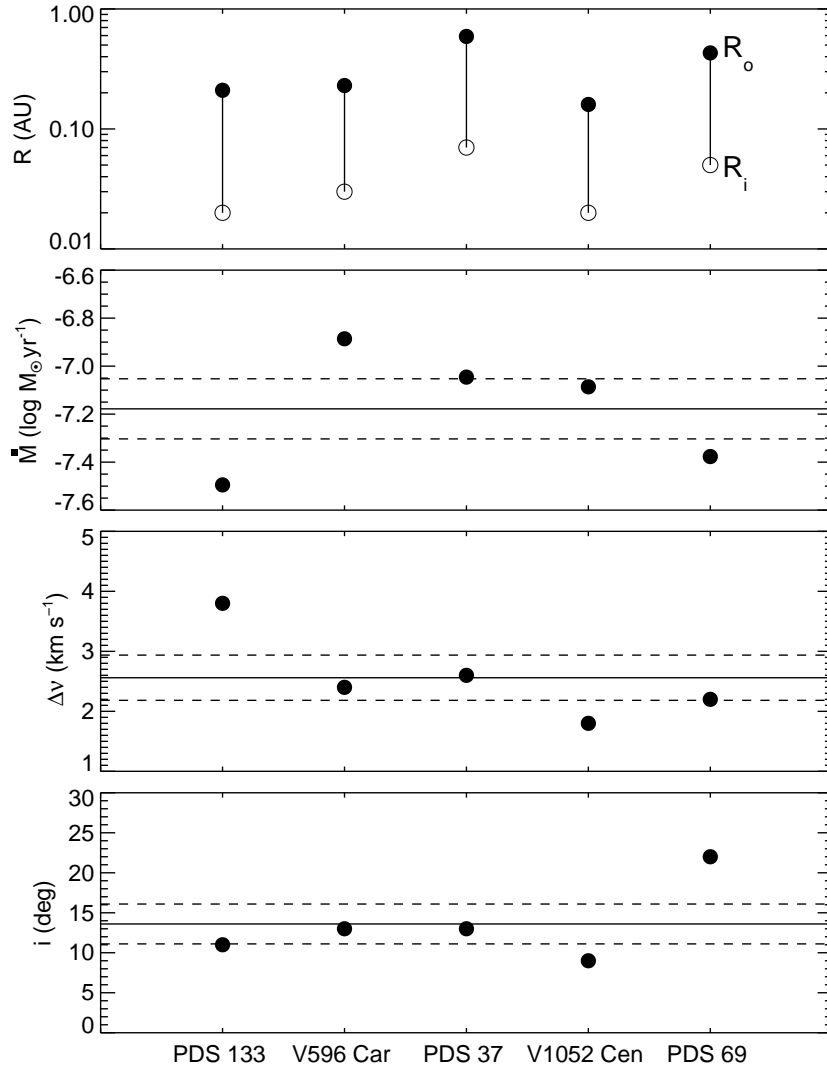


Figure 4.7: Comparison of the best fitting parameters for each HAeBe obtained from the CO fitting. The top panel shows the inner and outer radius of the CO disc (R_i , R_o). In all other panels, the mean and standard deviation are denoted with solid and dashed lines, respectively.

4.5 Analysis & Discussion

We find Br γ emission in all 5 of the HAeBe objects, at various strengths. The strongest emission compared to the continuum occurs in PDS 133, while the weakest is V1052 Cen. The FWHM of the Br γ emission ranges from 120–200 km s⁻¹, which is approximately six times the thermal linewidth expected for Hydrogen gas at the effective temperatures of the central protostars (20–30 km s⁻¹), which suggests the lines are also broadened by non-thermal mechanisms. The Br γ lines are also much broader than the individual linewidths obtained from the CO fitting, suggesting a separate origin for both the Br γ and CO emission.

In total, 5 objects displayed CO first overtone bandhead emission in their spectra, which corresponds to a detection rate of approximately 6 per cent. This is in contrast to other studies of CO emission in young stellar objects, where detection rates of around 20 per cent have been reported in low to intermediate mass YSOs (e.g. Carr, 1989) and 17 per cent for massive YSOs (e.g. Cooper *et al.*, 2013). It is unclear why our detection rate is substantially lower than these other studies. A possible explanation is that many HAeBes may not have enough gas in their circumstellar environments to allow sufficient excitation of the CO bandheads, but direct measurements of the amount of gas in these systems would be required to confirm this hypothesis.

In addition to the low detection rate, the objects in our CO sample are mainly of spectral type HBe (and V1052 Cen is of type HAO, having previously been classified as HBe). Therefore, these objects are hotter and more massive than their HAe-type counterparts. It could be that HAe stars not hot enough to excite the CO sufficiently for it to be detected.

The intrinsic linewidths obtained from the fitting are of the order of the thermal linewidths of CO gas between 1000-5000 K ($1-3 \text{ km s}^{-1}$), however it should be noted that these values are not well constrained and possess large errors in most cases. The mass accretion rates obtained from the CO fitting procedure are clustered around low values, close to the lowest accretion rate searched by the fitting routine. The inclinations are similarly clustered at low values, with an average of approximately 14° . It is possible that a geometric selection effect is occurring, and that to detect sufficiently strong CO bandhead emission, we require the disc to be close to face on. From the perspective of the observer, this would correspond to the CO emission region covering a larger area on the sky, whereas an edge on disc of the same size would cover a smaller region. However, given the issues with the fitting discussed previously, and that no such geometric selection effect is seen in the MYSO spectra presented in Chapter 3, it is more likely that this is due to the fitting routine being unable to distinguish features in the data that would allow other inclinations to be recovered.

The luminosities of the Br γ and CO $v = 2-0$ bandhead are compared in the left panel of Figure 4.8. There is a strong, positive correlation between the quantities. A least squares fit to the data obtained $\log L_{\text{CO}} = (1.06 \pm 0.17) \log L_{\text{Br}\gamma} + (0.26 \pm 0.44)$, which corresponds to an almost one-to-one relationship. In contrast, the mass accretion rates determined using the Br γ and CO fitting (shown in the right panel of Figure 4.8) do not follow this correlation. The clustering of the accretion rates from CO is particularly obvious. It is therefore clear that the fitting of the CO bandheads using the methods described does not properly constrain the mass accretion rates of the HAeBes using data of this quality.

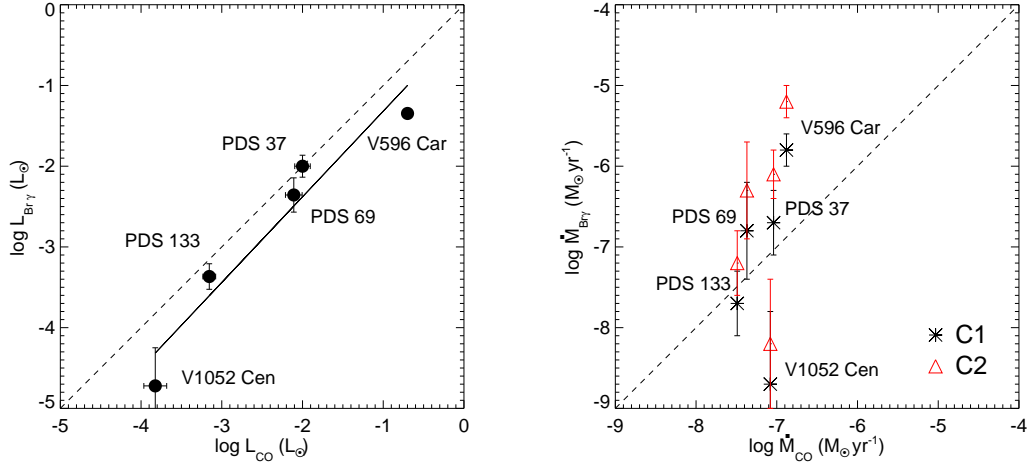


Figure 4.8: A comparison of the line luminosities (left) and mass accretion rates (right) obtained from the CO and Br γ lines for each of the HAeBes. The dotted lines show a one-to-one relationship. A line of best fit to the luminosity relationship ($\log L_{\text{CO}} = 1.06 \times \log L_{\text{Br}\gamma} + 0.26$) is shown in black. Errors for \dot{M}_{CO} are not shown because in most cases they span the entire fitting range.

4.6 Exploring the effect of higher resolution data

One of the objects in the sample, V1052 Cen has also been the subject of a similar investigation involving CO bandhead emission by Cowley *et al.* (2012). Using high spectral resolution VLT/CRIRES data, they find fits to their data assuming a disc of CO that is at most 0.8–1.2 au in extent, at a temperature of 2500 K, and assuming the disc is edge on, following the inclination of 80° determined from Fedele *et al.* (2008). The best fitting model to our data for V1052 Cen is a disc from 0.02–0.16 au at a low inclination of 9° , which is in stark contrast to the results obtained from the higher resolution CRIRES data.

In order to more fully assess the effect of higher spectral resolution observations on our investigation, the data from Cowley *et al.* (2012) were obtained from the

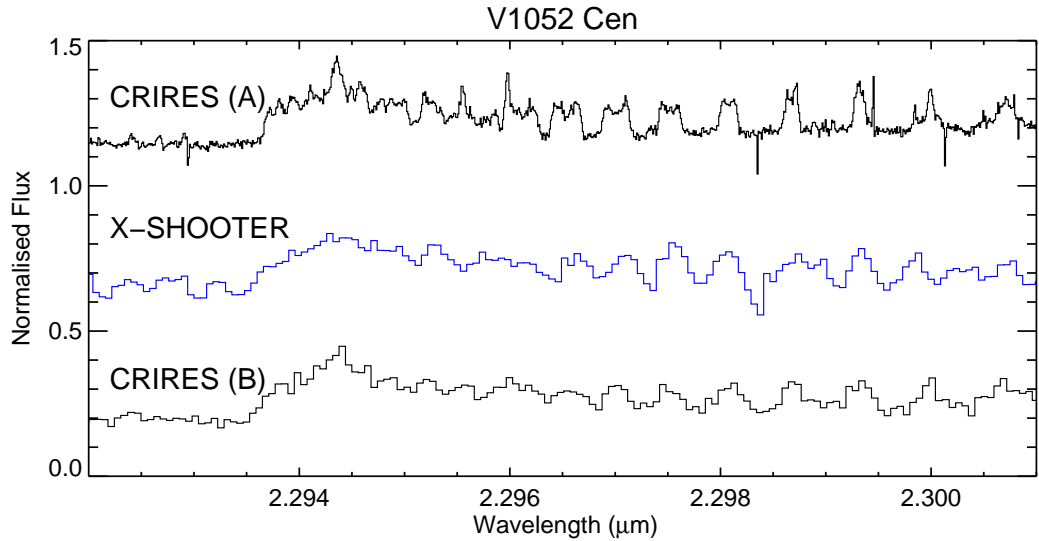


Figure 4.9: Comparison of CRIRES and X-SHOOTER data for V1052 Cen. The CRIRES spectrum at $R \sim 90\,000$ (CRIRES A) shows much detail that is masked when the spectrum is degraded to the X-SHOOTER resolution of $R \sim 9\,000$, re-binned, and given random noise (CRIRES B). The original X-SHOOTER data is shown for comparison. All spectra have been normalised to their continuum and shifted vertically for clarity.

ESO archive¹. Figure 4.9 shows the spectra of V1052 Cen from CRIRES and X-SHOOTER. It can be seen that the increase in resolution by approximately a factor of ten from X-SHOOTER to CRIRES allows for many more spectral features to be visible, including features in the blue shoulder of the bandhead and ‘M’ shaped rotational line profiles. When the CRIRES spectrum is convolved with a Gaussian corresponding to the spectral resolution of the X-SHOOTER data, re-binned the appropriate amount, and given a similar level of random noise, the data appears similar to the X-SHOOTER spectrum (CRIRES B). This suggests the differences in the spectra are mainly a resolution effect, and not due to spectral variability of the source. The main difference between our best fit to the X-SHOOTER data

¹ESO programme 087.C-0124(A)

and the best fit of Cowley *et al.* (2012) to the CRIRES data is that they find good model fits using much higher inclination of approximately 80° , compared to our best fit of 9° . It can be seen from Figure 4.9 that the X-SHOOTER data lacks the defined blue shoulder of the degraded CRIRES spectrum, which along with the masking of the double peaked rotational line profiles, does not allow our fitting routine to recover a solution at high inclinations.

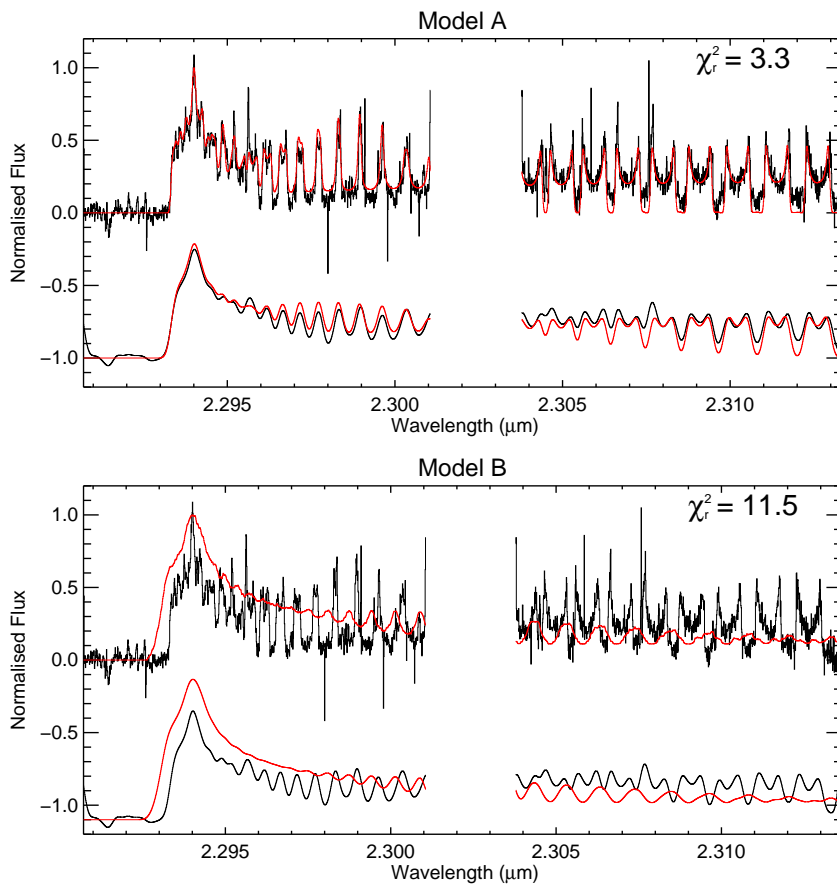


Figure 4.10: Model fits to the CRIRES data of V1052 Cen using disc model A (upper panel) and disc model B (lower panel), with associated χ_r^2 values. The line beneath the main fit shows the data and model fit after degradation to the spectral resolution of the X-SHOOTER observations.

To determine if the use of higher resolution data would better constrain the

Table 4.8: Best fitting model parameters for the high resolution CRIRES data of V1052 Cen using disc model A.

V1052 Cen		
R_i	$0.67^{+0.12}_{-0.07}$	au
R_o	0.87	au
N_i	$1.0^{+8}_{-*} \times 10^{20}$	cm^{-2}
T_i	2800^{+100}_{-400}	K
q	-4.0^{+*}_{-*}	–
p	$-3.9^{+2.4}_{-*}$	–
$\Delta\nu$	5.7^{+11}_{-7}	km s^{-1}
i	54^{+3}_{-5}	degrees

*: The value of χ_r^2 did not change by one over the allowed parameter range.

fit parameters to V1052 Cen, the CO fitting routine was performed on the high resolution CRIRES data using both disc model A and B. The results are shown in Figure 4.10. Contrary to the previous disc model testing, model B is unable to adequately fit the higher resolution data, while model A has the freedom to reproduce the features across the entire bandhead - which can be seen by inspection and from the much lower χ_r^2 value. Table 4.8 shows the parameters of the best fitting model to the data using disc model A. These values differ slightly from Cowley *et al.* (2012), but it should be noted that their model and fitting routine were different to the methods presented here. For instance, they assume an isothermal ring of CO with fixed parameters such as inclination, and the fitting was performed visually with no methodical χ_r^2 minimisation being performed. However, the results here still suggest a narrow ring of CO, at approximately the same temperature and distance from the central protostar.

While adequate fits are obtained to medium resolution spectra, it can be seen from analysis of high resolution spectra that the physical model based on Carr

(1989) and Chandler *et al.* (1995) it not appropriate. It may not contain the relevant physics to properly described the circumstellar environment in which the CO is excited to emit first overtone emission.

4.7 Conclusions

This Chapter has presented results on VLT/X-SHOOTER infrared spectra of five HAeBe objects, examining their Br γ and CO first overtone bandhead emission. The equivalent widths of the Br γ emission lines were measured and converted to line luminosities. The line luminosities were then converted to accretion luminosities using two relationships based on the work of Garcia Lopez *et al.* (2006) and Mendigutía *et al.* (2011). The accretion luminosities were used, along with stellar parameters, to determine an accretion rate for each object. The CO bandheads were fit using the methods described previously in Chapter 3. Two models describing the physical disc structure were tested on the best quality CO spectrum, and it was determined that a physical model based on balancing the heating and cooling within the disc most accurately reproduced the data. This model was then used to fit the other HAeBe CO spectra, deriving disc sizes, inclinations, mass accretion rates and intrinsic linewidths of the CO emitting gas.

Comparison of the mass accretion rates obtained from the CO and the Br γ showed that the CO fitting does not constrain the mass accretion rate well for data of this quality and spectral resolution. High resolution VLT/CRIRES archive data for one object is presented, and compared to the lower resolution X-SHOOTER spectra. The CRIRES data shows many spectral features that are not seen in the X-SHOOTER spectra. However, when degraded, the CRIRES data is comparable

to the X-SHOOTER data. Finally, the high resolution data are fit with the two disc models mentioned previously. The model based on heating and cooling as in Carr (1989) and Chandler *et al.* (1995) is unable to reproduce the features in the spectrum, while the previously discarded analytic model produces a good fit. It is concluded that high resolution data are required to perform the CO fitting in this way, and that the physical disc model based on the heating and cooling mechanisms, while able to fit low to medium resolution spectra, is not able to reproduce the features seen in high resolution spectra.

Thus, fits obtained to CO bandhead spectra of medium to low resolution must be treated with caution. While the model fit may appear to be acceptable when considering lower resolution data, the physical model of heating and cooling described in Carr (1989) and Chandler *et al.* (1995) is clearly oversimplified, and does not contain the relevant processes required to properly fit features seen in high resolution observations of CO bandhead emission. Thus, previous results obtained using this method should be treated with caution until high resolution follow-up observations can be performed.

Chapter 5

Conclusions

5.1 Summary

This thesis contains descriptions of work on several aspects of discs around young stars that are in the process of forming. The topics addressed are the modelling and observations of molecules within these discs, and how observations of these molecules can be used as a probe of the disc environment. The following sections summarise the important findings that have been presented.

Chemistry in a gravitationally unstable protoplanetary disc

The chemistry occurring within circumstellar discs around young solar-like stars has important consequences for theories of planet formation, and the evolution of pre-biotic molecules which may lead to life. Observations of the chemistry occurring in these discs have been made with telescopes such as the Plateau de Bure Interferometer and the Submillimeter Array (Dutrey *et al.*, 2007; Henning *et al.*, 2010; Öberg *et al.*, 2010, 2011). Many authors have used physical disc

models, along with chemical evolution networks, to compute the evolution of the chemistry within these discs in order to explain the observations (Fogel *et al.*, 2011; Heinzeller *et al.*, 2011; Walsh *et al.*, 2010; Woitke *et al.*, 2009b).

These models have used varying degrees of physical complexity, ranging from the single point models to two-dimensional treatment of discs that are considered axisymmetric. However, in the earliest stages of star formation, in Class 0 sources, disc masses may be comparable to the mass of the central protostar, and the assumption of axisymmetry may not be appropriate. Models have shown that in these cases, the discs may become gravitationally unstable, and rotating spiral arms will develop in the disc. These arms lead to shocks that result in increases in the temperature and density of the disc material, which alter the chemistry occurring within the disc. To determine the magnitude of the effect of this, a model of a young gravitationally unstable disc was used as physical input to a gas-grain chemical network, in the first study of non-axisymmetric disc chemistry.

It was found that the shocks associated with the spiral arms caused desorption of various chemical species from the surfaces of dust grains, which increased their gas-phase abundances in regions of the disc which would be normally too cold for this desorption to occur. In addition to shock-induced desorption, gas-phase reactions that would normally not be energetically favourable occur in warm regions that have recently been shocked, leading to the enhancement of the abundances of certain species. In contrast to axisymmetric models of more evolved discs that see significant vertical stratification of species and depletion near the mid-plane of the disc, substantial gas-phase abundances are found near the mid-plane, caused by the large scale mixing effect of the spiral arms.

CO bandhead emission in massive young stellar objects

The formation of massive stars is currently not well understood. Theoretical models have shown that it may be possible to form a massive star when considering a scaled up version of low mass star formation, via an accretion disc, but observational evidence of this is lacking. The precursors to massive stars, MYSOs, are therefore the subject of much study. However, confirming the presence of discs around massive young stellar objects with direct observations is difficult, because the MYSOs are highly obscured and invisible to optical radiation. Indirect methods must be used to probe the circumstellar environment of these objects.

The CO molecule offers just such an indirect probe. At the temperatures and densities that occur in circumstellar discs close to the central protostar ($T = 2000 - 5000$ K, $n > 10^{11}$ cm⁻²), the CO molecule is excited both rotationally and vibrationally, creating rovibrational emission in the form of CO bandheads. The first overtone of this emission occurs in the infrared at $2.3 \mu\text{m}$, which suffers from less extinction than optical wavelengths, allowing access to these close circumstellar regions.

High spectral resolution data were obtained with VLT/CRIRES for 20 MYSOs, selected from the RMS Survey. The first overtone emission was modelled under the assumption that it originates in a circumstellar disc in Keplerian rotation. Three models of the physical disc structure were tested, and it was determined that the only model able to reproduce the spectra adequately was an analytic description of the temperature and density within the disc.

All spectra were well fit by this model of a Keplerian rotation disc. The best fitting disc parameters were consistent with previously published information, where

information was available. The inclinations of the discs were spread across a wide range of angles, with an average corresponding to a random selection. The best fitting temperature and density exponents were consistent with flat circumstellar discs, with some scatter, and a handful of objects had exponents consistent with flared, irradiated discs. Essentially all best fitting discs are located close to, or within, the dust sublimation radius. This suggests that this emission occurs from gaseous circumstellar matter around the MYSOs. Finally, it is demonstrated that the objects in the sample appear to not differ from general population of the RMS Survey database, based on their near- and mid-infrared colours. The combination of a large sample of MYSOs and fits obtained with detailed models provide compelling evidence for the presence of small scale gaseous accretion discs around such objects, supporting the scenario in which massive stars form in a similar way to low mass stars, via disc accretion.

Determining accretion rates in Herbig Ae & Be stars

Herbig Ae & Be stars (HAeBes) are the precursors to intermediate mass stars, with masses between 2 and $8 M_{\odot}$. HAeBes are often obscured, but are still visible at optical wavelengths, unlike their higher mass equivalents, MYSOs. Therefore, the study of HAeBe stars offers a unique insight into the formation mechanisms of stars more massive than our Sun. Over the mass range of the HAeBes, the interiors of the stars change from being convective to being radiative, and thus they do not possess the dynamos needed to power strong magnetic fields. Therefore, the accretion mechanism is thought to change from magnetospheric to some other form of accretion, possibly directly on to the stellar surface. Thus, the study of the accretion mechanisms of HAeBes will enable characterisation of this change.

Near infrared spectroscopy can be used to probe the accretion characteristics of young stars. The strength of the $n = 7-4$ transition of atomic hydrogen, Br γ , has been shown in previous studies (Calvet *et al.*, 2004; Garcia Lopez *et al.*, 2006; Mendigutía *et al.*, 2011; Muzerolle *et al.*, 1998) to correlate with the accretion luminosity of YSOs as determined from infrared or UV continuum excess. CO first overtone bandhead emission has been shown to originate from the discs around young stars, and can be modelled using physical disc models, allowing the accretion rate to be determined.

Five Herbig Ae & Be stars with CO first overtone emission were selected from an original sample of 90 observed by VLT/X-SHOOTER, in order to measure the strength of the Br γ emission and model the CO emission to determine accretion rates for the objects, and to discover if the accretion rates determined by each method were consistent with one another. The equivalent widths of the Br γ emission lines were measured and converted into accretion rates using the calibrations determined from previous work (Garcia Lopez *et al.*, 2006; Mendigutía *et al.*, 2011). The CO bandheads were fit using the methods described in Chapter 3. Two models describing the physical disc structure were tested on the clearest CO spectrum, and it was determined that a physical model based on balancing the heating and cooling within the disc (as in Carr 1989 and Chandler *et al.* 1995) most accurately reproduced the X-SHOOTER data. This model was then used to fit the other HAeBe CO spectra, deriving disc sizes, inclinations, mass accretion rates and intrinsic linewidths of the CO emitting gas.

Comparison of the mass accretion rates obtained from the CO and the Br γ showed that the CO fitting does not constrain the mass accretion rate well for data

of this quality and spectral resolution. High resolution VLT/CRIRES archive data for one object was presented, and compared to the lower resolution X-SHOOTER spectra. The CRIRES data showed many spectral features that are not seen in the X-SHOOTER spectra. The high resolution spectrum was fit with the two disc models mentioned previously. The model based on heating and cooling was unable to reproduce the features in the spectrum, while the previously discarded analytic model had the freedom to produce a good fit to the data. It was concluded that high resolution data are required to perform the CO fitting in this way. Therefore, previous results obtained from fitting CO bandheads using this method of describing the disc should be treated with caution, until further high resolution follow-up observations can be performed and analysed.

5.2 Future work

Despite the state of the art modelling and observations that have been performed in recent years, there are still many unexplored avenues of research in the field of circumstellar discs and young stellar objects. This section outlines further steps that could be taken to develop the work presented in this thesis, and the outlook for the field as a whole.

Chemistry in circumstellar discs

Spiral structure has been detected in the discs of SAO 206462 (HD 135344B, Muto *et al.* 2012) and AB Aurigae (Fukagawa *et al.*, 2004). However, these objects possess relatively evolved transitional discs, and the structures are seen in longer wavelength regimes, more associated with dust emission. Imaging of spiral arms

in gaseous disc material has yet to be performed. The advent of ALMA will allow previously unresolvable scales to be accessed. With this facility nearing full capacity, the opportunity for observations such as these is fast approaching. Promising targets for such imaging include a Class 0 source, NGC 1333 IRAS 4A, shown to have a 130 AU disc from NH_3 observations using the Jansky Very Large Array (JVLA, Choi *et al.* 2007); and IRAS 16293-2422 A and B, which have been observed in ALMA science verification (Pineda *et al.*, 2012).

Therefore, the chemical results presented here have been used in radiative transfer calculations to determine the observability of this model disc in different submillimetre line transitions (Douglas *et al.*, 2013). The Common Astronomy Software package (CASA) was used to produce synthetic ALMA observations of the disc under the assumption that it is surrounded by a pre-stellar core. It has been found that transitions of CO, HCO^+ , OCS and H_2CO will allow measurements of the disc structure, and can be used to probe the kinematics of the disc on all scales. Figure 5.1 shows the synthetic observations of transitions of H_2CO and HCO^+ .

It was also found that spiral structure signatures can be resolved in position-velocity diagrams of the disc, even when the disc is close to edge-on. In the future, we hope to use the resolving power of fully-operational ALMA in order to image such discs, which will allow constraints to be placed on physical and chemical models of these environments.

Improvements to the methods presented here could also be made. For instance, the reaction network used in this work is, by comparison to other models, rather small. The implementation of a larger reaction network involving more chemical

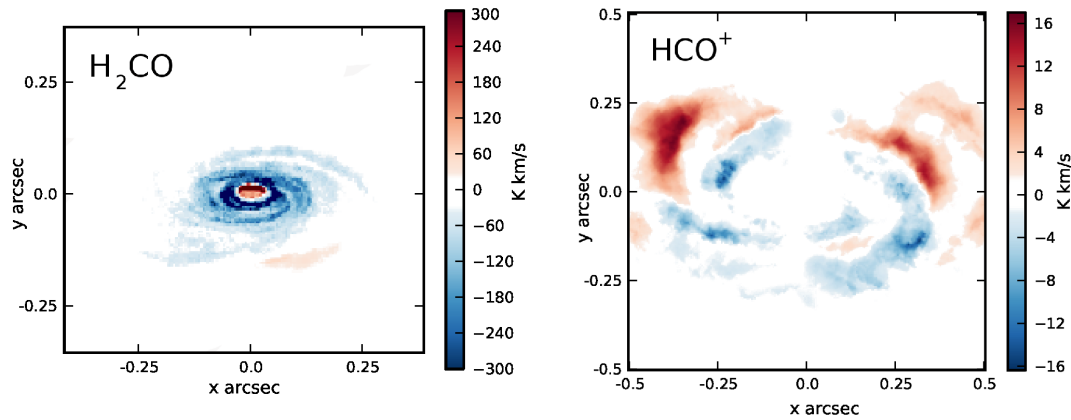


Figure 5.1: Synthetic, continuum subtracted, integrated intensity maps of the disc presented in Chapter 2 for transitions of H_2CO and HCO^+ , as would be viewed with fully operational ALMA. Courtesy of Tom Douglas (Douglas *et al.*, 2013)

species and elements would be straightforward, but would increase the time required to compute the chemical histories. To compensate for this, the number of fluid elements that are followed could be reduced. However, testing would need to be performed to determine the minimum number of fluid elements necessary before the chemistry is not sampled well enough across the disc, and in particular across shock regions.

In this disc model, the chemistry and physical simulation are decoupled. It has been shown in recent coupled models of protoplanetary discs that the effect of the chemistry on the the physical evolution of the disc material can be significant. Molecules such as CO and H_2O contribute to the cooling of the disc material, and large molecules such as polycyclic aromatic hydrocarbons (PAHs) can contribute significantly to the heating of the disc material (Tilling *et al.*, 2012; Woitke *et al.*, 2009a). In order to achieve this coupling in the model presented here, the chemistry of the species key for the thermal structure would need to be calculated alongside the physical disc simulation, which could be included in future modelling efforts.

Discs around MYSOs

As discussed previously, direct evidence of discs around massive young stellar objects is difficult to obtain for all but a handful of cases, so indirect methods of probing the circumstellar environment of MYSOs are extremely useful. An obvious next step to the work presented here is the observation of more MYSO targets in the southern hemisphere with CO emission, using VLT/CRIRES in other semesters, in order to increase the number of objects in the sample. The SUBARU/IRCS instrument ($R \sim 20\,000$, Tokunaga *et al.* 1998) may be able to resolve the kinematic structure within the CO bandheads for MYSOs in the northern hemisphere.

Currently, the model of the disc used in the work is considered to be infinitely thin. This may not be appropriate for discs around massive stars, and could be extended to include vertical structure. Discs with a non-negligible vertical extent may have upper regions that absorb enough stellar radiation to become hot enough to excite CO at radii where collisional heating cannot produce the required excitation temperatures. Including this structure in the modelling may allow further information on the circumstellar environment of the MYSOs to be obtained.

The method of fitting CO bandheads presented here has been utilised in further studies of MYSOs involving integral field spectroscopy (Murakawa *et al.*, submitted) and also in a study of a lower mass young star (Garatti *et al.*, 2013), demonstrating the applicability of the technique to young stars across the entire mass range.

Mass accretion in HAeBes

The study of Herbig Ae & Be stars provides much information about the formation mechanisms of higher mass stars, as it is across this mass range that the accretion mechanism is thought to switch from magnetospheric accretion to another form of accretion. The large sample of approximately 90 HAeBes observed with X-SHOOTER provides a wealth of data across a large wavelength range that has yet to be completely explored. Other accretion indicators, such as the Paschen β transitions, and UV and IR excesses, could be characterised from this dataset. However, preliminary analysis has shown that this is difficult for the hotter, more massive Be stars. Therefore, there is clearly a need for other indicators of accretion in these objects.

The work presented here has shown that higher spectral resolution observations are needed to properly resolve the kinematic structure of the CO bandheads, to enable fitting models as was done with the MYSOs. The VLT/CRIRES instrument has been shown to be able to provide such high resolution spectra, therefore a proposal will be submitted to observe the other HAeBe targets with CO emission in our sample using CRIRES, so that their CO emission can be properly modelled using other descriptions of accretion discs.

There is not currently an explanation for why some YSOs exhibit CO first overtone emission, and why others do not. VLTI/AMBER and VLT/CRIRES observations were used in Wheelwright *et al.* (2012c) to spatially resolve the CO emission region around the binary supergiant B[e] star HD 327083, and showed that the emission originated in a circumbinary disc. It is possible that observations such as this could be used to resolve the CO emission regions around MYSOs and

HAeBes. More precise measurements of the source of the CO emission may enable us to determine why CO is not detected across all YSOs.

5.3 Final remarks

The study of circumstellar discs offers a useful opportunity to study how star and planet formation occurs, and under what conditions these processes take place. The field is approaching an exciting period of time. In the short term, the completion of a fully operational ALMA will revolutionise our understanding using submillimetre observations. In the longer term, facilities such as the proposed European Extremely Large Telescope (E-ELT) will prove equally as revolutionary for optical and near-infrared observations.

This thesis has shown that the relationship between physics and chemistry can be used to gain a better understanding of astrophysical environments. Knowledge of the chemistry occurring within circumstellar discs can be used to determine species that are useful tracers of physical processes in the discs, and observations of such chemical species can be used to determine the physical parameters of the discs themselves.

Bibliography

- AIKAWA, Y., MIYAMA, S.M., NAKANO, T. & UMEBAYASHI, T. (1996). Evolution of Molecular Abundance in Gaseous Disks around Young Stars: Depletion of CO Molecules. *ApJ*, **467**, 684. 27
- AIKAWA, Y., UMEBAYASHI, T., NAKANO, T. & MIYAMA, S.M. (1999). Evolution of Molecular Abundances in Protoplanetary Disks with Accretion Flow. *ApJ*, **519**, 705–725. 27, 28
- AIKAWA, Y., VAN ZADELHOFF, G.J., VAN DISHOECK, E.F. & HERBST, E. (2002). Warm molecular layers in protoplanetary disks. *A&A*, **386**, 622–632. 27
- ANDRE, P., WARD-THOMPSON, D. & BARSONY, M. (1993). Submillimeter continuum observations of Rho Ophiuchi A - The candidate protostar VLA 1623 and prestellar clumps. *ApJ*, **406**, 122–141. 5, 6
- ARMITAGE, P.J. (2011). Dynamics of Protoplanetary Disks. *ARA&A*, **49**, 195–236. 15
- ARMITAGE, P.J., LIVIO, M. & PRINGLE, J.E. (2001). Episodic accretion in magnetically layered protoplanetary discs. *MNRAS*, **324**, 705–711. 29

- ARONS, J. & MAX, C.E. (1975). Hydromagnetic Waves in Molecular Clouds. *ApJ*, **196**, L77. 4
- BALBUS, S.A. (2003a). Enhanced Angular Momentum Transport in Accretion Disks. *ARA&A*, **41**, 555–597. 12
- BALBUS, S.A. (2003b). Enhanced Angular Momentum Transport in Accretion Disks. *ARA&A*, **41**, 555–597. 15
- BALBUS, S.A. & HAWLEY, J.F. (1991). A powerful local shear instability in weakly magnetized disks. I - Linear analysis. II - Nonlinear evolution. *ApJ*, **376**, 214–233. 14
- BERGIN, E., CALVET, N., D’ALESSIO, P. & HERCZEG, G.J. (2003). The Effects of UV Continuum and Ly α Radiation on the Chemical Equilibrium of T Tauri Disks. *ApJ*, **591**, L159–L162. 27
- BERTHOUD, M.G. (2008). *Carbon monoxide emission from the inner disk around intermediate-mass stars*. Ph.D. thesis, Cornell University. 64
- BERTHOUD, M.G., KELLER, L.D., HERTER, T.L., RICHTER, M.J. & WHELAN, D.G. (2007). Near-IR CO Overtone Emission in 51 Ophiuchi. *ApJ*, **660**, 461–468. 67
- BEUTHER, H., LINZ, H. & HENNING, T. (2012). The high-mass disk candidates NGC 7538IRS1 and NGC 7538S. *A&A*, **543**, A88. 104
- BIK, A. & THI, W.F. (2004). Evidence for an inner molecular disk around massive Young Stellar Objects. *A&A*, **427**, L13–L16. 62, 67, 87, 99, 100

- BIK, A., KAPER, L. & WATERS, L.B.F.M. (2006). VLT K-band spectroscopy of massive young stellar objects in (ultra-)compact HII regions. *A&A*, **455**, 561–576. 74, 85, 100
- BLUM, R.D., BARBOSA, C.L., DAMINELI, A., CONTI, P.S. & RIDGWAY, S. (2004). Accretion Signatures from Massive Young Stellar Objects. *ApJ*, **617**, 1167–1176. 62
- BODENHEIMER, P. (1995). Angular Momentum Evolution of Young Stars and Disks. *ARA&A*, **33**, 199–238. 12, 15
- BOLEY, A.C. (2007). *The three-dimensional behavior of spiral shocks in protoplanetary disks*. Ph.D. thesis, Indiana University. 30
- BOLEY, A.C. (2009). The Two Modes of Gas Giant Planet Formation. *ApJ*, **695**, L53–L57. 13, 28, 30, 31
- BOLEY, A.C. & DURISEN, R.H. (2008). Gravitational Instabilities, Chondrule Formation, and the FU Orionis Phenomenon. *ApJ*, **685**, 1193–1209. 30, 31, 33, 36
- BOLEY, A.C. & DURISEN, R.H. (2010). On the Possibility of Enrichment and Differentiation in Gas Giants During Birth by Disk Instability. *ApJ*, **724**, 618–639. 29
- BOLEY, A.C., MEJÍA, A.C., DURISEN, R.H. *et al.* (2006). The Thermal Regulation of Gravitational Instabilities in Protoplanetary Disks. III. Simulations with Radiative Cooling and Realistic Opacities. *ApJ*, **651**, 517–534. 29

- BOLEY, A.C., DURISEN, R.H., NORDLUND, Å. & LORD, J. (2007a). Three-Dimensional Radiative Hydrodynamics for Disk Stability Simulations: A Proposed Testing Standard and New Results. *ApJ*, **665**, 1254–1267. 29
- BOLEY, A.C., HARTQUIST, T.W., DURISEN, R.H. & MICHAEL, S. (2007b). The Internal Energy for Molecular Hydrogen in Gravitationally Unstable Protoplanetary Disks. *ApJ*, **656**, L89–L92. 31
- BOLEY, A.C., HAYFIELD, T., MAYER, L. & DURISEN, R.H. (2010). Clumps in the outer disk by disk instability: Why they are initially gas giants and the legacy of disruption. *Icarus*, **207**, 509–516. 29
- BOLEY, P., LINZ, H., VAN BOEKEL, R. *et al.* (2012). On the massive young stellar object AFGL4176: High-spatial-resolution multi-wavelength observations and modeling. *ArXiv e-prints*. 98
- BOSS, A.P. (2001). Gas Giant Protoplanet Formation: Disk Instability Models with Thermodynamics and Radiative Transfer. *ApJ*, **563**, 367–373. 29
- BOSS, A.P. (2007). Testing Disk Instability Models for Giant Planet Formation. *ApJ*, **661**, L73–L76. 29
- BOUVIER, J., ALENCAR, S.H.P., HARRIES, T.J., JOHNS-KRULL, C.M. & ROMANOVA, M.M. (2007). Magnetospheric Accretion in Classical T Tauri Stars. *Protostars and Planets V*, 479–494. 107
- BRAND, J. & BLITZ, L. (1993). The Velocity Field of the Outer Galaxy. *A&A*, **275**, 67. 74

- BRONFMAN, L., NYMAN, L.A. & MAY, J. (1996). A CS(2-1) survey of IRAS point sources with color characteristics of ultra-compact HII regions. *A&AS*, **115**, 81. 74
- BROWN, P.N., BYRNE, G.D. & HINDMARSH, A.C. (1989). Vode: A variable-coefficient ode solver. *SIAM Journal on Scientific and Statistical Computing*, **10**, 1038–1051. 39
- CAI, K., PICKETT, M.K., DURISEN, R.H. & MILNE, A.M. (2010). Giant Planet Formation by Disk Instability: A Comparison Simulation with an Improved Radiative Scheme. *ApJ*, **716**, L176–L180. 29
- CALVET, N., MUZEROLLE, J., BRICEÑO, C. *et al.* (2004). The Mass Accretion Rates of Intermediate-Mass T Tauri Stars. *AJ*, **128**, 1294–1318. 108, 116, 145
- CARR, J.S. (1989). Near-infrared CO emission in young stellar objects. *ApJ*, **345**, 522–535. 24, 62, 67, 69, 92, 120, 132, 137, 139, 145
- CARRASCO-GONZÁLEZ, C., GALVÁN-MADRID, R., ANGLADA, G. *et al.* (2012). Resolving the Circumstellar Disk around the Massive Protostar Driving the HH 80-81 Jet. *ApJ*, **752**, L29. 61
- CASELLI, P. (2005). Chemical Processes in Star Forming Regions. In M.S.N. Kumar, M. Tafalla & P. Caselli, eds., *Cores to Clusters: Star Formation with Next Generation Telescopes*, 47. 18
- CHANDLER, C.J., CARLSTROM, J.E. & SCOVILLE, N.Z. (1995). Infrared CO Emission from Young Stars: Accretion Disks and Neutral Winds. *ApJ*, **446**, 793. 24, 62, 67, 69, 92, 120, 138, 139, 145

CHANDRASEKHAR, S. (1960). The Stability of Non-Dissipative Couette Flow in Hydromagnetics. *Proceedings of the National Academy of Science*, **46**, 253–257.

14

CHIANG, E.I. & GOLDREICH, P. (1997). Spectral Energy Distributions of T Tauri Stars with Passive Circumstellar Disks. *ApJ*, **490**, 368. 88, 97, 98

CHINI, R. & NECKEL, T. (1981). UBV and H-beta observations of stars towards M8. *A&A*, **102**, 171–174. 74

CHOI, M., TATEMATSU, K., PARK, G. & KANG, M. (2007). Ammonia Imaging of the Disks in the NGC 1333 IRAS 4A Protobinary System. *ApJ*, **667**, L183–L186. 147

CLARKE, A. J. (2007). *Near-infrared studies of massive young stellar objects*. Ph.D. thesis, University of Leeds. 63

COOPER, H.D.B., LUMSDEN, S.L., OUDMAIJER, R.D. *et al.* (2013). The RMS survey: near-IR spectroscopy of massive young stellar objects. *MNRAS*, **430**, 1125–1157. 63, 132

COSSINS, P., LODATO, G. & CLARKE, C.J. (2009). Characterizing the gravitational instability in cooling accretion discs. *MNRAS*, **393**, 1157–1173. 29

COVEY, K.R., HILLENBRAND, L.A., MILLER, A.A. *et al.* (2011). PTF10nvg: An Outbursting Class I Protostar in the Pelican/North American Nebula. *AJ*, **141**, 40. 85

- COWLEY, C.R., HUBRIG, S., CASTELLI, F. & WOLFF, B. (2012). The narrow, inner CO ring around the magnetic Herbig Ae star HD 101412. *A&A*, **537**, L6. 134, 136, 137
- D’ALESSIO, P., CALVET, N., HARTMANN, L., LIZANO, S. & CANTÓ, J. (1999). Accretion Disks around Young Objects. II. Tests of Well-mixed Models with ISM Dust. *ApJ*, **527**, 893–909. 108
- D’ALESSIO, P., CALVET, N. & HARTMANN, L. (2001). Accretion Disks around Young Objects. III. Grain Growth. *ApJ*, **553**, 321–334. 108
- DAVIES, B., LUMSDEN, S.L., HOARE, M.G., OUDMAIJER, R.D. & DE WIT, W.J. (2010). The circumstellar disc, envelope and bipolar outflow of the massive young stellar object W33A. *MNRAS*, **402**, 1504–1515. 62
- DE WIT, W.J., HOARE, M.G., OUDMAIJER, R.D. & LUMSDEN, S.L. (2010). The origin of mid-infrared emission in massive young stellar objects: multi-baseline VLTI observations of W33A. *A&A*, **515**, A45. 77, 80, 82
- DE ZEEUW, P.T., HOOGERWERF, R., DE BRUIJNE, J.H.J., BROWN, A.G.A. & BLAAUW, A. (1999). A HIPPARCOS Census of the Nearby OB Associations. *AJ*, **117**, 354–399. 110
- DOUGLAS, T.A., CASELLI, P., ILEE, J.D. *et al.* (2013). Simulated Observations of Young Gravitationally Unstable Protoplanetary Discs. *ArXiv e-prints*. 59, 147, 148
- DREW, J.E., BUSFIELD, G., HOARE, M.G. *et al.* (1997). MWC 297, B1.5Ve: a zero-age main-sequence star in the Aquila Rift. *MNRAS*, **286**, 538–548. 110

- DULLEMOND, C.P., HOLLENBACH, D., KAMP, I. & D'ALESSIO, P. (2007). Models of the Structure and Evolution of Protoplanetary Disks. *Protostars and Planets V*, 555–572. 15
- DURISEN, R.H., BOSS, A.P., MAYER, L. *et al.* (2007). Gravitational Instabilities in Gaseous Protoplanetary Disks and Implications for Giant Planet Formation. *Protostars and Planets V*, 607–622. 29, 31
- DUTREY, A., HENNING, T., GUILLOTEAU, S. *et al.* (2007). Chemistry in disks. I. Deep search for N₂H⁺ in the protoplanetary disks around LkCa 15, MWC 480, and DM Tauri. *A&A*, **464**, 615–623. 27, 141
- EGAN, M.P., PRICE, S.D. & KRAEMER, K.E. (2003). The Midcourse Space Experiment Point Source Catalog Version 2.3. In *AAS Meeting Abstracts*, vol. 35 of *Bulletin of the AAS*, 1301. 9
- EHRENFREUND, P. & CHARNLEY, S.B. (2000). Organic Molecules in the Interstellar Medium, Comets, and Meteorites: A Voyage from Dark Clouds to the Early Earth. *ARA&A*, **38**, 427–483. 42, 43
- EHRENFREUND, P. & SCHUTTE, W.A. (2000). ISO Observations of Interstellar Ices: Implications for the Pristinity of Comets. *Advances in Space Research*, **25**, 2177–2188. 43
- ELLERBROEK, L.E., KAPER, L., BIK, A. *et al.* (2011). The Intermediate-mass Young Stellar Object 08576nr292: Discovery of A Disk-Jet System. *ApJ*, **732**, L9. 99, 100

FALGARONE, E. & PHILLIPS, T.G. (1990). A signature of the intermittency of interstellar turbulence - The wings of molecular line profiles. *ApJ*, **359**, 344–354.

4

FARRENQ, R., GUELACHVILI, G., SAUVAL, A.J., GREVESSE, N. & FARMER, C.B. (1991). Improved Dunham coefficients for CO from infrared solar lines of high rotational excitation. *Journal of Molecular Spectroscopy*, **149**, 375–390. 63

FEDELE, D., VAN DEN ANCKER, M.E., ACKE, B. *et al.* (2008). The structure of the protoplanetary disk surrounding three young intermediate mass stars. II. Spatially resolved dust and gas distribution. *A&A*, **491**, 809–820. 134

FERGUSON, J.W., ALEXANDER, D.R., ALLARD, F. *et al.* (2005). Low-Temperature Opacities. *ApJ*, **623**, 585–596. 71

FOGEL, J.K.J., BETHELL, T.J., BERGIN, E.A., CALVET, N. & SEMENOV, D. (2011). Chemistry of a Protoplanetary Disk with Grain Settling and Ly α Radiation. *ApJ*, **726**, 29. 27, 142

FUKAGAWA, M., HAYASHI, M., TAMURA, M. *et al.* (2004). Spiral Structure in the Circumstellar Disk around AB Aurigae. *ApJ*, **605**, L53–L56. 146

GAMMIE, C.F. (1996). Layered Accretion in T Tauri Disks. *ApJ*, **457**, 355. 29

GAMMIE, C.F. (2001). Nonlinear Outcome of Gravitational Instability in Cooling, Gaseous Disks. *ApJ*, **553**, 174–183. 29

GARATTI, A.C.O., GARCIA LOPEZ, R., WEIGELT, G. *et al.* (2013). LBT/LUCIFER near-infrared spectroscopy of PV Cephei. An outbursting young stellar object with an asymmetric jet. *ArXiv e-prints*. 149

- GARCIA LOPEZ, R., NATTA, A., TESTI, L. & HABART, E. (2006). Accretion rates in Herbig Ae stars. *A&A*, **459**, 837–842. 109, 116, 117, 138, 145
- GORTI, U. & HOLLENBACH, D. (2004). Models of Chemistry, Thermal Balance, and Infrared Spectra from Intermediate-Aged Disks around G and K Stars. *ApJ*, **613**, 424–447. 28
- GUILLOTEAU, S. & DUTREY, A. (2008). A new view of proto-planetary disks with ALMA. *Ap&SS*, **313**, 95–100. 27
- GUIMARÃES, M.M., ALENCAR, S.H.P., CORRADI, W.J.B. & VIEIRA, S.L.A. (2006). Stellar parameters and evidence of circumstellar activity for a sample of Herbig Ae/Be stars. *A&A*, **457**, 581–589. 110
- HARTQUIST, T.W. & DALGARNO, A. (1996). Molecular Diagnostics of the Interstellar Medium and Star Forming Regions. *Ap&SS*, **237**, 267–298. 20
- HASEGAWA, T.I., HERBST, E. & LEUNG, C.M. (1992). Models of gas-grain chemistry in dense interstellar clouds with complex organic molecules. *ApJS*, **82**, 167–195. 42
- HEINZELLER, D., NOMURA, H., WALSH, C. & MILLAR, T.J. (2011). Chemical Evolution of Protoplanetary Disks The Effects of Viscous Accretion, Turbulent Mixing, and Disk Winds. *ApJ*, **731**, 115. 28, 59, 142
- HENNING, T., SEMENOV, D., GUILLOTEAU, S. *et al.* (2010). Chemistry in Disks. III. Photochemistry and X-ray Driven Chemistry Probed by the Ethynyl Radical (CCH) in DM Tau, LkCa 15, and MWC 480. *ApJ*, **714**, 1511–1520. 27, 41, 141

- HERBIG, G.H. (1960). The Spectra of Be- and Ae-TYPE Stars Associated with Nebulosity. *ApJS*, **4**, 337. 10
- HERBST, E. & VAN DISHOECK, E.F. (2009). Complex Organic Interstellar Molecules. *ARA&A*, **47**, 427–480. 19
- HERPIN, F., CHAVARRÍA, L., VAN DER TAK, F. *et al.* (2012). The massive protostar W43-MM1 as seen by Herschel-HIFI water spectra: high turbulence and accretion luminosity. *A&A*, **542**, A76. 104
- HOLLENBACH, D., KAUFMAN, M.J., BERGIN, E.A. & MELNICK, G.J. (2009). Water, O₂, and Ice in Molecular Clouds. *ApJ*, **690**, 1497–1521. 42
- HOSOKAWA, T. & OMUKAI, K. (2009). Evolution of Massive Protostars with High Accretion Rates. *ApJ*, **691**, 823–846. 80, 104, 108
- HOSOKAWA, T., YORKE, H.W. & OMUKAI, K. (2010). Evolution of Massive Protostars Via Disk Accretion. *ApJ*, **721**, 478–492. 104
- HUBRIG, S., SCHÖLLER, M., SAVANOV, I. *et al.* (2009). Magnetic survey of emission line B-type stars with FORS 1 at the VLT. *Astronomische Nachrichten*, **330**, 708. 107
- HUMPHREYS, R.M. & LOCKWOOD, G.W. (1972). Spectroscopic and Photometric Changes in the Peculiar Infrared Star VX Sagittarius. *ApJ*, **172**, L59. 19
- ILGNER, M., HENNING, T., MARKWICK, A.J. & MILLAR, T.J. (2004). Transport processes and chemical evolution in steady accretion disk flows. *A&A*, **415**, 643–659. 28, 54, 59

- JEANS, J.H. (1902). The Stability of a Spherical Nebula. *Royal Society of London Philosophical Transactions Series A*, **199**, 1–53. 3
- JIMÉNEZ-SERRA, I., MARTÍN-PINTADO, J., RODRÍGUEZ-FRANCO, A. *et al.* (2007). A Photoevaporating Rotating Disk in the Cepheus A HW2 Star Cluster. *ApJ*, **661**, L187–L190. 61
- JONKHEID, B.J. (2006). *Chemistry in evolving protoplanetary disks*. Ph.D. thesis, Leiden Observatory, Leiden University, P.O. Box 9513, 2300 RA Leiden, The Netherlands. 6
- KAEUFL, H.U., BALLESTER, P., BIEREICHEL, P. *et al.* (2004). CRIRES: a high-resolution infrared spectrograph for ESO’s VLT. In A.F.M. Moorwood & M. Iye, eds., *SPIE Conference Series*, vol. 5492 of *SPIE Conference Series*, 1218–1227. 72
- KAHN, F.D. (1974). Cocoons around early-type stars. *A&A*, **37**, 149–162. 9
- KAZES, I. & CRUTCHER, R.M. (1986). Measurement of magnetic-field strengths in molecular clouds Detection of OH-line Zeeman splitting. *A&A*, **164**, 328–336. 3
- KLAASSEN, P.D., WILSON, C.D., KETO, E.R. *et al.* (2011). High resolution CO observation of massive star forming regions. *A&A*, **530**, A53. 9
- KRAUS, M., KRÜGEL, E., THUM, C. & GEBALLE, T.R. (2000). CO band emission from MWC 349. I. First overtone bands from a disk or from a wind? *A&A*, **362**, 158–168. 63, 73

- KRAUS, S., HOFMANN, K.H., MENTEN, K.M. *et al.* (2010). A hot compact dust disk around a massive young stellar object. *Nature*, **466**, 339–342. 61, 98, 104
- KRUMHOLZ, M.R., KLEIN, R.I. & MCKEE, C.F. (2007). Molecular Line Emission from Massive Protostellar Disks: Predictions for ALMA and EVLA. *ApJ*, **665**, 478–491. 96
- KRUMHOLZ, M.R., KLEIN, R.I., MCKEE, C.F., OFFNER, S.S.R. & CUNNINGHAM, A.J. (2009). The Formation of Massive Star Systems by Accretion. *Science*, **323**, 754–. 9
- KUIPER, R., KLAHR, H., BEUTHER, H. & HENNING, T. (2010). Circumventing the Radiation Pressure Barrier in the Formation of Massive Stars via Disk Accretion. *ApJ*, **722**, 1556–1576. 9
- KUIPER, R., KLAHR, H., BEUTHER, H. & HENNING, T. (2011). Three-dimensional Simulation of Massive Star Formation in the Disk Accretion Scenario. *ApJ*, **732**, 20. 9, 96, 104
- LADA, C.J. (1987). Star formation - From OB associations to protostars. In M. Peimbert & J. Jugaku, eds., *Star Forming Regions*, vol. 115 of *IAU Symposium*, 1–17. 5
- LARSON, R.B. & STARRFIELD, S. (1971). On the formation of massive stars and the upper limit of stellar masses. *A&A*, **13**, 190–197. 9
- LEPP, S. & STANCIL, P.C. (1998). Molecules in the Early Universe and Primordial Structure Formation. *The Molecular Astrophysics of Stars and Galaxies*,

edited by Thomas W. Hartquist and David A. Williams. Clarendon Press, Oxford, 1998., p.37, 4, 37. 18

LINZ, H., HENNING, T., FELDT, M. *et al.* (2009). Mid-infrared interferometry of massive young stellar objects. I. VLTI and Subaru observations of the enigmatic object M8E-IR. *A&A*, **505**, 655–661. 85, 101

LODATO, G. (2008). Classical disc physics. *New Astronomy Reviews*, **52**, 21–41. 14, 15

LODATO, G. & CLARKE, C.J. (2011). Resolution requirements for smoothed particle hydrodynamics simulations of self-gravitating accretion discs. *MNRAS*, **413**, 2735–2740. 29

LODATO, G. & RICE, W.K.M. (2004). Testing the locality of transport in self-gravitating accretion discs. *MNRAS*, **351**, 630–642. 29

LUMSDEN, S.L., HOARE, M.G., OUDMAIJER, R.D. & RICHARDS, D. (2002). The population of the Galactic plane as seen by MSX. *MNRAS*, **336**, 621–636. 9

MANOJ, P., BHATT, H.C., MAHESWAR, G. & MUNEER, S. (2006). Evolution of Emission-Line Activity in Intermediate-Mass Young Stars. *ApJ*, **653**, 657–674. 110

MARKWICK, A.J., ILGNER, M., MILLAR, T.J. & HENNING, T. (2002). Molecular distributions in the inner regions of protostellar disks. *A&A*, **385**, 632–646. 28

- MARTIN, S.C. (1997). A Funnel Flow Origin for CO Bandhead Emission in Young Stellar Objects. *ApJ*, **478**, L33. 102
- MARTINS, F., SCHAERER, D. & HILLIER, D.J. (2005). A new calibration of stellar parameters of Galactic O stars. *A&A*, **436**, 1049–1065. 76, 85
- MAYER, L., QUINN, T., WADSLEY, J. & STADEL, J. (2004). The Evolution of Gravitationally Unstable Protoplanetary Disks: Fragmentation and Possible Giant Planet Formation. *ApJ*, **609**, 1045–1064. 29
- MAYER, L., LUFKIN, G., QUINN, T. & WADSLEY, J. (2007). Fragmentation of Gravitationally Unstable Gaseous Protoplanetary Disks with Radiative Transfer. *ApJ*, **661**, L77–L80. 29
- MCÉLROY, D., WALSH, C., MARKWICK, A.J. *et al.* (2013). The UMIST database for astrochemistry 2012. *A&A*, **550**, A36. 16
- MEJÍA, A.C., DURISEN, R.H., PICKETT, M.K. & CAI, K. (2005). The Thermal Regulation of Gravitational Instabilities in Protoplanetary Disks. II. Extended Simulations with Varied Cooling Rates. *ApJ*, **619**, 1098–1113. 29
- MENDIGUTÍA, I., CALVET, N., MONTESINOS, B. *et al.* (2011). Accretion rates and accretion tracers of Herbig Ae/Be stars. *A&A*, **535**, A99. 109, 117, 138, 145
- MERÍN, B., MONTESINOS, B., EIROA, C. *et al.* (2004). Study of the properties and spectral energy distributions of the Herbig AeBe stars HD 34282 and HD 141569. *A&A*, **419**, 301–318. 120
- MERU, F. & BATE, M.R. (2011). Non-convergence of the critical cooling timescale for fragmentation of self-gravitating discs. *MNRAS*, **411**, L1–L5. 29

- MESTEL, L. & SPITZER, L., JR. (1956). Star formation in magnetic dust clouds. *MNRAS*, **116**, 503. 3
- MICHAEL, S., DURISEN, R.H. & BOLEY, A.C. (2011). Migration of Gas Giant Planets in Gravitationally Unstable Disks. *ApJ*, **737**, L42. 29
- MILLAR, T.J., FARQUHAR, P.R.A. & WILLACY, K. (1997a). The UMIST Database for Astrochemistry 1995. *A&AS*, **121**, 139–185. 16
- MILLAR, T.J., FARQUHAR, P.R.A. & WILLACY, K. (1997b). The UMIST Database for Astrochemistry 1995. *A&AS*, **121**, 139–185. 36, 40
- MOLINARI, S., BRAND, J., CESARONI, R. & PALLA, F. (1996). A search for precursors of ultracompact HII regions in a sample of luminous IRAS sources. I. Association with ammonia cores. *A&A*, **308**, 573–587. 9
- MONNIER, J.D. & MILLAN-GABET, R. (2002). On the Interferometric Sizes of Young Stellar Objects. *ApJ*, **579**, 694–698. 90
- MOTTRAM, J.C., VINK, J.S., OUDMAIJER, R.D. & PATEL, M. (2007). On the difference between Herbig Ae and Herbig Be stars. *MNRAS*, **377**, 1363–1374. 9, 10, 107
- MOTTRAM, J.C., HOARE, M.G., LUMSDEN, S.L. *et al.* (2010). The RMS survey: far-infrared photometry of young massive stars. *A&A*, **510**, A89. 10
- MOTTRAM, J.C., HOARE, M.G., DAVIES, B. *et al.* (2011). The RMS Survey: The Luminosity Functions and Timescales of Massive Young Stellar Objects and Compact H II Regions. *ApJ*, **730**, L33. 73

- MÜLLER, H., SCHLÖDER, F., STUTZKI, J. & WINNEWISSER, G. (2005). The Cologne Database for Molecular Spectroscopy. *Journal of Molecular Structure*, **742**, 215–227. 16
- MURAKAWA, K., LUMSDEN, S.L., OUDMAIJER, R.D. *et al.* (submitted). Near-infrared integral field spectroscopy of Massive Young Stellar Objects. *MNRAS*. 149
- MUTO, T., GRADY, C.A., HASHIMOTO, J. *et al.* (2012). Discovery of Small-scale Spiral Structures in the Disk of SAO 206462 (HD 135344B): Implications for the Physical State of the Disk from Spiral Density Wave Theory. *ApJ*, **748**, L22. 146
- MUZEROLLE, J., HARTMANN, L. & CALVET, N. (1998). A Br γ Probe of Disk Accretion in T Tauri Stars and Embedded Young Stellar Objects. *AJ*, **116**, 2965–2974. 108, 145
- MYERS, P.C., FULLER, G.A., MATHIEU, R.D. *et al.* (1987). Near-infrared and optical observations of IRAS sources in and near dense cores. *ApJ*, **319**, 340–357. 4
- NAJITA, J., CARR, J.S., GLASSGOLD, A.E., SHU, F.H. & TOKUNAGA, A.T. (1996). Kinematic Diagnostics of Disks around Young Stars: CO Overtone Emission from WL 16 and 1548C27. *ApJ*, **462**, 919. 24
- NOMURA, H. & MILLAR, T.J. (2005). Molecular hydrogen emission from protoplanetary disks. *A&A*, **438**, 923–938. 28

- NOMURA, H., AIKAWA, Y., NAKAGAWA, Y. & MILLAR, T.J. (2009). Effects of accretion flow on the chemical structure in the inner regions of protoplanetary disks. *A&A*, **495**, 183–188. 28
- NORBERG, P. & MAEDER, A. (2000). On the formation of massive stars by accretion. *A&A*, **359**, 1025–1034. 8
- ÖBERG, K.I., QI, C., FOGEL, J.K.J. *et al.* (2010). The Disk Imaging Survey of Chemistry with SMA. I. Taurus Protoplanetary Disk Data. *ApJ*, **720**, 480–493. 27, 141
- ÖBERG, K.I., QI, C., FOGEL, J.K.J. *et al.* (2011). Disk Imaging Survey of Chemistry with SMA. II. Southern Sky Protoplanetary Disk Data and Full Sample Statistics. *ApJ*, **734**, 98. 27, 141
- OUDMAIJER, R.D., PALACIOS, J., EIROA, C. *et al.* (2001). EXPORT: Optical photometry and polarimetry of Vega-type and pre-main sequence stars. *A&A*, **379**, 564–578. 110
- OUDMAIJER, R.D., VAN DEN ANCKER, M.E., BAINES, D. *et al.* (2011). X-shooting Herbig Ae/Be stars: Accretion probed by near-infrared He I emission. *Astronomische Nachrichten*, **332**, 238–241. 10
- PATEL, N.A., CURIEL, S., SRIDHARAN, T.K. *et al.* (2005). A disk of dust and molecular gas around a high-mass protostar. *Nature*, **437**, 109–111. 61
- PETROV, R.G., MALBET, F., WEIGELT, G. *et al.* (2007). AMBER, the near-infrared spectro-interferometric three-telescope VLTI instrument. *A&A*, **464**, 1–12. 61

- PINEDA, J.E., MAURY, A.J., FULLER, G.A. *et al.* (2012). The first ALMA view of IRAS 16293-2422. Direct detection of infall onto source B and high-resolution kinematics of source A. *A&A*, **544**, L7. 147
- PODOLAK, M., MAYER, L. & QUINN, T. (2011). Evolution of Coated Grains in Spiral Shocks of Self-gravitating Protoplanetary Disks. *ApJ*, **734**, 56. 29
- QI, C., WILNER, D.J., AIKAWA, Y., BLAKE, G.A. & HOGERHEIJDE, M.R. (2008). Resolving the Chemistry in the Disk of TW Hydrae. I. Deuterated Species. *ApJ*, **681**, 1396–1407. 27
- QIU, K., ZHANG, Q., BEUTHER, H. & FALLSCHEER, C. (2012). Forming an O Star via Disk Accretion? *ApJ*, **756**, 170. 104
- REIPURTH, B. & ZINNECKER, H. (1993). Visual binaries among pre-main sequence stars. *A&A*, **278**, 81–108. 110
- ROBITAILLE, T.P., WHITNEY, B.A., INDEBETOUW, R. & WOOD, K. (2007). Interpreting Spectral Energy Distributions from Young Stellar Objects. II. Fitting Observed SEDs Using a Large Grid of Precomputed Models. *ApJS*, **169**, 328–352. 85
- ROTHMAN, L.S., RINSLAND, C.P., GOLDMAN, A. *et al.* (1998). The HITRAN Molecular Spectroscopic Database and HAWKS (HITRAN Atmospheric Workstation): 1996 Edition. *J. Quant. Spec. Radiat. Transf.*, **60**, 665–710. 72
- SÁNCHEZ-MONGE, Á., CESARONI, R., BELTRÁN, M.T. *et al.* (2013). A candidate circumbinary Keplerian disk in G35.20-0.74 N: A study with ALMA. *A&A*, **552**, L10. 97

- SCHNEIDER, N., STUTZKI, J., WINNEWISSER, G. & BLOCK, D. (1998). The Rosette Molecular Complex. I. CO observations. *A&A*, **335**, 1049–1069. 2
- SCHREYER, K., GUILLOTEAU, S., SEMENOV, D. *et al.* (2008). Chemistry in disks. II. Poor molecular content of the AB Aurigae disk. *A&A*, **491**, 821–827. 41
- SEMENOV, D., PAVLYUCHENKOV, Y., HENNING, T., WOLF, S. & LAUNHARDT, R. (2008). Chemical and Thermal Structure of Protoplanetary Disks as Observed with ALMA. *ApJ*, **673**, L195–L198. 27
- SEMENOV, D., HERSANT, F., WAKELAM, V. *et al.* (2010). Chemistry in disks. IV. Benchmarking gas-grain chemical models with surface reactions. *A&A*, **522**, A42+. 41
- SEMENOV, D.A. (2011). Chemical Evolution of a Protoplanetary Disk. In *IAU Symposium*, vol. 280 of *IAU Symposium*, 114–126. 41
- SHAKURA, N.I. & SUNYAEV, R.A. (1973). Black holes in binary systems. Observational appearance. *A&A*, **24**, 337–355. 67, 69
- SHU, F.H., ADAMS, F.C. & LIZANO, S. (1987a). Star formation in molecular clouds - Observation and theory. *ARA&A*, **25**, 23–81. 1, 4, 6
- SHU, F.H., ADAMS, F.C. & LIZANO, S. (1987b). Star formation in molecular clouds - Observation and theory. *ARA&A*, **25**, 23–81. 4, 8
- SRIDHARAN, T.K., BEUTHER, H., SCHILKE, P., MENTEN, K.M. & WYROWSKI, F. (2002). High-Mass Protostellar Candidates. I. The Sample and Initial Results. *ApJ*, **566**, 931–944. 9

- STAMATELLOS, D., HUBBER, D.A. & WHITWORTH, A.P. (2007). Brown dwarf formation by gravitational fragmentation of massive, extended protostellar discs. *MNRAS*, **382**, L30–L34. 29
- TATULLI, E., MALBET, F., MÉNARD, F. *et al.* (2008). Spatially resolving the hot CO around the young Be star 51 Ophiuchi. *A&A*, **489**, 1151–1155. 62
- THÉ, P.S., DE WINTER, D. & PEREZ, M.R. (1994). A new catalogue of members and candidate members of the Herbig Ae/Be (HAEBE) stellar group. *A&AS*, **104**, 315–339. 10, 109
- TILLING, I., WOITKE, P., MEEUS, G. *et al.* (2012). Gas modelling in the disc of HD 163296. *A&A*, **538**, A20. 148
- TOKUNAGA, A.T., KOBAYASHI, N., BELL, J. *et al.* (1998). Infrared camera and spectrograph for the SUBARU Telescope. In A.M. Fowler, ed., *Society of Photo-Optical Instrumentation Engineers (SPIE) Conference Series*, vol. 3354 of *Society of Photo-Optical Instrumentation Engineers (SPIE) Conference Series*, 512–524. 149
- TOOMRE, A. (1964). On the gravitational stability of a disk of stars. *ApJ*, **139**, 1217–1238. 13, 29
- URQUHART, J.S., BUSFIELD, A.L., HOARE, M.G. *et al.* (2007). The RMS survey. Radio observations of candidate massive YSOs in the southern hemisphere. *A&A*, **461**, 11–23. 10

- URQUHART, J.S., HOARE, M.G., LUMSDEN, S.L. *et al.* (2009). The RMS survey. H₂O masers towards a sample of southern hemisphere massive YSO candidates and ultra compact HII regions. *A&A*, **507**, 795–802. 10
- VAIDYA, B., FENDT, C. & BEUTHER, H. (2009). Accretion Disks Around Massive Stars: Hydrodynamic Structure, Stability, and Dust Sublimation. *ApJ*, **702**, 567–579. 70
- VAN DEN ANCKER, M.E., DE WINTER, D. & TJIN A DJIE, H.R.E. (1998). HIPPARCOS photometry of Herbig Ae/Be stars. *A&A*, **330**, 145–154. 110
- VAN DISHOECK, E.F. & BLACK, J.H. (1988). The photodissociation and chemistry of interstellar CO. *ApJ*, **334**, 771–802. 87
- VAN DISHOECK, E.F. & HOGERHEIJDE, M.R. (1999). Models and Observations of the Chemistry Near Young Stellar Objects. In C.J. Lada & N.D. Kylafis, eds., *NATO ASIC Proc. 540: The Origin of Stars and Planetary Systems*, 97. 18
- VASYUNIN, A.I., WIEBE, D.S., BIRNSTIEL, T. *et al.* (2011). Impact of Grain Evolution on the Chemical Structure of Protoplanetary Disks. *ApJ*, **727**, 76. 41
- VELIKHOV, E.P. (1959). Stability of an Ideally Conducting Liquid Flowing Between Cylinders Rotating in a Magnetic Field. *J. Exptl. Theoret. Phys.*, **36**, 1398–1404. 14
- VERNET, J., DEKKER, H., D’ODORICO, S. *et al.* (2011). X-shooter, the new wide band intermediate resolution spectrograph at the ESO Very Large Telescope. *A&A*, **536**, A105. 109

- VIEIRA, S.L.A., CORRADI, W.J.B., ALENCAR, S.H.P. *et al.* (2003). Investigation of 131 Herbig Ae/Be Candidate Stars. *AJ*, **126**, 2971–2987. 10, 109, 110
- VISSER, R., VAN DISHOECK, E.F., DOTY, S.D. & DULLEMOND, C.P. (2009). The chemical history of molecules in circumstellar disks. I. Ices. *A&A*, **495**, 881–897. 42
- VOROBYOV, E.I. & BASU, S. (2005). The Origin of Episodic Accretion Bursts in the Early Stages of Star Formation. *ApJ*, **633**, L137–L140. 28
- VOROBYOV, E.I. & BASU, S. (2006). The Burst Mode of Protostellar Accretion. *ApJ*, **650**, 956–969. 28
- VOROBYOV, E.I. & BASU, S. (2009). Secular evolution of viscous and self-gravitating circumstellar discs. *MNRAS*, **393**, 822–837. 28
- VOROBYOV, E.I. & BASU, S. (2010). Formation and Survivability of Giant Planets on Wide Orbits. *ApJ*, **714**, L133–L137. 29
- WAKELAM, V., HERBST, E., LOISON, J.C. *et al.* (2012). A Kinetic Database for Astrochemistry (KIDA). *ApJS*, **199**, 21. 16, 36
- WALSH, A.J., HYLAND, A.R., ROBINSON, G. & BURTON, M.G. (1997). Studies of ultracompact HII regions - I. Methanol maser survey of IRAS-selected sources. *MNRAS*, **291**, 261–278. 74
- WALSH, C., MILLAR, T.J. & NOMURA, H. (2010). Chemical Processes in Protoplanetary Disks. *ApJ*, **722**, 1607–1623. 28, 54, 57, 142

- WHEELWRIGHT, H.E., OUDMAIJER, R.D., DE WIT, W.J. *et al.* (2010). Probing discs around massive young stellar objects with CO first overtone emission. *MNRAS*, **408**, 1840–1850. 24, 62, 63, 85, 87, 96, 97, 99, 100, 101, 105
- WHEELWRIGHT, H.E., DE WIT, W.J., OUDMAIJER, R.D. *et al.* (2012a). Probing the envelopes of massive young stellar objects with diffraction limited mid-infrared imaging. *A&A*, **540**, A89. 77, 98
- WHEELWRIGHT, H.E., DE WIT, W.J., WEIGELT, G., OUDMAIJER, R.D. & ILEE, J.D. (2012b). AMBER and CRIRES observations of the binary sgB[e] star HD 327083: evidence of a gaseous disc traced by CO bandhead emission. *A&A*, **543**, A77. 62
- WHEELWRIGHT, H.E., DE WIT, W.J., WEIGELT, G., OUDMAIJER, R.D. & ILEE, J.D. (2012c). AMBER and CRIRES observations of the binary sgB[e] star HD 327083: evidence of a gaseous disc traced by CO bandhead emission. *A&A*, **543**, A77. 150
- WILLACY, K. (2007). The Chemistry of Multiply Deuterated Molecules in Protoplanetary Disks. I. The Outer Disk. *ApJ*, **660**, 441–460. 28
- WILLACY, K., KLAHR, H.H., MILLAR, T.J. & HENNING, T. (1998). Gas and grain chemistry in a protoplanetary disk. *A&A*, **338**, 995–1005. 21, 28
- WILLACY, K., LANGER, W., ALLEN, M. & BRYDEN, G. (2006). Turbulence-driven Diffusion in Protoplanetary Disks: Chemical Effects in the Outer Regions. *ApJ*, **644**, 1202–1213. 28

- WILLIAMS, D.A. (2005). Gas and dust in the interstellar medium. *Journal of Physics Conference Series*, **6**, 1–17. 19
- WILLIAMS, J.P., BLITZ, L. & STARK, A.A. (1995). The Density Structure in the Rosette Molecular Cloud: Signposts of Evolution. *ApJ*, **451**, 252. 1, 3
- WOITKE, P., KAMP, I. & THI, W.F. (2009a). Radiation thermo-chemical models of protoplanetary disks. I. Hydrostatic disk structure and inner rim. *A&A*, **501**, 383–406. 148
- WOITKE, P., THI, W.F., KAMP, I. & HOGERHEIJDE, M.R. (2009b). Hot and cool water in Herbig Ae protoplanetary disks. A challenge for Herschel. *A&A*, **501**, L5–L8. 28, 142
- WOLFIRE, M.G. & CASSINELLI, J.P. (1987). Conditions for the formation of massive stars. *ApJ*, **319**, 850–867. 9
- WOODALL, J., AGÚNDEZ, M., MARKWICK-KEMPER, A.J. & MILLAR, T.J. (2007). The UMIST database for astrochemistry 2006. *A&A*, **466**, 1197–1204. 16
- WYROWSKI, F., GÜSTEN, R., MENTEN, K.M., WIESEMAYER, H. & KLEIN, B. (2012). Terahertz ammonia absorption as a probe of infall in high-mass star forming clumps. *A&A*, **542**, L15. 104
- ZHU, Z., HARTMANN, L. & GAMMIE, C. (2009). Nonsteady Accretion in Protostars. *ApJ*, **694**, 1045–1055. 29

ZHU, Z., HARTMANN, L. & GAMMIE, C. (2010a). Long-term Evolution of Protostellar and Protoplanetary Disks. II. Layered Accretion with Infall. *ApJ*, **713**, 1143–1158. 29

ZHU, Z., HARTMANN, L., GAMMIE, C.F. *et al.* (2010b). Long-term Evolution of Protostellar and Protoplanetary Disks. I. Outbursts. *ApJ*, **713**, 1134–1142. 29

ZINNECKER, H. & YORKE, H.W. (2007). Toward Understanding Massive Star Formation. *ARA&A*, **45**, 481–563. 8